DEVELOPMENT OF COMPUTATIONAL MASS AND MOMENTUM TRANSFER MODELS FOR EXTRACORPOREAL HOLLOW FIBER MEMBRANE OXYGENATORS

by

Kenneth Leslie Gage

B.S.ChE, University of Florida, 1995

Submitted to the Graduate Faculty of

the School of Engineering in partial fulfillment

of the requirements for the degree of

Doctor of Philosophy

University of Pittsburgh

2007

UNIVERSITY OF PITTSBURGH

SCHOOL OF ENGINEERING

This dissertation was presented

by

Kenneth Leslie Gage

It was defended on

October 26th, 2005

and approved by

Fernando Boada, Ph.D., Associate Professor, Departments of Radiology and Bioengineering, Director, UPMC MR Research Center

Harvey S. Borovetz, Ph.D., Professor and Chair, Department of Bioengineering, Robert L. Hardesty Professor, Department of Surgery, and Professor, Department of Chemical and Petroleum Engineering

William J. Federspiel, Ph.D., Associate Professor, Departments of Chemical and Petroleum Engineering, Surgery, and Bioengineering

Jörg C. Gerlach, M.D., Ph.D., Professor, Departments of Surgery and Bioengineering

Dissertation Director: William R. Wagner, Ph.D., Associate Professor, Departments of Surgery, Bioengineering and Chemical and Petroleum Engineering

DEVELOPMENT OF COMPUTATIONAL MASS AND MOMENTUM TRANSFER MODELS FOR EXTRACORPOREAL HOLLOW FIBER MEMBRANE OXYGENATORS

Kenneth Leslie Gage, PhD

University of Pittsburgh, 2007

Simulation of mass and momentum transfer in hollow fiber membrane (HFM) oxygenators has remained a topic of interest for decades. The current work reports upon efforts toward modeling the transport phenomena within these devices using a computational fluid dynamic (CFD) approach. The results and findings form a basis for future efforts in computational model development, design refinement and the investigation of other HFM systems.

The main purpose of the present work was to determine the validity and applicability of the Darcian porous media model for three-dimensional flow simulations of a commercial membrane oxygenator design. Close agreement between experiment and simulation was found for pressure losses within the device, although not within the standard deviation of the experimental data. The divergence could be attributed to the governing equations, which incorporated the Darcian model parameters into a less restrictive model, or the model parameters themselves, which were assumed isotropic and uniform.

The porous media model developed was used to predict the superficial velocity field of the membrane oxygenator during operation. For model verification, the experimental and CFD-predicted flow fields were compared using optical flow calculations performed on radiographic and simulated radiographic images, respectively. The data obtained were adequate for qualitative but not quantitative comparison and suggested reasonable agreement between experiment and simulation. Methods for improving the data and its interpretation were also described.

It was hypothesized that appropriate CFD models would predict the local oxygen concentration and gas exchange in a HFM oxygenator. A mass transfer correlation for a non-reactive fluid was derived using parameters from the literature. The correlation was converted to a reactive form for blood through dimensional analysis and incorporated into a CFD simulation. The results from these simulations and an analysis of the experimental process indicated that the parameters used are subject to error when data collection is performed in a limited flow range.

In conclusion, CFD-based simulations hold promise for HFM evaluation and design. Future researchers should consider the appropriateness of models and parameters during simulation development. Proper validation techniques are also critical for model assessment and evaluation.

TABLE OF CONTENTS

LIST OF FIGURES

PREFACE

"I have yet to see any problem, however complicated, which, when you looked at it in the right way, did not become still more complicated."

- Poul Anderson

I dedicate this dissertation and the work involved to my wife and children. To them I owe more than can be written.

The dissertation committee has a central role in molding the minds of doctoral candidates from that of an undergraduate to an independent investigator. Too often I ignored the insight and wisdom given to me from the committee, and I implore others to avoid this mistake. Without their assistance and hours of support I would not have been able to begin this work, much less bring it to fruition. I owe each of them a debt of gratitude.

To Dr. William R. Wagner, as my advisor and confidant for more than a decade (for the latter, at least), I owe a great deal more than gratitude. His intelligence, guidance, and above all patience made the work herein possible. I will strive to become an academic leader and mentor in the model he has demonstrated to me.

Last but not least, I thank my parents, Alan and Christine Gage, and brother, Edward, for their steadfast support, love and prayers. I could not have completed graduate school without their constant, sometimes vigorous, exhortations.

1.0   INTRODUCTION[1]

"Those who cannot remember the past are condemned to repeat it."
   - George Santayana

1.1   HISTORICAL OVERVIEW OF EXTRACORPOREAL OXYGENATION

An appreciation of the chronological and technological progression of extracorporeal gas exchange can assist in delineating the major factors that determine clinical success and failure. Stammers [2] has separated the historical development of extracorporeal support into three phases; a "conceptual and developmental period" occurring prior to 1950 [3], an "applied technological period" that lasted until 1970, and a "refinement period" that continues until the present time.   The overview presented herein will be divided upon technological lines, with major developments presented in a chronological fashion. The interested historian can find further information in a number of excellent publications [4-7] celebrating the 50th anniversary of the first successful application of total cardiopulmonary bypass [8].

1.1.1   Artificial Oxygenators

A number of artificial devices for oxygenating the blood have been proposed since La Gallois first put forth the concept of extracorporeal life support in 1812 [9]. The designs have been

---

[1] The chapter contents are based in part upon a published book chapter previously authored by the Ph.D. applicant [1]   K. L. Gage and W. R. Wagner, "Cardiovascular Devices," in *Standard Handbook of Biomedical Engineering and Design*, *McGraw-Hill Standard Handbooks*, M. Kutz, Ed. New York: McGraw-Hill Professional, 2002, pp. 20.1-20.48.

classified based on the method of gas exchange and are presented with an overview of the important developmental milestones and device features.

1.1.1.1 Film Oxygenators

Now relegated to historical interest, film oxygenators were dominant during the 1950's when cardiopulmonary bypass (CPB) was in its clinical infancy. In these systems, the "film" refers to a thin film of blood created on the surface of a supporting structure (e.g., disk, sheet, and cylinder) through either immersion into a blood pool or pouring of the blood over the surface. The resulting blood film is exposed directly to an oxygenating gas within the device chamber. Historical reviews on the development of CPB [2, 3] credit von Frey and Gruber with developing the first film oxygenator in 1885 [10] as part of the first closed perfusion loop, a forerunner to the modern heart-lung machine [4].

The film oxygenator was present in various forms for a number of surgical milestones. Dr. Clarence Dennis unsuccessfully attempted the first intracardiac repair under total CPB on April 5th, 1951 using a rotating screen oxygenator [11]; the failure was attributed to an iatrogenic cause and not the device itself [2, 3]. The first successful intracardiac repair under total CPB was performed by Dr. J. H. Gibbon Jr. on May 6th, 1953 [8], culminating years of prior animal research; unfortunately, it was a success he was unable to repeat.

Although effective, film oxygenators suffered from a number of failings that eventually led to their replacement. The direct gas-blood interface allowed for adequate gas exchange but led to extensive damage to the formed blood elements and derangement of the coagulation cascade [12]. The large blood priming volume and time-consuming, complicated maintenance and use procedures were also a disadvantage [5]. Because of these problems, bubble oxygenators begin to eclipse film devices in the 1960's [5].

1.1.1.2 Bubble Oxygenators

Bubble oxygenators were dominant in clinical use throughout most of the fifty-year history of CPB. The first practical bubble oxygenator was invented in 1882 [13] and later incorporated into a closed loop perfusion device in 1890 [3, 14].

The initial bubble units were constructed of the same materials as the film devices and therefore not disposable, although the devices possessed a lower prime requirement and greater

mass transfer compared to the film units. The advent of the disposable plastic bubble oxygenator in the late 1950's [15] resulted in a move away from the more complex oxygenator designs [16]. In the early 1980's, bubble oxygenators began to lose ground to the improved membrane oxygenator designs then under commercial development and production. By 1985, the devices used for CPB were evenly split between bubble and membrane type units [5].

1.1.1.3 Membrane Oxygenators

The use of a semipermeable membrane to separate the blood and gas phases characterizes all membrane oxygenator designs. Membrane oxygenators can be further divided into *flat-sheet / spiral-wound* and *hollow-fiber* models. The flat-sheet designs restrict blood flow to a conduit formed between two membranes, with gas flowing on the membrane exterior; these systems were the first membrane oxygenators to enter clinical use [17]. Despite their concurrent development with bubble oxygenators, the primitive membrane devices shared a number of shortcomings with the earlier film units, including a large priming volume and more difficult operational procedure that required sizing the device to the patients' metabolic need [5]. These factors limited the use of membrane oxygenators for a considerable time.

Spiral-wound oxygenators use membrane sheets as well, but are arranged in a roll rather than the sandwich formation of the original flat-sheet assemblies. Polymers such as polyethylene, ethylcellulose [18], and polytetrafluoroethylene [17] were used for membranes in these early designs as investigators searched for a material with high permeability to oxygen and carbon dioxide but that elicited mild responses when in contact with blood. The introduction of polysiloxane as an artificial lung membrane material in the 1960s provided a significant leap in gas transfer efficiency, particularly for carbon dioxide [19]. These membranes remain in use today for long-term neonatal ECMO support.

Development of the microporous hollow fiber led to the next evolution in lung design, the hollow-fiber membrane oxygenator [2]. Increased carbon dioxide permeability compared to solid membranes, coupled with improved structural stability, has secured the standing of these devices as the market leader [2, 12]. The current, standard artificial lung is constructed of hollow microporous polypropylene fibers housed in a plastic shell. An extraluminal cross-flow design is used for most models and is characterized by blood flow on the exterior of the fibers with gas constrained to the fiber interior. Intraluminal flow designs utilize the reverse blood-gas

arrangement, with blood constrained to the fiber interior. The laminar conditions experienced by blood flowing inside the fibers result in the development of a relatively thick boundary layer that limits gas transfer. Extraluminal-flow devices are less susceptible to this phenomenon, and investigators have used barriers and geometric arrangements to passively disrupt the boundary layer, resulting in large gains in mass transfer efficiency [20, 21]. Extraluminal-flow hollow fiber membrane oxygenators have come to dominate the market because of their improved mass transfer rates and decreased flow resistance, the latter of which minimizes blood damage [12].

1.1.2   Biological Oxygenators

Although the bulk of research effort in extracorporeal life support has sought to use an artificial lung for the purpose of gas exchange, some investigators resorted to the use of biological lungs, either excised or in place, as an alternative. During the pioneering days of cardiac surgery, the oxygenator was only one of many potential problem sources facing the surgeon, who was also concerned with the difficulties of surgical approach and patient management. The absence of a specialized perfusion staff added to the surgeon's primary burden of performing the surgical intervention. It is understandable that some sought to replace the bulky, unreliable oxygenator with a biological system of proven performance, at least for the short term.

Homologous and heterologous donor lungs have been investigated as gas exchange devices in both the research and clinical setting. In 1895 Carl Jacobj, recognizing that direct gas-blood contact led to blood damage and derangement [3], supplanted the primitive bubble oxygenator [14] in his closed organ perfusion apparatus with a set of excised animal lungs [22] in order to place a natural membrane between the perfusate and oxygenating gas. Although Dr. Jacobj's device was used for the evaluation of isolated organ function, the concept of the natural lung as a gas exchange unit was later to be demonstrated on larger scale. On November 1st, 1926, the first total cardiopulmonary bypass of an animal (dog) was performed by Dr. Sergei Brukhonenko of the USSR using a heart-lung machine of his own design complete with a set of donor canine lungs [23]. Dr. Brukhonenko's device permitted the use of animals for surgical research and the practice of operative technique, but it was not intended for clinical application in conjunction with donor lungs [23].

4

In the United States and Canada, the use of heterologous and homologous donor lungs progressed to clinical application. Successful intracardiac repairs were performed using the donor lungs of rhesus monkeys [24] and mongrel dogs [25]. Banked donor lungs were also utilized but without success [26]. The arrival of more reliable artificial lung units led to the abandonment of the donor lung approach.

1.2 THERAPEUTIC APPLICATIONS OF ARTIFICIAL LUNGS

In the more than 50 years since the first successful clinical application of an artificial lung in humans, extracorporeal life support (ECLS) has been utilized as a therapeutic intervention for a broad range of clinical conditions. An understanding of the terminology defining these interventions, the indications for initiation of treatment, and the complications associated with their clinical use is required to define appropriate performance criteria when designing new devices. An appreciation for the relative market size for each application is also beneficial as device cost and reimbursement issues continue to be major factors in determining whether new, "improved" devices enter widespread clinical use.

1.2.1 Cardiopulmonary Bypass (CPB)

The indications for cardiopulmonary bypass are surgical in nature, and are based on whether the particular procedure requires the heart to be arrested. Currently, most cardiac surgical procedures fall into this category [27]. The goal of CPB is to temporarily divert the blood around the heart and lungs, providing the surgeon with a stable, blood-free field to perform both intracardiac repairs (valve surgery, repair of septal defects) and extracardiac procedures such as coronary artery bypass grafting (CABG).

Cardiopulmonary bypass (CPB) is the most prevalent therapeutic application requiring the use of an artificial lung, and is expected to remain so for the foreseeable future. In 2000, there were approximately one million interventions requiring CPB around the globe, with somewhat less than half of these occurring within the U.S.A. [5]. However, the use of CPB is

slowly declining, with the number of U.S. cases having dropped to 350,000 in 2004 [5]. Recent trends in minimally invasive surgery have led to surgical systems that allow some procedures such as coronary artery bypass grafting to be performed in the absence of oxygenator support [28], although the dominant cause for the reduction in CPB cases is believed to be an increase in the number of coronary interventions by cardiologists [5].

1.2.2 Extracorporeal Membrane Oxygenation (ECMO)

In contrast to cardiopulmonary bypass, medical criteria are the primary indicators for initiation of extracorporeal membrane oxygenation (ECMO). Conventional treatment of acute respiratory failure calls for high-pressure mechanical ventilation with an elevated percentage of oxygen in the ventilation gas. Unfortunately, the high oxygen concentration can result in oxidative damage to lung tissue (oxygen toxicity) and, in the case of the newborn, proliferation of blood vessels in the retina leading to visual damage (retinoproliferative disorder) [29]. The high pressures used to achieve maximum ventilation area also cause lung damage through a process known as barotrauma. In essence, the lungs are being subjected to further damage by the therapy employed, preventing the healing necessary to restore proper lung function. The purpose of ECMO is to take over the burden of gas exchange and allow the native lung tissue time to heal.

ECMO is considered a standard therapy for the treatment of respiratory failure in neonatal patients [29]. In adult and pediatric patients, it is a treatment of last resort for individuals who would otherwise die despite maximal therapy [29, 30]. Even in neonatal cases, ECMO is a therapy reserved for those patients with severe respiratory compromise and a high risk of death who are failing traditional ventilator-based interventions. Common causes of respiratory failure in the neonatal population treatable with ECMO support include pneumonia or sepsis, meconium aspiration syndrome, respiratory distress syndrome, persistent fetal circulation, and congenital diaphragmatic hernia [29, 30]. Contraindications to ECMO support include root causes that are irresolvable, such as a major birth defect or genetic abnormality, and comorbid conditions such as intracranial hemorrhage or fetal underdevelopment that suggest a poor outcome [29]. Indications for ECMO use in the pediatric and adult populations are not dissimilar from those of the neonate, but the causes for respiratory or cardiopulmonary failure are different, and many individuals suffer from comorbid conditions. Indications include pneumonia,

aspiration pneumonitis, acute respiratory distress syndrome, and recoverable heart failure as caused by infection or post-surgical complications [29].

1.3   DESIGN GOALS FOR ARTIFICIAL LUNGS

At a minimum, an ideal artificial lung would be biocompatible over sustained operational periods and possess excellent mass transfer performance. A careful balance must be struck between the competing flow-dependent phenomena of mass transfer and biocompatibility to achieve ideal operation. In general, mass transfer rates are increased as the blood boundary layer thickness is reduced. In the case of traditional, static hollow fiber membrane oxygenators, the reduction in boundary layer thickness is often attained through higher flow rates. The fluid boundary layer can be shown to be the dominant factor in limiting gas transfer to blood in modern membrane oxygenators analytically and through experimental data [31]. This relationship can be modeled for idealized gas transfer surfaces with simplified geometries and flow fields. With increased computational power and numerical method sophistication, the subtleties in boundary layer effects can be investigated for complex systems that include multiple fibers in a pulsatile environment [32].

Unfortunately, high blood velocity can result in shear induced damage to the red blood cells [33], which is of concern for long duration (i.e., ECMO) support. In addition, shear induced platelet activation can occur at higher velocities [34], resulting in platelet consumption and derangement of clotting homeostasis. At the other end of the blood speed spectrum, sluggish flow in artificial lungs has previously been linked to thrombosis [35], presumably due to a localized buildup of activated coagulation and platelet activating factors. The desire for improved gas exchange must be balanced with the clinical sequelae associated with thrombosis and red blood cell destruction.

Computer optimization of artificial lung blood flow pathways and operating variables offers the promise of achieving such a balance in a mathematical, objective manner. A numerical optimization approach would require accurate spatial models to characterize and predict each of these phenomena on a local scale. Models for gas exchange [36], pressure drop [37], blood damage [33], and coagulation [38] have been developed, although a one or two dimensional approximation is often used. One characteristic shared among these models is a critical

dependence upon the blood velocity, a dependence which is spatially variable in three dimensional simulations. Accurate prediction of the 3D blood velocity field is a prerequisite for proper application of the above models, yet the literature reveals a lack of experiments verifying the flow field predictions of computational fluid dynamic simulations. Despite these difficulties, recent efforts in the CFD based optimization of an oxygenator design have met with considerable success [39], although experimental validation of the resulting optimal design and CFD predicted values was limited.

Despite the persistent clinical need for an artificial lung capable of providing long-term respiratory support, no such device is commercially available at the present time. Device standards have been under development for oxygenator evaluation since 1969 [40] and have culminated with clinical benchmarks from regulatory and standardization bodies such as the Food and Drug Administration (FDA) [41] and the Association for the Advancement of Medical Instrumentation (AAMI) [42]. However, the current standards represent clinical minimums, and the methods used in evaluation do not provide sufficient information for the development and testing of advanced computational models, which are the very models required for accurate, robust computer based optimization of the next generation of artificial lungs.

1.4 PURPOSE OF THE CURRENT WORK

A review of the artificial organs and related engineering literature reveals numerous studies utilizing computational fluid dynamics (CFD) to investigate the performance of a broad range of medical devices. Recent publications have reported on the use of CFD to examine the functioning of artificial hearts [43, 44], artificial lungs [35, 45], and other devices such as a cardioplegia heat exchanger [46]. In some cases, corroborating experimental methods such as particle image velocimetry [44] are used to evaluate the validity of the numerical model, which can then serve as the basis for the determination of clinically relevant phenomena such as hemolysis [47, 48] and thrombosis [49].

One benefit of CFD modeling is the ability to investigate an expanded design space without resorting to repeated, expensive experimentation to verify the effects of minor changes [39]. A CFD model can help guide a device design to maximize desired characteristics while

shortening the design cycle and reducing development cost [43, 44]. For many devices, such as an artificial heart or pump, accurate prediction of the flow field and derived variables provides a sufficient level of detail for analysis and investigation. However, artificial lungs and other mass transfer devices require accurate prediction of both flow and species transport characteristics for design analysis, thus complicating the modeling approach. Further complications arise in that the gas transfer to blood is non-linear, being dependent upon the oxygen binding characteristics of hemoglobin. Inclusion of models capable of describing blood hemolysis or thrombotic deposition into the analysis results in a very complex system that exceeds even the extensive computational power available today. The possible benefit of a model that accurately predicts device performance a priori, coupled to a computer based optimization approach, fuels current modeling efforts despite limitations.

This research sought to develop and investigate the use of CFD models to predict the pressure-flow and mass transfer performance of hollow fiber membrane (HFM) oxygenators. The results and findings form a basis for future efforts in computational model development, design refinement, and the investigation of other HFM systems.

The specific aims of the research were to:

Test the hypothesis that CFD could predict the pressure field encountered in a standard membrane oxygenator when coupled with an appropriate porous media model. In examining this hypothesis, the appropriate functional form of the porous media model was determined through a combination of experiment and simulation. Initial model verification was performed by comparing the computer predicted pressure field to that obtained via pressure drop experiments.

Test the hypothesis that CFD could predict the flow field encountered in a standard membrane oxygenator when coupled with an appropriate porous media model. The porous media model developed pursuant to the first research aim was used to predict the superficial velocity field of the membrane oxygenator under investigation. Model verification was performed by means of comparison of the predicted flow field to the field obtained via experiment using radiographic techniques and optical flow calculation.

Test the hypothesis that CFD could predict the local oxygen concentration encountered in a standard membrane oxygenator when coupled with an appropriate porous media and mass transfer model. The functional form of a mass transfer correlation for a non-reactive fluid such as water was derived by utilization of literature derived parameters. Using dimensional analysis the

equation was converted to a reactive form for blood and utilized in a CFD simulation. The results from this simulation of oxygen transfer were compared to experimental data.

2.0   PRESSURE-FLOW RELATIONS FOR HOLLOW FIBER MODULES[2]

2.1   BACKGROUND

The engineering literature abounds with pressure-flow relationships for a variety of systems analogous to the hollow fiber membrane lung. It is somewhat surprising then that the modeling of pressure drop within HFM units has been primarily limited to the use of simple nonlinear equations based on isotropic porous media assumptions.

2.1.1   General approach to modeling of porous media

The phrase "porous media model" in the present work is intended to encompass those models that utilize a lumped parameter approach to incorporate both linear and nonlinear momentum loss effects. It is useful to organize porous media models according to the length scale of application or development; such a scheme allows practical comparisons between different models and an appreciation for the advantages and limitations imposed through work at a particular length scale.

The first published article regarding the CFD modeling of a hollow fiber oxygenator, the commercial Avecor Affinity™ (Avecor Cardiovascular, Inc. Plymouth, MN), utilized a Darcian porous media model to account for momentum losses within the bundle zone [51]. Later investigators utilized a nonlinear Ergun or Forchheimer model [35, 45, 52] to account for inertial losses that could occur within the device. An analysis of the Reynolds number reveals a small

---

[2] The chapter contents are based in part on a published journal article previously authored by the Ph.D. applicant.

[50]   K. L. Gage, M. J. Gartner, G. W. Burgreen, and W. R. Wagner, "Predicting membrane oxygenator pressure drop using computational fluid dynamics," *Artif Organs*, vol. 26, pp. 600-7, 2002.

value even at high flow rates, indicating that inertial losses in the traditional, turbulent sense should not be present. However, pressure losses that possess nonlinear velocity dependence are documented to occur in these devices, which raise questions as to the nature of the phenomena at their source [37]. It is known that deviation from simple Stokes flow begins at a Re greater than 0.1, well below the onset of true turbulence. The cause of this momentum loss remains under debate [53, 54].

Authors have calculated Re in blood oxygenators using a variety of different approaches. The porous media literature typically calculates Re for low porosity devices using the conduit flow approach where the "wetted perimeter" (blood flow path characteristic dimension) is utilized. The Re in high porosity devices is better represented using a submerged flow approach with the object diameter as the appropriate length scale. Unfortunately these guidelines are not consistently applied, which makes comparison of results between different studies difficult.

2.2   MATERIALS AND METHODS

2.2.1   Experimental Methods

A standard uncoated oxygenator (Maxima™ Hollow Fiber Membrane Oxygenator, Medtronic Corp., Anaheim, CA, U.S.A.) was modified to allow pressure measurements along the fiber bundle region. Holes were bored into the plastic housing of the Maxima at prescribed locations using a #3 (5.41 mm) drill bit. Care was taken to avoid breaching the interior wall of the housing and damaging the fibers through direct contact with the drill bit or mobile debris. A ¼ inch-28 thread size tap modified with a flattened tip was used to create threads in the bore hole and gently push the remaining wall material into the bundle where it was subsequently retrieved under microscopy. The local fiber area was visualized for traumatic damage or disruption of the fiber arrangement near the wall which could affect local flow conditions and pressure measurements. Minor fiber damage resulting in loss of fluid integrity of the gas flow path was not a concern as the focus of the experiment was on momentum transport and not gas exchange. Threaded polycarbonate female Luer ports (Value Plastics, Inc., Fort Collins, CO, U.S.A.) were

shortened to prevent projection into the fiber bundle and then glued into place with epoxy to complete the modification.

Ports were placed to take advantage of device symmetry. The fiber bundle assembly of the Medtronic Maxima™ has the general shape of a hollowed cylinder, with a single outflow port disrupting the circular appearance when viewed from above. From the overhead view, a symmetry plane bisects the device into halves, passing through the midline of the device outflow port. The symmetry plane was used to define the cardinal axes of the device, with the front being located inline with the outflow port, the back located at the antipodal position, and the left and right sides being defined by location relative to the plane itself. Five ports were placed along each of the cardinal axes of the oxygenator fiber bundle, with additional ports being positioned at the device inflow and outflow, between the heat exchanger and fiber bundle assembly, and at the outflow collection ring. The port locations allow the pressure drop contribution of the fiber bundle and the heat exchanger to be separated. The modified and assembled oxygenator is shown in **Figure 2-1**.
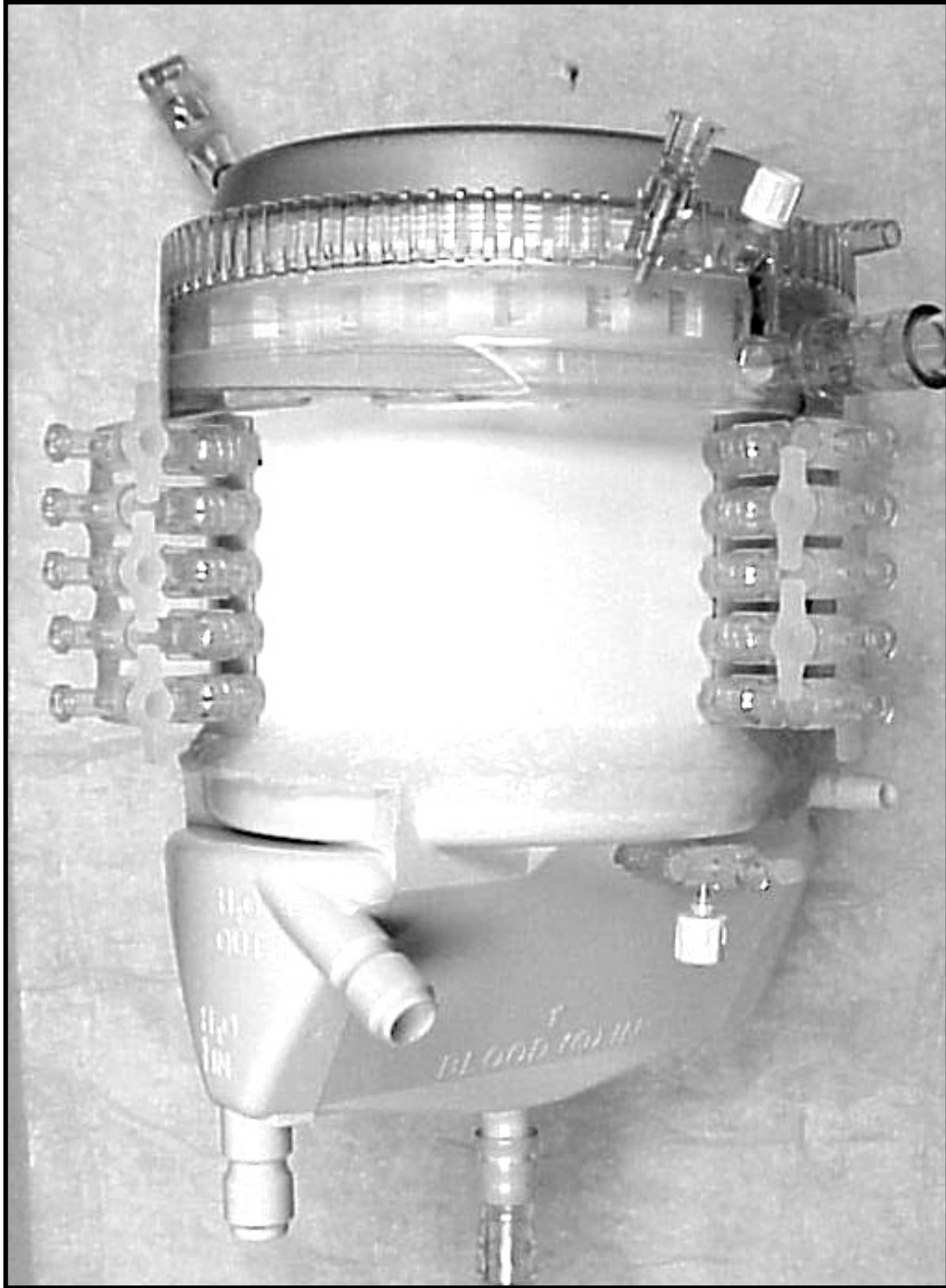
Figure 2-1 The pressure measurement ports for the Maxima™ are shown.

A mock circulatory loop was constructed as shown in **Figure 2-2**. The experimental fluid was deionized water maintained at 37° C by a heating recirculator (Model 210, Polyscience, Niles, IL, U.S.A.). A clinical centrifugal pump (520D Bio-console and BP-80 Bio-pump, Biomedicus, Minneapolis, MN, U.S.A.) provided flow in the system. The Biomedicus pump is not a constant displacement or roller pump but generates a pressure differential in the system. Under constant feed and back pressure, steady-state flow can be achieved. The pressure in the reservoir was thus maintained at 10 mmHg (1333 Pa) to provide a constant upstream and supply head.
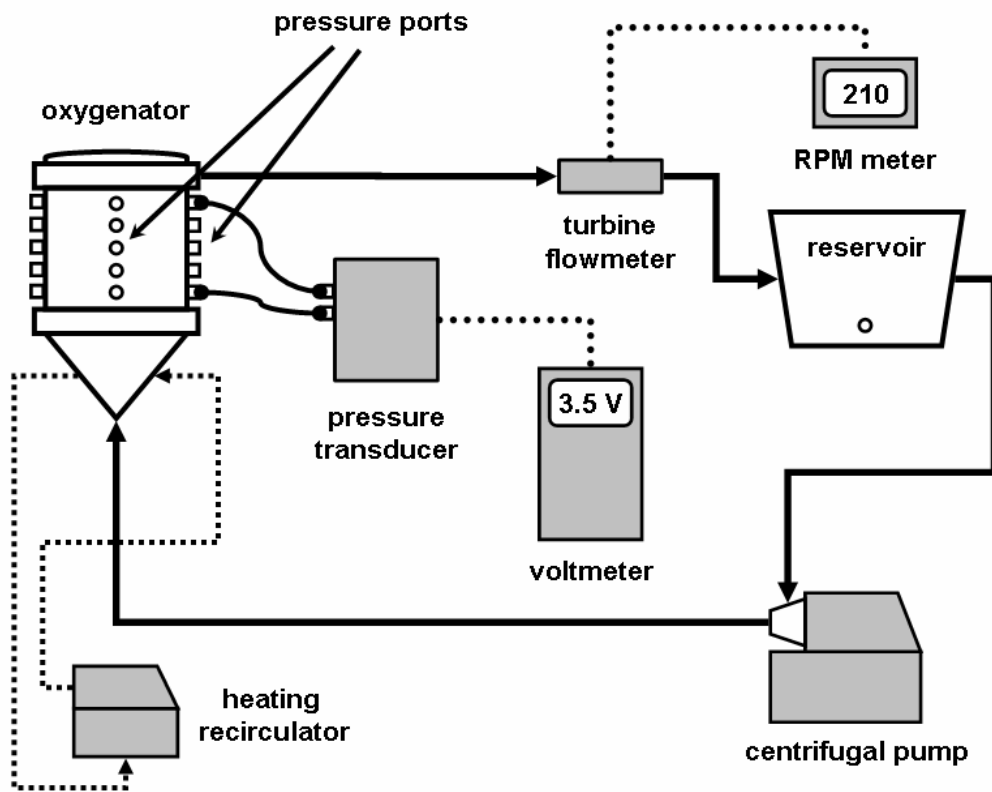
Figure 2-2 Mock circulation loop for the pressure-flow experiments.

Flow rate measurements were made using a turbine flowmeter (FTB2002, Omega Engineering, Inc., Stamford, CT, U.S.A.) positioned after the oxygenator in a straight length of tubing. An amplified, signal-conditioned pressure transducer with a 0-34474 Pa (0-5 psi) range (ASCX05 Series, Invensys Sensor Systems, Milpitas, CA, U.S.A.) was used to measure pressure at the port locations. All liquid was eliminated in the connection tubing between sample port and pressure transducer via air pressurization prior to measurement. Experiments were performed at 2, 4 and 6 L/min flow rates. The number of trials performed at each flow rate differed, ranging between three to five independent measurements at each port location.

2.2.2 Computational Model

A commercial computer-aided design software package, I-DEAS Master Series 8 (SDRC, Milford, OH, U.S.A.), was used to generate the three-dimensional geometry and computational surface mesh of the oxygenator. The oxygenator geometry is symmetric about a single sagittal plane passing from the center of the device through the outflow port. The sagittal plane can be described as the plane that divides the oxygenator into left and right halves that are mirror images and where both halves possess half of the inlet (heat exchanger) and outlet (collection cap) regions. The model domain encompassed the region of the oxygenator distal to the heat exchanger, including the flow diffuser and inlet, fiber bundle region, and fluid collection ring. A triangular surface mesh was generated in I-DEAS using the geometry as a guide, and then exported to a volumetric grid generator (TGrid, Fluent, Inc., Lebanon, NH, U.S.A.) for final meshing. The final tetrahedral mesh contained approximately 240,000 elements and is shown in **Figure 2-3**.
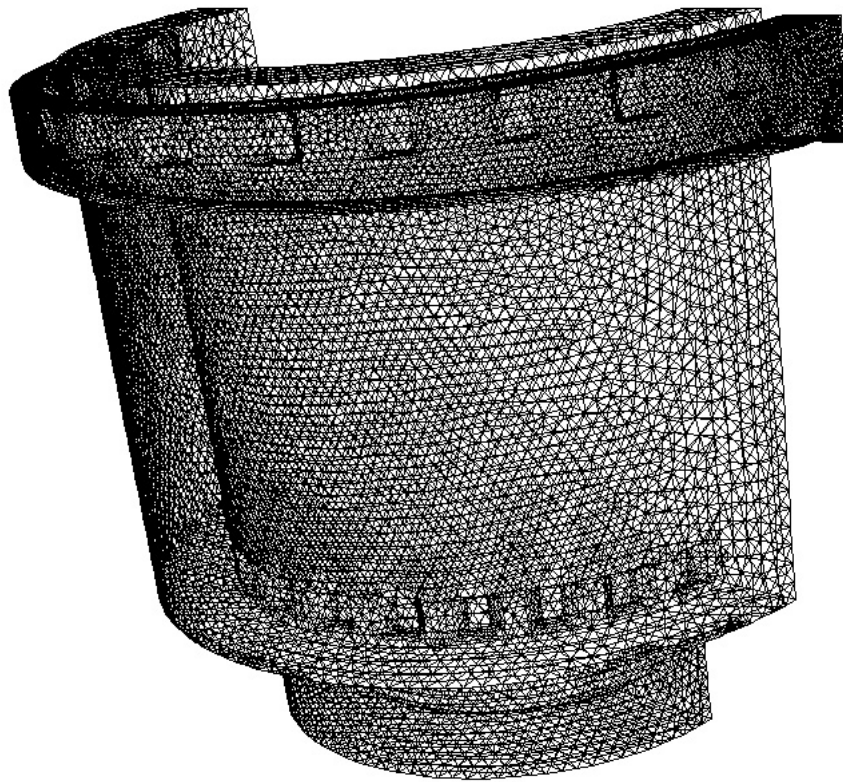
Figure 2-3 Surface mesh used for numerical investigations of pressure-flow.

A commercial CFD code, FLUENT5 (Fluent, Inc., Lebanon, NH, U.S.A.), was used to discretize and solve the mass and momentum equations governing fluid flow through the device. FLUENT5 utilizes the finite volume method to solve the discretized conservation equations. All simulations were run on either a SGI Indigo2 or Octane2 (Mountain View, CA, U.S.A.) workstation. The solution was considered converged when the mass residual was unchanging and less than 1.0 x 10-3. The outflow mass flow rate, a value determined through surface integration of the pressure outlet, was monitored and compared with the inflow mass flow rate as a second check on solution convergence.

2.2.2.1 Boundary Conditions

Boundary conditions applied in the numerical simulation are based on conditions encountered during the water perfusion experiments. A velocity boundary condition was specified at the domain inlet. Steady laminar flow was assumed in all cases. In the actual device, the inlet is

located just distal to the heat exchanger tube bank. Because of the proximity of the inlet to the tube bank, a plug flow velocity profile was assumed to approximate the fluid flow. The fluid was assumed to be incompressible (ρ = 993 kg / m3) and possess a Newtonian viscosity (μ = 0.71 cP) consistent with that of water at 37° C. A constant pressure boundary condition was set for the domain outflow. The no-slip condition was enforced at the wall boundaries, and a symmetry condition was applied along the appropriate plane.

2.2.2.2 Porous Media Approximation

Direct numerical simulation of flow in and about the individual fibers of the present fiber bundle is impossible with today's technology. To overcome this limitation, a porous media model that accounts for the tortuosity of the fiber bundle was used. Momentum losses were approximated using Darcy's Law [55]

$$\nabla p = -\frac{\mu}{\alpha}\mathbf{v} \qquad \text{Equation 2-1}$$

where p is the static fluid pressure, α represents the fiber bed permeability, μ the dynamic fluid viscosity, and $\mathbf{v}$ the superficial velocity (volumetric flow rate divided by fiber bundle cross sectional area). The losses predicted by the porous media model are incorporated into the momentum balance equation in the i-direction as a source term [56, 57],

$$\frac{\partial}{\partial t}(\rho v_i) + \frac{\partial}{\partial x_j}(\rho v_i v_j) = -\frac{\partial p}{\partial x_i} + \frac{\partial \tau_{ij}}{\partial x_j} + \rho g_i + S_i \qquad \text{Equation 2-2}$$

where ρ is the fluid density, t is time, x_i, x_j are directional coordinates, τ_{ij} is the stress tensor, and g_i is the gravitational force. For a simple homogenous Darcian porous media, the source term S_i is

$$S_i = -\frac{\mu}{\alpha}v_i \qquad \text{Equation 2-3}$$

as derived from [45]. It is worth noting that all calculations are performed using the superficial velocity, $\mathbf{v}$. The fiber bed permeability α was calculated from experimental pressure drop data collected at 4 L/min by assuming the superficial velocity was circumferentially uniform and unidirectional along the central axis of the device, thus reducing it to a single value.

The computational domain was divided into three separate fluid zones to allow application of the porous media model to the volume representing the fiber bundle and not the

18

inflow and outflow regions. Internal boundaries representing the transition between porous and non-porous fluid zones were identified at the entrance and exit windows of the fiber bundle. The exit windows of the fiber bundle can be seen through the clear collection ring in **Figure 2-1**. Interior surfaces were created at these locations during surface mesh generation and then used to define the separate fluid zones during the creation of the volumetric mesh. The momentum sink term defined in **Equation 2-3** was then applied to the momentum equations in the fluid zone corresponding to the fiber bundle.

2.3   RESULTS

The pressure distribution at the high flow condition of 6 L/min is presented in **Figure 2-4**. It can be seen that the pressure distribution throughout the bundle is predicted to be concentrically uniform despite the nonaxisymmetric location of the outflow port. Similar distributions were observed at 2 and 4 L/min.

Figure 2-5 compares the experimental pressure drops with those calculated by the CFD model. Experimental pressure drops were determined using the pressures recorded at the fiber bundle ports. The pressure drop for each location from each experimental run was then averaged over all experimental runs. The mean and standard deviation of the experimental pressure drops reveals a relatively narrow clustering of data. The pressure drops determined from the CFD simulation are based on the same spatial locations as the experimental ports. Good agreement is shown between the numerical simulation and experiment at 2 L/min, with the CFD results predicting lower pressure drops than recorded from experiment at the 4 and 6 L/min cases.
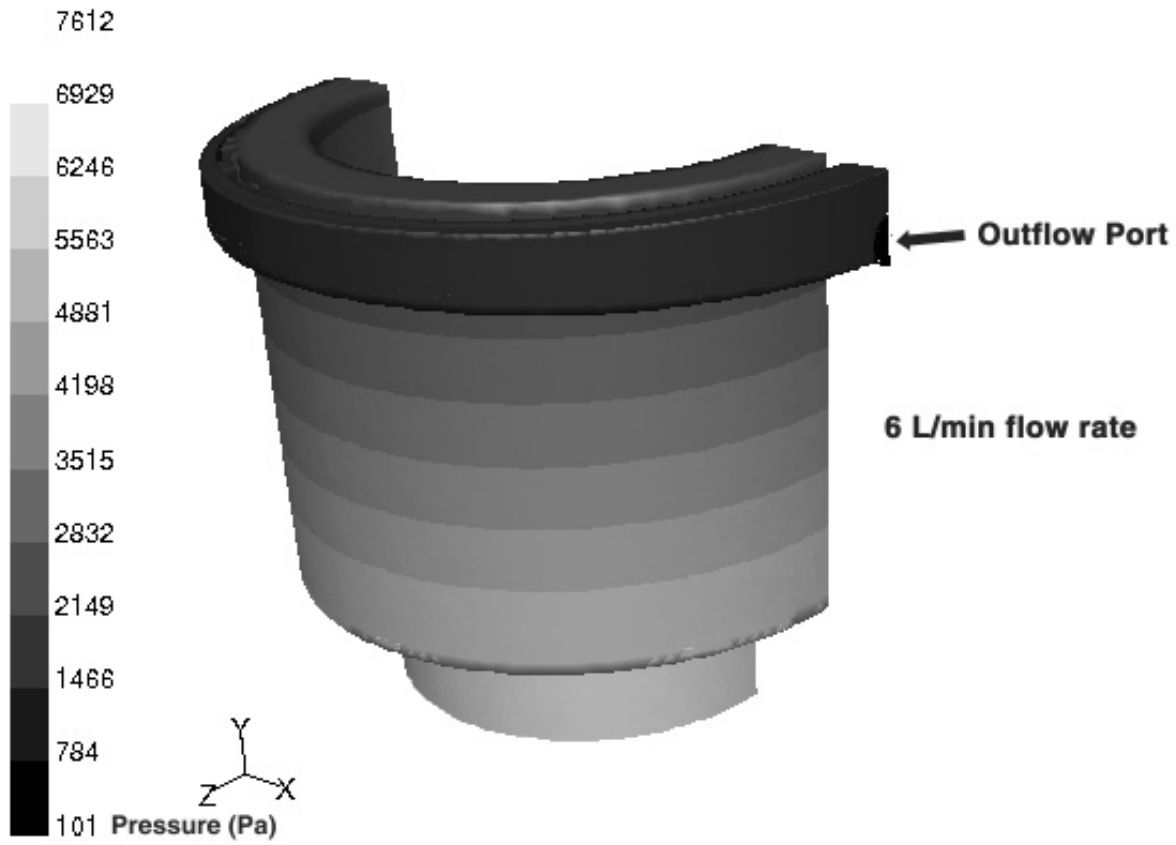
Figure 2-4 Pressure distribution for the 6 LPM flow case.
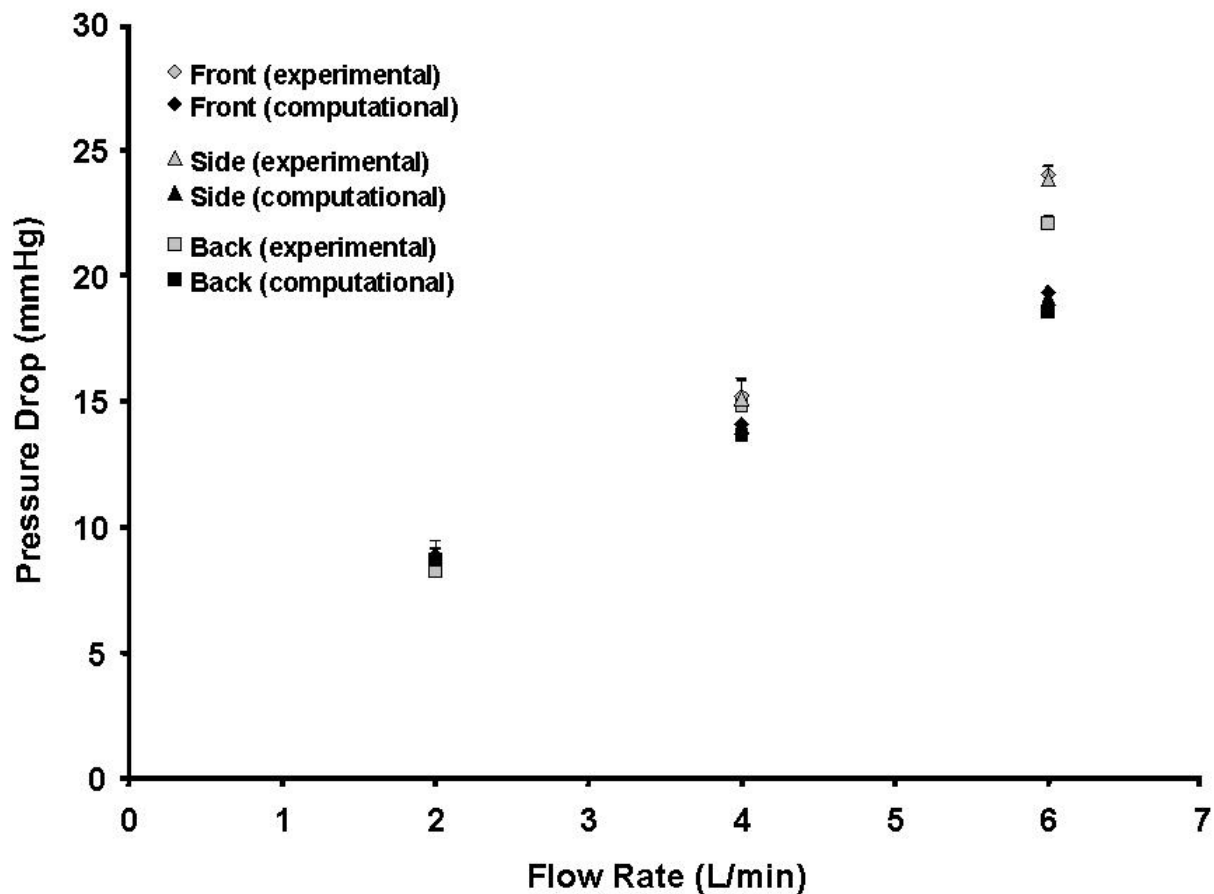
Figure 2-5 Comparison of experimental and CFD predicted pressure drops.

2.4   DISCUSSION

The purpose of the present work was to determine the validity and applicability of the Darcian porous media model for three-dimensional flow simulations of a commercial membrane oxygenator design. Close agreement between experiment and simulation was expected because Darcy's Law has been used with success by other researchers for modeling pressure drop in membrane oxygenators [45], and the permeability used in the simulation process was determined from experimental pressure drop data. As shown in **Figure 2-5**, the agreement is close but not within the standard deviation of the measured pressure drops. The lack of perfect agreement at 4

L/min might be explained by the fact that the momentum loss calculated by Darcy's law was added onto the full Navier-Stokes losses as a body force term. In essence, a small amount of viscous loss might have been double counted. The trend for increased deviation at higher flow rates is consistent with losses due to inertial effects, which are proportional to the superficial velocity v to the second power. Because the experimental pressure drop does not vary linearly with flow rate, the Darcian permeability as calculated here is not constant for the oxygenator under study. At 2 and 6 L/min, respectively, the Darcian permeabilities calculated from the experimental data range from 15% above to 14% below the permeability calculated at 4 L/min, which was the value used for all simulations. Small differences between the size of the actual device features and those present in our current geometric model could also contribute to the discrepancy by altering the pressure drop, particularly at the inlet and exit windows of the fiber bundle. However, the experimental pressure drop measurements were taken from within the fiber bundle and did not include the device windows (where fluid flow enters into the fiber bundle) or other features in the measured flow path. In addition, simulations with an open region in place of the fiber bundle indicate that the pressure drop contribution of the device windows is only a few percent of the total bundle pressure drop, reducing the likelihood that geometric considerations are the cause of the discrepancy between the experimental and computational results. Comparison of the predicted and experimental pressure drop data for the entire fiber bundle assembly (heat exchanger outflow to device outflow) reveals analogous behavior to that of the fiber bundle data shown in **Figure 2-5**. Further investigations are needed to determine whether inertial effects have a role in this case or whether other phenomena could be contributing to the deviation.

There are limitations in the present investigation. The oxygenator under study is no longer in production, and few samples remain. The scarcity of available oxygenators and the difficulty associated with cleaning blood-perfused devices restricted the current studies to water as the motive fluid. However, dimensional analysis can often provide insight into the performance of similar, scaled systems once the results for an analogous system are known. The dimensionless equation of motion for a fluid of constant viscosity and density can be written as

$$\frac{D\mathbf{u}^*}{Dt^*} = -\nabla^* p^* + \frac{1}{\text{Re}}\nabla^{*2}\mathbf{u}^*$$

Equation 2-4

where $\mathrm{Re} = \dfrac{DV\rho}{\mu}$ is the Reynolds number with V being defined as the characteristic or average velocity and D the characteristic system diameter [58]. The other terms in **Equation 2-4** are the dimensionless velocity $\upsilon^{\ast} = \dfrac{v}{V}$, dimensionless time $t^{\ast} = \dfrac{tV}{D}$, dimensionless pressure $p^{\ast} = \dfrac{(p - p_0)}{\rho V^2}$, and where p_0 is a convenient reference pressure. In regards to the dimensionless momentum equation, if two systems have the same Reynolds numbers, and the dimensionless boundary conditions are the same, the systems are mathematically identical [58]. Therefore, it might be possible to estimate the blood pressure drop while using water if a Newtonian viscosity blood model is assumed, the system variables are matched to produce the desired Reynolds numbers, and the dimensionless boundary conditions are equivalent. An alternative to utilizing dimensionless analogies to estimate the blood pressure drop involves the use of fluid analogues that more accurately mimic blood properties. Glycerin-water mixtures are in common use as Newtonian blood analogues, although more exotic formulations are needed if the non-Newtonian, shear-thinning properties of blood are to be represented [59]. Further studies with blood and blood analogues are required to determine what effect the non-Newtonian properties have upon the flow characteristics through fibrous porous media.

Other study limitations include the possibility that slight manufacturing differences between devices would present a spectrum of pressure drops and subsequent permeabilities. Isotropic permeability was assumed in our model, but this appears to be reasonable based on our experimental finding of minimal concentric pressure variation. Finally, our simulation efforts were not a priori, as an experimentally determined global permeability from one flow rate was required.

2.5   FUTURE WORK

Current efforts in the literature to predict the pressure drop characteristics of oxygenator fiber bundles have resulted in novel global (oxygenator-level) and local (fiber-level) approaches that may be applied to a three dimensional simulation [37, 60]. Approaches using such models could

conceivably obviate the need for experimental measures to determine critical variables such as permeability and could provide accommodation for fiber orientation effects in large-scale simulations. Improved instrumentation that permits accurate pressure measurement at the fiber scale within the bundle, through, for instance, fiber sized pressure transducers, could provide the data necessary to validate fiber-level modeling approaches. Although the pressure distributions predicted with porous media models should allow gross definition of the flow field, techniques used to predict oxygen transfer often require accurate local velocities to determine mass transfer coefficients. Because of concerns regarding the relationship between the true fluid flow pattern and the porous media approximation, flow visualization is a necessary adjunct to permit true validation of CFD predicted results.

3.0 FLOW VISUALIZATION IN HOLLOW FIBER MEMBRANE MODULES

As discussed in previous chapters, a fundamental relationship exists between the flow phenomena in a HFM module and the rate and amount of local gas exchange; for spatial models, an accurate flow solution is a prerequisite for further mass transport simulation. Basic fluid mechanics assumes that the proper combination of the equations of momentum and state can describe the relationship between pressure and flow in a given environment. However, the complex geometries and transport conditions found in HFM modules pose a challenge to the selection of representative but tractable model formulations. In Chapter 2, a computational model based on porous media assumptions was developed and implemented for use in predicting pressure-flow phenomena in HFM modules; the predicted pressure drops were compared to experimental data for model evaluation. In a similar vein, comparison of the experimental and model-predicted flow fields is the subject of the current chapter.

A computational model requires methodical validation on multiple levels before researchers can have confidence in its predictions. Models can be evaluated from a pure mathematical perspective, with rigorous assessment of the fundamental assumptions and derivations that result in the basic model structure and the numerical methods used for solution. A more practical but less rigorous approach might utilize model performance under known, real-world test conditions as an evaluation tool. Following the latter tactic, the current chapter describes the novel application of fluoroscopic imaging to fluid flow measurement in HFM modules, along with the development and testing of numerical methods involved in data extraction.

3.1 BACKGROUND

3.1.1 Flow Imaging Methods and Prior Application

Traditional methods of velocity measurement such as particle image velocimetry (PIV) and anemometry are poorly suited for application in hollow fiber membrane oxygenators due to their opacity and fiber cores. Some researchers have utilized CT [45, 52] to investigate device flow, however, the acquisition time required limits the spatio-temporal resolution of the result. Magnetic resonance imaging (MRI) has broad application to numerous flow regimes [61, 62], including turbulent 3D flow [63], but may have limitations in gas-filled systems such as HFM devices. In contrast, fluoroscopy can peer into the device interior and has a high spatial and temporal resolution capable of resolving rapid changes in fluid movement. The fluoroscopic data can be analyzed and compared to CFD predicted velocity fields. The performance features suggest that fluoroscopic imaging has promise as a tool for validating and extending computational simulations of hollow fiber membrane oxygenators. In addition, fluoroscopy is cheap, widely available and has recently been extended to 3D applications [64], albeit with a loss of temporal resolution. The current chapter outlines a novel application of fluoroscopic imaging to estimate the projected 2D velocity field inside a membrane oxygenator.

3.1.2 Overview of Fluoroscopic Imaging

Fluoroscopic imaging is the original radiographic visualization method. The apparatus used by W.C. Roentgen for his initial studies in 1895 utilized a barium platinocyanide screen that fluoresced when struck by the invisible 'x-rays' [65]. Despite its long tenure in the arsenal of radiologists, fluoroscopy remains a preferred technique for the observation of biophysical dynamics in real-time [66].

A number of factors impact the final quality of the image generated during fluoroscopy. The influence of these factors can best be assessed through consideration of the fluoroscopic imaging chain, which describes the components present in a modern fluoroscopic imaging system and can therefore show where signal degradation and data corruption can occur.
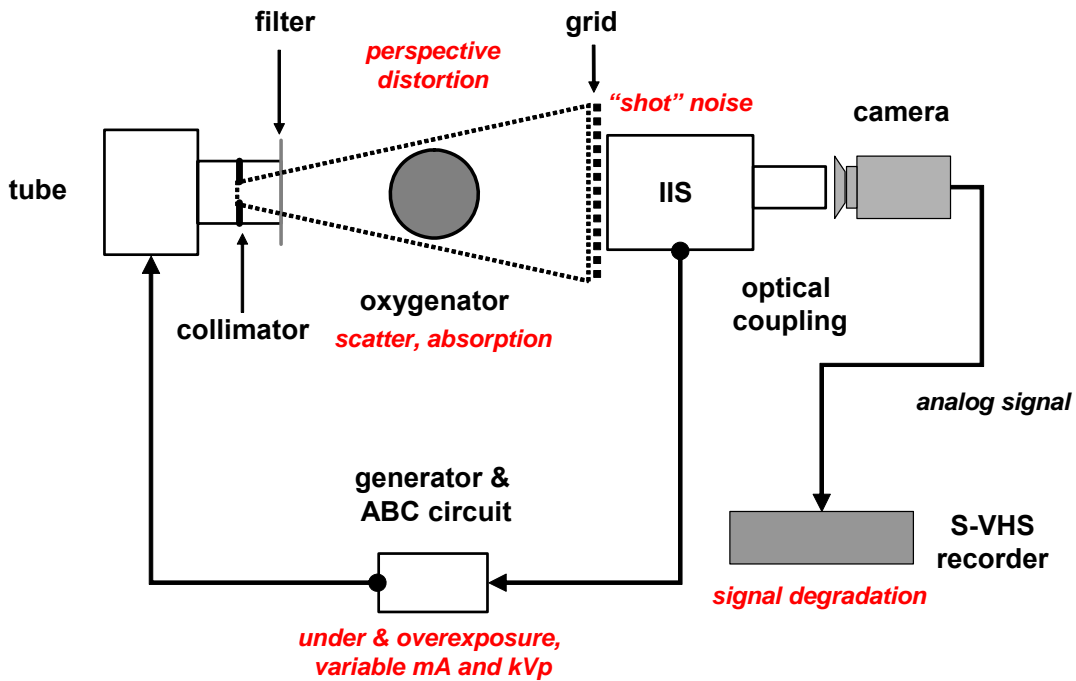
Figure 3-1 The fluoroscopic imaging chain with sources of error.

As shown in **Figure 3-1**, noise and data corruption arises from components within the imaging chain as well as from their interaction with the object being studied, which in this case is a membrane oxygenator. After x-rays are produced in the tube unit, they pass through the collimator, which can adjust the size of the beam from a large to small area depending on the clinical (or experimental) need. The x-rays then pass through a filter unit which is able to block low energy x-rays that do not have enough energy to penetrate the target and would result in increased radiation exposure without imaging benefit. Once past the filter, the x-rays then begin their interaction with the target being imaged and the surroundings. The x-rays do not emerge from the tube assembly on parallel paths but emerge in a cone pattern with an apex (**Figure 3-2)** on the focal spot where x-ray generation occurs. One major effect of the cone pattern is the production of perspective distortion in the final image whereby portions of the target closer to

the tube assembly are larger than in reality. Perspective distortion can have a major impact on flow imaging calculations as will be seen in later sections.
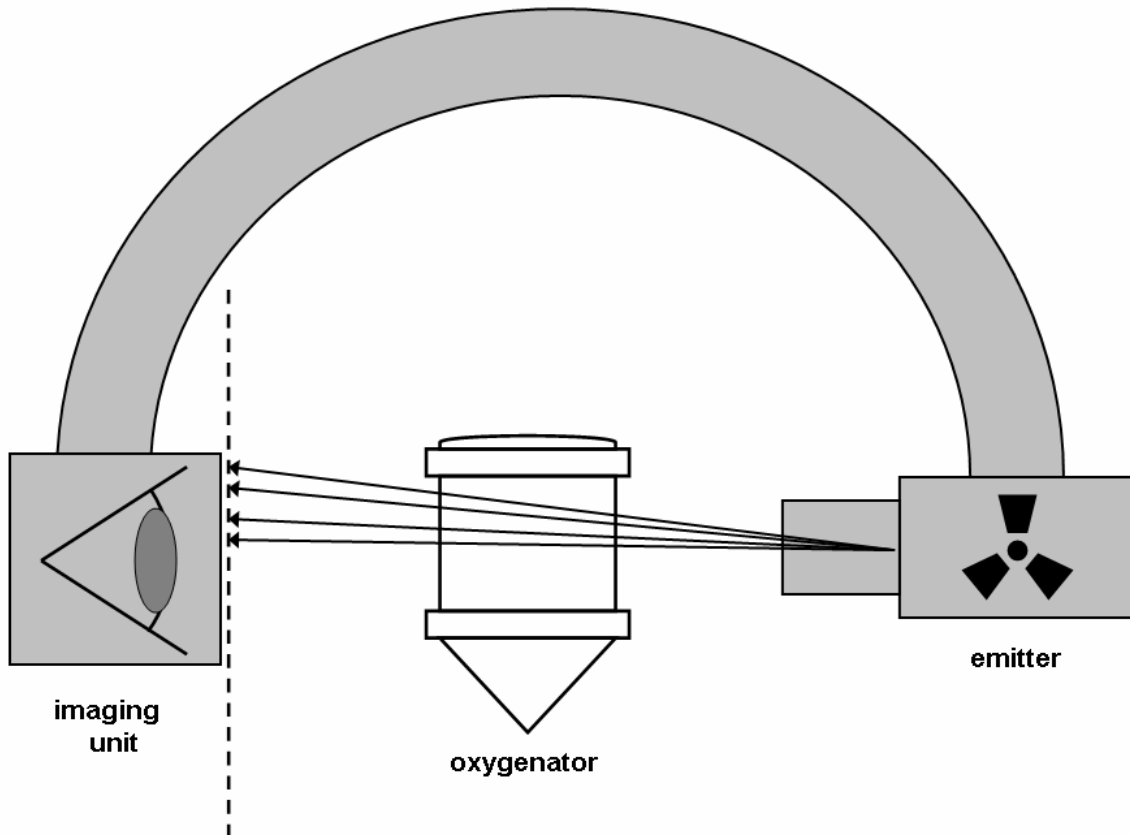
Figure 3-2 The "cone" shaped beam results in perspective distortion.

The interaction of x-rays with the target object is not completely benign. Despite filtering, some low-energy x-rays are absorbed and will be lost from the final image. Of greater concern is the impact of scattering whereby some x-rays are deflected and contribute to portions of the image that are not aligned with the original beam path. The net effect is to artificially lighten areas of the resulting image, resulting in brightness changes that are not related to motion or object density. A grid placed in front of the image intensifier system (IIS) attempts to minimize the effect of scattered photons by limiting the penetration of x-rays not aligned parallel

with the tube-IIS assembly. The IIS can be thought of as a photomultiplier unit whereby one photon entering the assembly is multiplied many, many times until a visible image is formed. Because the multiplication factor is so great, the potential corruption due to "shot" or electronic noise is significant as it will result in the triggering of the photon cascade where an original photon didn't exist. In most modern fluoroscopic imaging systems, the IIS is connected to an automatic brightness control (ABC) unit and a camera. The purpose of the ABC is to adjust the production of x-rays so that the resulting image is neither under or overexposed, which is useful from a clinical perspective. However, from an experimental perspective the ABC is undesirable because the adjustment results in global changes in image brightness which can affect the quantification of the data. Fortunately, the ABC feature can be disabled in most systems. Additional error can enter the image sequence depending on the method of recording. Most modern fluoroscopes are digital and there is no analog-to-digital conversion taking place. In older units, the camera converts the image into an analog TV signal that is then either recorded digitally or upon magnetic tape. The conversion process can result in data loss in some cases and magnetic tape is vulnerable to aging and corruption.

3.1.3   Overview of Optical Flow Calculation

Fluoroscopic imaging results in the acquisition of a series of images that contain "flattened" data; the contrast concentration information for the 3D device has been projected onto a 2D plane and recorded. In addition to the lossy compression from 3D to 2D, the data is further corrupted with various noise and summations, resulting in a somewhat grainy 2D representation of flow through a 3D object. Fortunately, computer scientists researching robust robotic vision have developed a set of methods to tease out the velocity of moving objects in similar images. A conceptual overview of these methods is now presented.

Recovering optical flow velocities from an image sequence can be viewed as a minimization procedure. The velocities obtained from the use of a specific conservation model (as applied to the brightness pattern) is balanced against a smoothness estimate for the calculated velocities.

$$\min \iint \left(\xi_c + \alpha\, \xi_{s_1} + \beta\, \xi_{s_2} + \cdots \right) dx\, dy$$

continuity constraint   smoothness constraints

Figure 3-3 Optical flow calculation as a minimization problem.

The continuity constraint is most often based on the assumption that the brightness of a point in a moving pattern is constant over time [67]. Beginning with the total brightness derivative, a single equation relating the two unknown (planar) velocities can be derived.

$$\frac{dE}{dt} = 0 \qquad\qquad \textbf{Equation 3-1}$$

$$\frac{\partial E}{\partial x}\frac{dx}{dt} + \frac{\partial E}{\partial y}\frac{dy}{dt} + \frac{\partial E}{\partial t} = 0 \qquad\qquad \textbf{Equation 3-2}$$

$$E_x u + E_y v + E_t = 0 \qquad\qquad \textbf{Equation 3-3}$$

The under-determined final equation requires some constraint to relate the two velocities and result in an appropriately determined system. The origin of this effect is due to what is commonly referred to as the aperture problem. The aperture problem can be described by considering a system with a uniform brightness gradient in one direction. Movement in a direction perpendicular to the gradient cannot be visualized since this movement does not result in a brightness change [68]. A common constraint is one of smoothness based on limiting the square of the calculated velocity gradient.

$$\xi_s = \left(\frac{\partial u}{\partial x}\right)^2 + \left(\frac{\partial u}{\partial y}\right)^2 + \left(\frac{\partial v}{\partial x}\right)^2 + \left(\frac{\partial v}{\partial y}\right)^2 \qquad\qquad \textbf{Equation 3-4}$$

A number of constraints have been applied by different authors to overcome the limitations of the above constraint, which tends to "bleed" velocity into non-moving areas. An overview of the different optical flow models and constraint equations are shown below in **Figure 3-4.**

Optical Flow Models & Constraints

model	continuity constraint	smoothness constraints
Horn-Schunck	$\left(E_x u + E_y v + E_t\right)^2$	$\left(\frac{\partial u}{\partial x}\right)^2 + \left(\frac{\partial u}{\partial y}\right)^2 + \left(\frac{\partial v}{\partial x}\right)^2 + \left(\frac{\partial v}{\partial y}\right)^2$
Wildes, et. al.	$\left(E_x u + E_y v + E u_x + E v_y + E_t\right)^2$	$\left(\frac{\partial u}{\partial x}\right)^2 + \left(\frac{\partial u}{\partial y}\right)^2 + \left(\frac{\partial v}{\partial x}\right)^2 + \left(\frac{\partial v}{\partial y}\right)^2$
Cornelius-Kanade	$\left(\frac{dE}{dt} - E_x u - E_y v - E_t\right)^2$	$\left(\frac{\partial u}{\partial x}\right)^2 + \left(\frac{\partial u}{\partial y}\right)^2 + \left(\frac{\partial v}{\partial x}\right)^2 + \left(\frac{\partial v}{\partial y}\right)^2$ $\left[\frac{\partial}{\partial x}\left(\frac{dE}{dt}\right)\right]^2 + \left[\frac{\partial}{\partial y}\left(\frac{dE}{dt}\right)\right]^2$

Figure 3-4 Optical flow models and constraints.

The combined continuity and brightness constraints are then minimized over the image sequence (or some portion thereof) to produce a 2D estimate of the velocity field. The process is shown graphically in **Figure 3-5**.
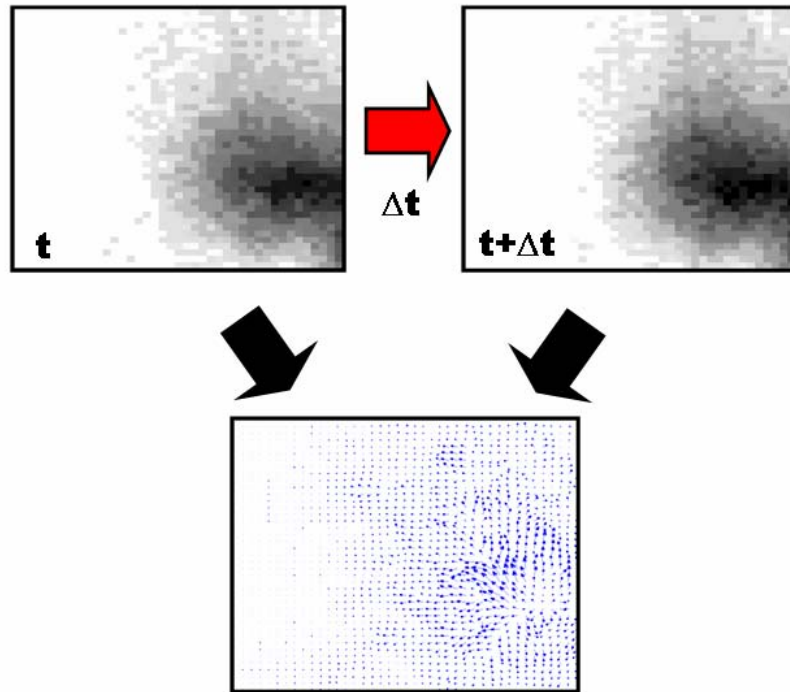
Figure 3-5 Graphical description of the optical flow calculation process.

3.2   MATERIALS AND METHODS

3.2.1   Experimental Methods

A novel recirculation loop (**Figure 3-6**) was constructed to permit constant speed injection of radiographic contrast into an extracorporeal hollow-fiber membrane oxygenator (Medtronic Maxima™, Medtronic, Anaheim, CA, U.S.A.). Two three-way solenoid valves (Automatic Switch Co., Florham Park, NJ, U.S.A) divided a section of the loop into separate flow paths, one of which contained the contrast bolus. During normal (i.e., unenergized) operation, the fluid would flow through the contrast-free tubing. When triggered, the valves redirect the moving

fluid into the alternate tubing path, convecting the contrast bolus into the oxygenator. A clinical blood pump (BP-80 Biopump and 520D Bioconsole, Biomedicus, Eden Prairie, MN, U.S.A.) provided smooth, continuous flow in the circulation loop. The target flow rate of 4 liters per minute (L/min) was an average of rates encountered during normal operation of the Medtronic Maxima™ (1 to 7 L/min). A turbine flowmeter (FTB2002, Omega Engineering Inc., Stamford, CT, U.S.A.) provided the flow rate measurement. The blood pump utilized was capable of flow rates up to 10 L/min.

Experiments were performed at room temperature using a glycerin-water (35% / 65%) blood analogue as the motive fluid. A Cannon-Fenske capillary viscometer (Cannon Instrument, State College, PA, U.S.A.) and hydrometer (Fisher Scientific, Pittsburgh, PA, U.S.A.) established the viscosity and density of the blood analogue. The bolus consisted of an ionic iodinated contrast agent (Renografin-60®, Bracco Diagnostics, Princeton, NJ, U.S.A.) diluted with water.

Radiographic imaging was performed using a standard portable C-arm fluoroscope (Series 9000, OEC-Diasonics, Salt Lake City, UT, U.S.A.) attached to a SVHS video recording unit (Panasonic AG-7300 VTR, Matsushita Electrical Industrial Co., Ltd., Osaka, Japan), which records at 30 frames/sec. The tube voltage (kVp) and excitation energy (mAs) were chosen prior to contrast injection to maximize the subjective image quality, and the recording process was triggered automatically when the emitter unit was active. The oxygenator was imaged in both profile and frontal views as defined by a dividing symmetry plane that passes through the center of outflow port.
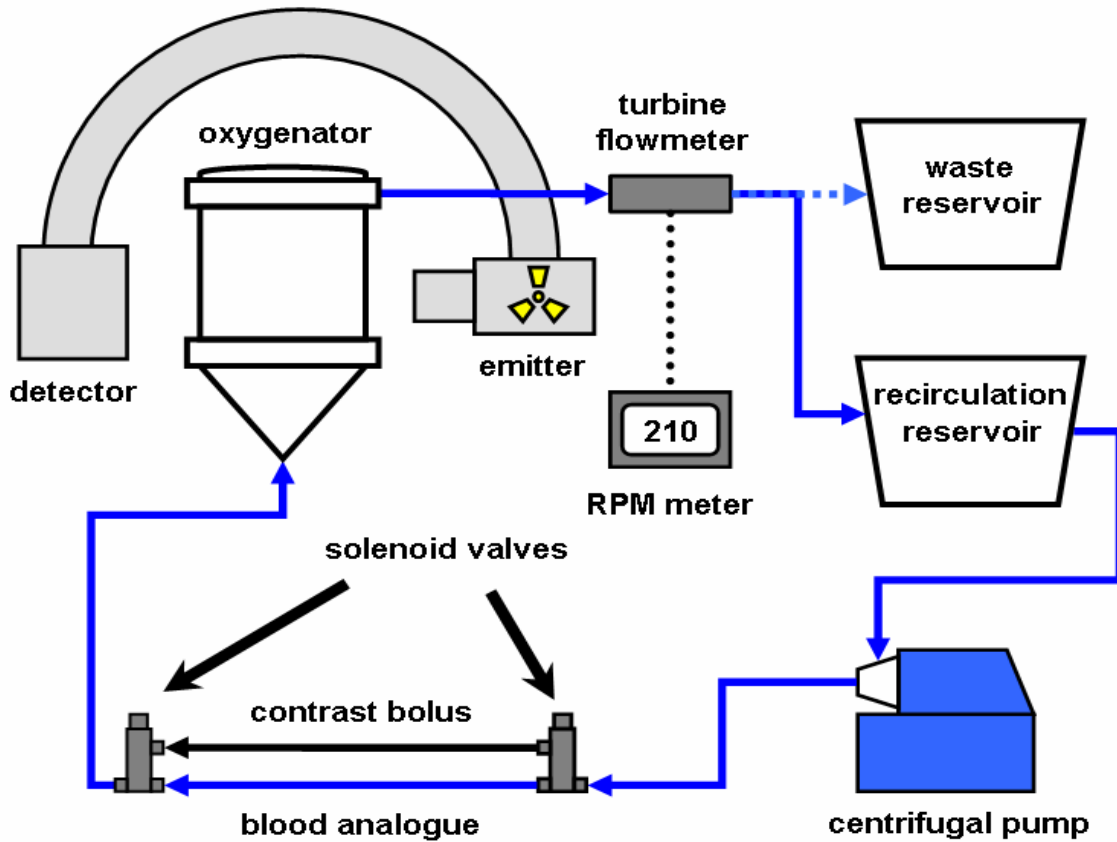
Figure 3-6 Experimental flow loop for contrast injection.

3.2.2 Computational Model

The computational grid developed to discretize the governing equations is described in a previous publication [50] and in Chapter 2. In summary, the midline symmetry of the Medtronic Maxima™ membrane oxygenator was utilized to create a three-dimensional tetrahedral mesh encompassing one-half of the device geometry and containing approximately 240,000 cells. The modeled portion omitted the heat exchanger and included the inflow diffuser, fiber bundle region, and outflow fluid collection ring.

A time-dependent solution procedure was used to simulate the temporal movement of the contrast agent into the oxygenator. The contrast agent and blood analogue were modeled as a mixture possessing the same physical properties as the blood analogue alone. The mixture assumption allows the momentum and species transport equations to be uncoupled and solved independently. Our approach was to calculate the steady state velocity field inside in the oxygenator using the properties of the blood analogue and appropriate boundary conditions. The converged flow solution provided the velocimetric terms for the species transport equation, which was solved separately as a function of time. Convergence was achieved at each timestep prior to progression.

3.2.2.1 Boundary Conditions

The physical properties and boundary conditions used in the simulation were selected to approximate the experimental settings described earlier. Laminar, steady flow was assumed for solution of the momentum equations. A plug velocity profile was chosen for the modeled inflow region to approximate the well-mixed outflow of the heat exchanger. A constant gauge pressure of zero was assumed at the device outflow. The no-slip condition was applied to the oxygenator wall areas, and a symmetry condition was applied along the device midline.

3.2.2.2 Porous Media Approximation

The computational expense required to simulate the flow pattern around individual fibers precludes this approach except for the smallest bundles. Because of this limitation, porous media models are often used to approximate the momentum losses due to the fibers [35, 50]. The current work utilizes a Darcian porous media model (**Equation 3-5**) to account for the viscous drag due to fluid movement through the fiber bundle.

$$\nabla p = -\frac{\mu}{\alpha}\mathbf{v}$$
<div align="right">**Equation 3-5**</div>

Experimental data [50] were used to determine an isotropic permeability α characteristic of the Maxima™.

The pressure drop correlations that provide an experimental foundation for porous media models are often developed using the superficial velocity, which is the velocity of fluid passing through the porous domain if the obstructing media were ignored. The superficial velocity is

lower than the true, interstitial fluid velocity, and can be related to the interstitial velocity through the following equation

$$v^{\text{sup}\,er} = \gamma v^{\text{int}\,er}$$ **Equation 3-6**

where γ represents the porosity of the porous media [69]. Note that the contrast bolus will move through the oxygenator at the true, interstitial velocity rather than the superficial velocity.

When **Equation 3-6** is introduced into the standard momentum conservation equation, the resulting form is as follows [55],

$$\frac{\partial(\gamma\rho\mathbf{v})}{\partial t} + \nabla\cdot(\gamma\rho\mathbf{v}\mathbf{v}) = -\gamma\nabla p + \nabla\cdot(\gamma\boldsymbol{\tau}) + \gamma\mathbf{B}_{\text{force}} + \gamma S$$ **Equation 3-7**

where **B**force represents a body force such as gravity, and S represents the viscous and possible inertial momentum losses due to the interaction of the fluid and the fiber bundle. Use of the interstitial or physical velocity formulation allows spatially accurate time-dependent simulations to be performed with a convected species, which in this case would be the contrast bolus. The commercial finite volume code FLUENT 6 (Fluent, Inc., Lebanon, N.H., U.S.A.) was used to discretize the momentum and species transport equations and solve them in an uncoupled, time-dependent approach.

3.2.3   Image and Data Processing

The analog tape acquired from the fluoroscopic SVHS recorder was digitized using a visual workstation (Power Macintosh G3, Apple Computer, Cupertino, CA, U.S.A) equipped with a digital capture board and software (Adobe Premiere, San Jose, CA, U.S.A.) Still images (320 x 240 pixels) were generated for each frame.

The image brightness patterns are the result of the variable attenuation of x-ray photons caused by the intervening device, fluid, and contrast agent. The radiographically dense contrast scatters and absorbs more x-ray photons than the surrounding structure and therefore appears darker. A higher concentration of contrast results in a greater level of local attenuation, and the total extent of attenuation is a function of the amount of contrast encountered along the beam path. The image brightness pattern is therefore related to the two dimensional projection of the volumetric contrast concentration.
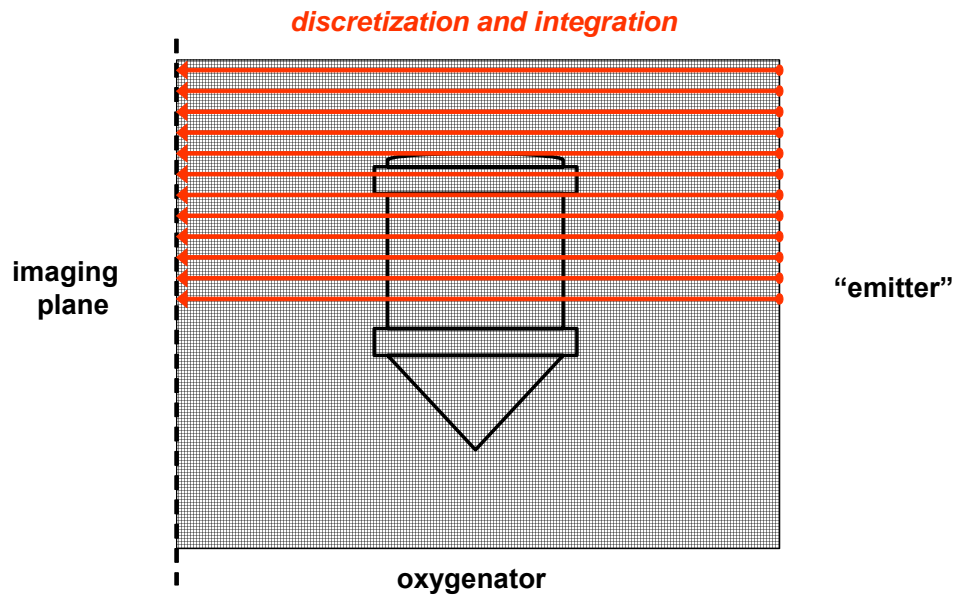
Figure 3-7 Overview of the orthogonal projection technique.

The three dimensional, time dependent species concentration data from the CFD simulations were transformed via a projection technique to create a 2D sequence analogous to the fluoroscopic results. The species concentration data present at the nodes of the irregular tetrahedral mesh were remapped onto a regular, rectangular grid using spatial interpolation. The remapped spatial concentration data was then integrated in the direction normal to the viewing plane to produce a two dimensional map of contrast concentration. **Figure 3-7** presents an overview of the orthogonal projection process in a graphical format. Of note, the remapping and projection technique utilized does not account for the cone shape of the emitted x-ray beam and the resulting perspective distortion present in the experimental fluoroscopic images. An alternative projection technique that would account for the perspective distortion is outlined in the Future Work section of the current chapter. **Figure 3-8** shows both an experimental fluoroscopic and CFD predicted, postprocessed bolus time-matched to the point when the contrast first enters the oxygenator bundle. These sequences would then be analyzed using an optical flow method described in the next section.
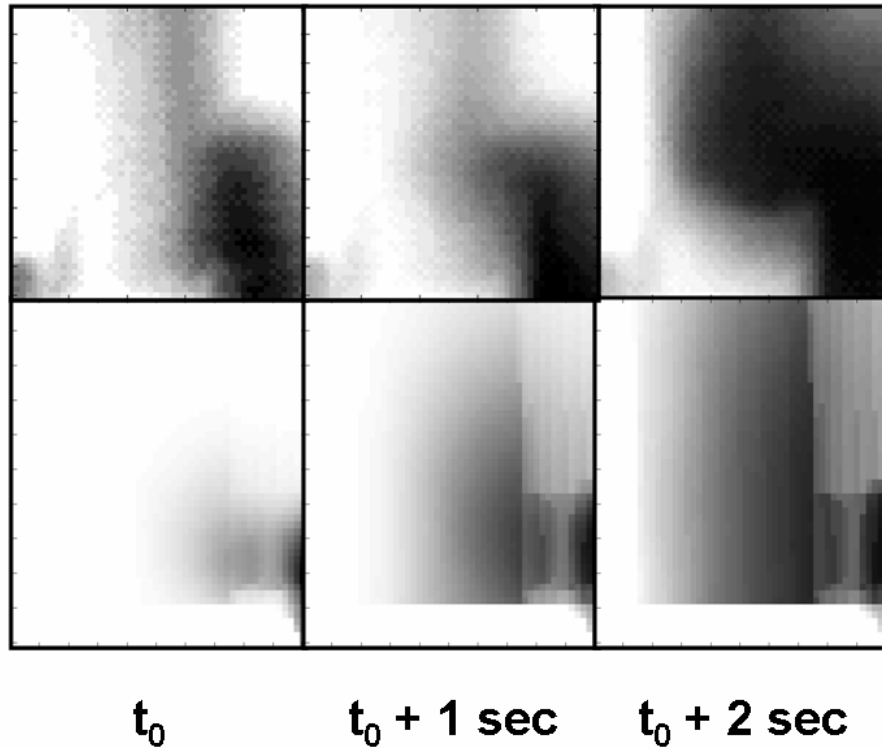
Figure 3-8 Frames from the fluoroscopic (top) and CFD image (bottom) sequences.

3.2.4 Calculation of Optical Flow

The Horn and Schunck method for calculation of optical flow was used to estimate the velocity field using the image sequences [67]. A major assumption in the Horn and Schunck approach is that the brightness changes present in the image sequence are due to movement of an underlying texture or pattern in the viewed scene; in essence, the brightness is conserved for each scene location. The assumption can be expressed as a differential equation

$$\frac{dE}{dt} = 0 \hspace{4cm} \textbf{Equation 3-8}$$

where E is the brightness measure. Expansion via the chain rule results in a differential equation relating brightness changes to movement in the underlying scene

$$\frac{\partial E}{\partial x}u + \frac{\partial E}{\partial y}v + \frac{\partial E}{\partial t} = 0$$

<div align="right">**Equation 3-9**</div>

where u and v are the apparent projected velocities of the viewed field. Inspection of the equation reveals two unknowns (u and v), so the system is undetermined. An additional constraint equation was imposed which assumes a smooth change in the brightness gradient and the calculated velocities, as outlined in Horn and Schunck's original manuscript [67]. The sum of the squares of the brightness gradient

$$\varepsilon^2 = \left(\frac{\partial u}{\partial x}\right)^2 + \left(\frac{\partial u}{\partial y}\right)^2 + \left(\frac{\partial v}{\partial x}\right)^2 + \left(\frac{\partial v}{\partial y}\right)^2$$

<div align="right">**Equation 3-10**</div>

is minimized as part of a solution technique that balances the smoothness of the resulting velocity field with the agreement to the actual recorded data. Further details are available in the original reference [67].

Two additional modifications were made to reduce the computational expense of the flow visualization technique and potentially improve precision. A 50 x 50 pixel region of interest (ROI) was selected from the 2D projections to encompass the corner of the inflow bundle nearest the outflow port as shown in **Figure 3-9**. The decrease in the number of pixels (320 x 240 are present in the original digital fluoroscopic images) provides a significant reduction in computational expense required for remapping of the irregular data, and minimizes the involvement of non-device pixels in the global smoothing calculation. The ROI also encompasses an area found to be prone to thrombus formation in previous experiments [35].
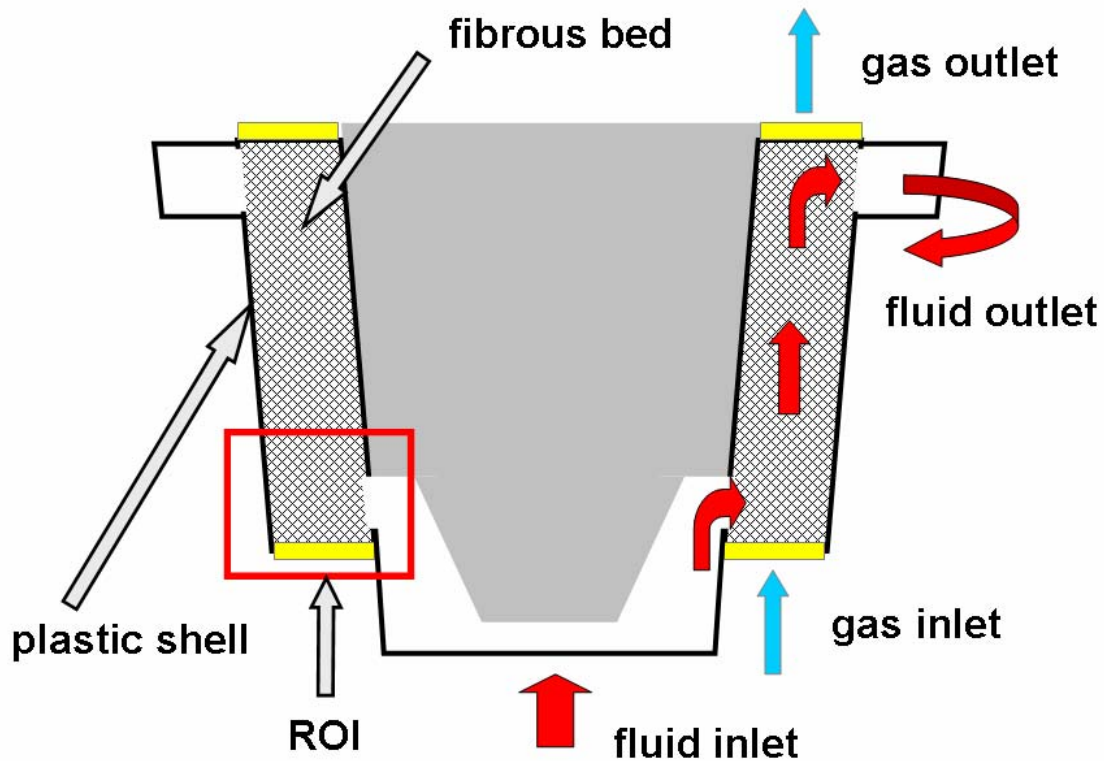
Figure 3-9 A 2D view of the Medtronic Maxima™ with the ROI indicated.

The second modification involved the use of spatio-temporal brightness information to determine the optimal frames in the image sequence for local velocity calculations. Prior to the arrival of the leading edge of the contrast bolus, the brightness at a pixel location will be almost constant. The brightness will change as the contrast leading edge enters the pixel location, becoming constant again (at a lower brightness value) as the bulk of the contrast arrives. In effect, the value of the brightness time derivative is close to zero prior to and after the arrival of the contrast bolus, and peaks as the leading edge appears in the pixel. The large change in brightness value around the arrival of the leading edge reduces the effects of noise on the velocity calculation that would be encountered if a more gradual change in brightness were used. The maximum brightness time derivative at each pixel location was used to select the image frame used for the velocity calculation for that pixel, a velocity that should be constant under the

steady flow assumptions used herein. It is important to note that the contrast bolus itself is not followed through the images; the velocity calculation procedure assumes that pixels with the largest brightness gradient possess the highest signal-to-noise ratio and represent the leading edge of the bolus. **Figure 3-10** reveals maps of the maximum brightness time derivative for both the computational and experimental image sequences. Note the similarities in the general pattern of contrast edge penetration into the bundle zone, indicating that the approach used does indeed provide some information about the location of the contrast leading edge.
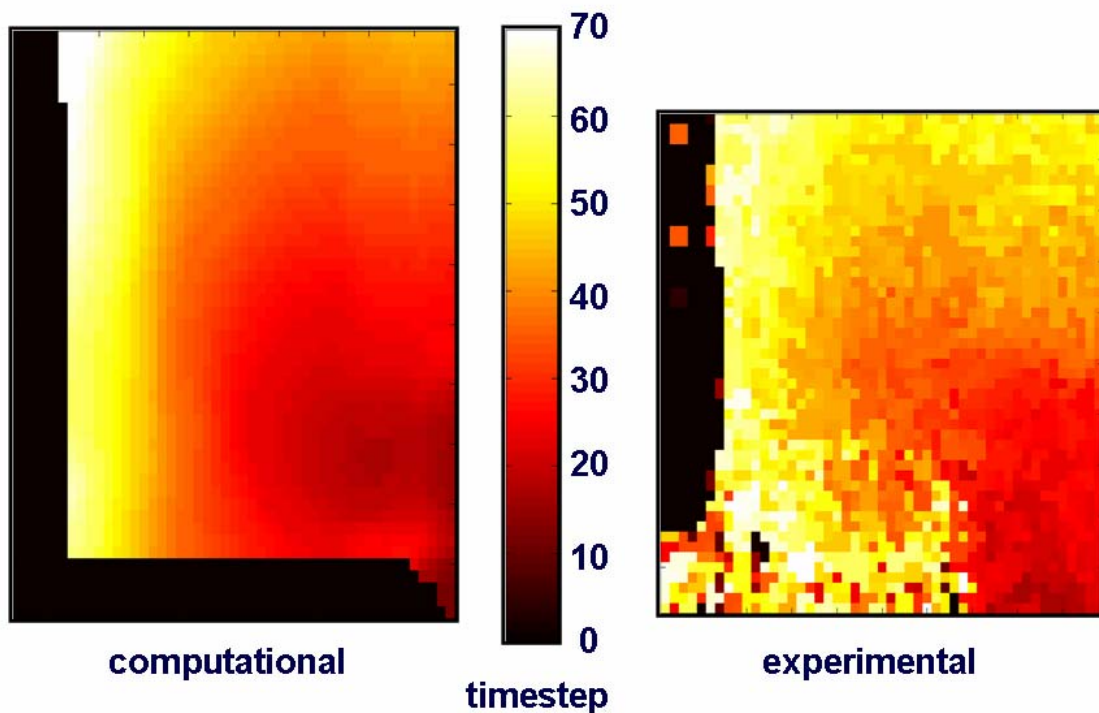
Figure 3-10 A spatial map of the maximum brightness time derivative is shown.

The final set of equations based on the ROI was solved on a personal computer using a Gauss-Seidel iterative procedure in the MATLAB numerical programming language (MATLAB

R12, MathWorks Inc, Natick, MA). The brightness derivative information indicated which timesteps were included in the ultimate velocity field at each pixel location.

3.3   RESULTS

3.3.1   Validation Studies

It is common practice to evaluate optical flow algorithms using standardized test sequences. A test sequence generator is included in **Appendix A** and is capable of generating some of the test sequences used for validation purposes in Horn & Schunck's original manuscript [67]. The figure below includes a sampling of the initial frames of a translational test sequence. The sequences often used gradient brightness patterns or orthogonal sinusoidal patterns to provide adequate contrast for algorithm function.

As seen in **Figures 3-11 and 3-12**, the optical flow algorithm exhibits rapid convergence for the test sequence. The results are compared to a "ground truth" velocity map that contains the actual image displacement velocities. It should be noted that the validation uses a simple translating pattern with uniform movement throughout the image field; each frame of the sequence adds additional data without change in speed or direction. In contrast, the experimental sequences obtained from the CFD and fluoroscopic images demonstrate change of speed and direction within the image field.
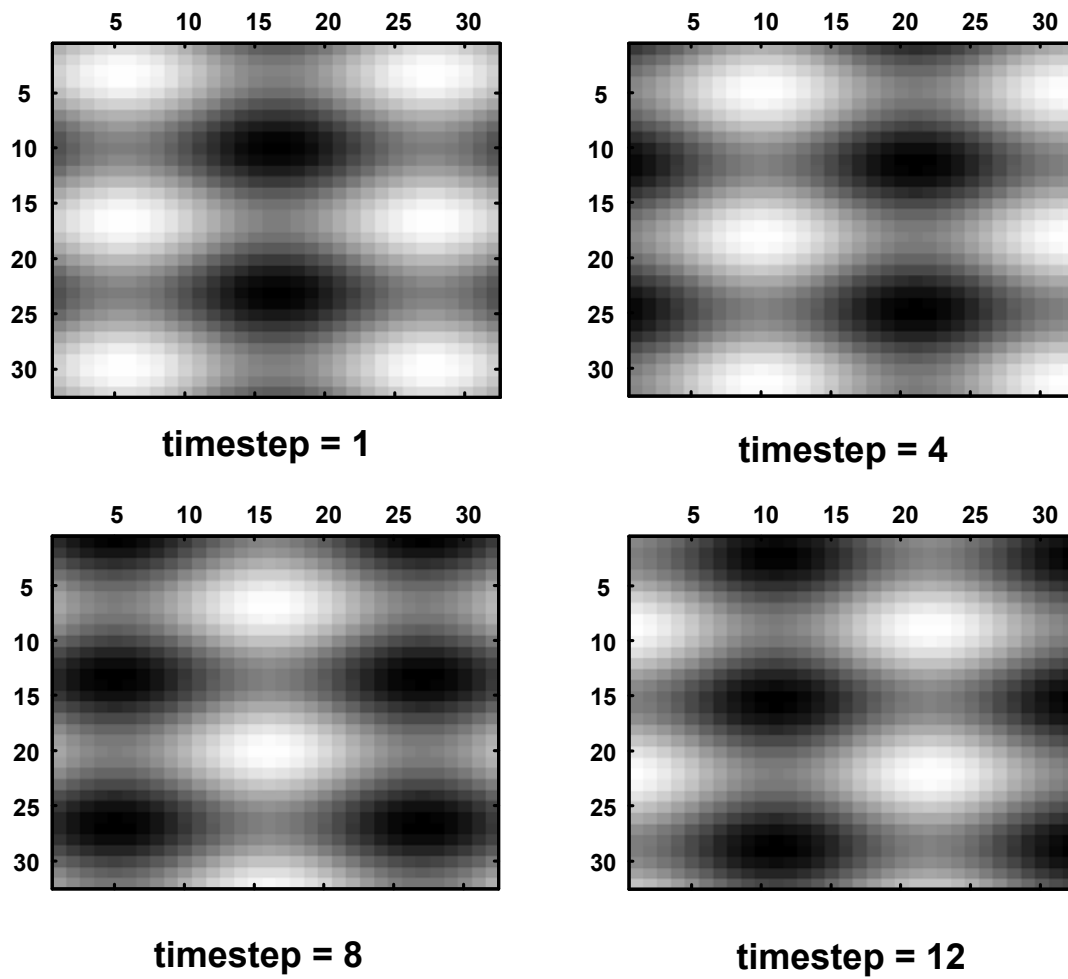
Figure 3-11 Sample frames from a translating brightness pattern.
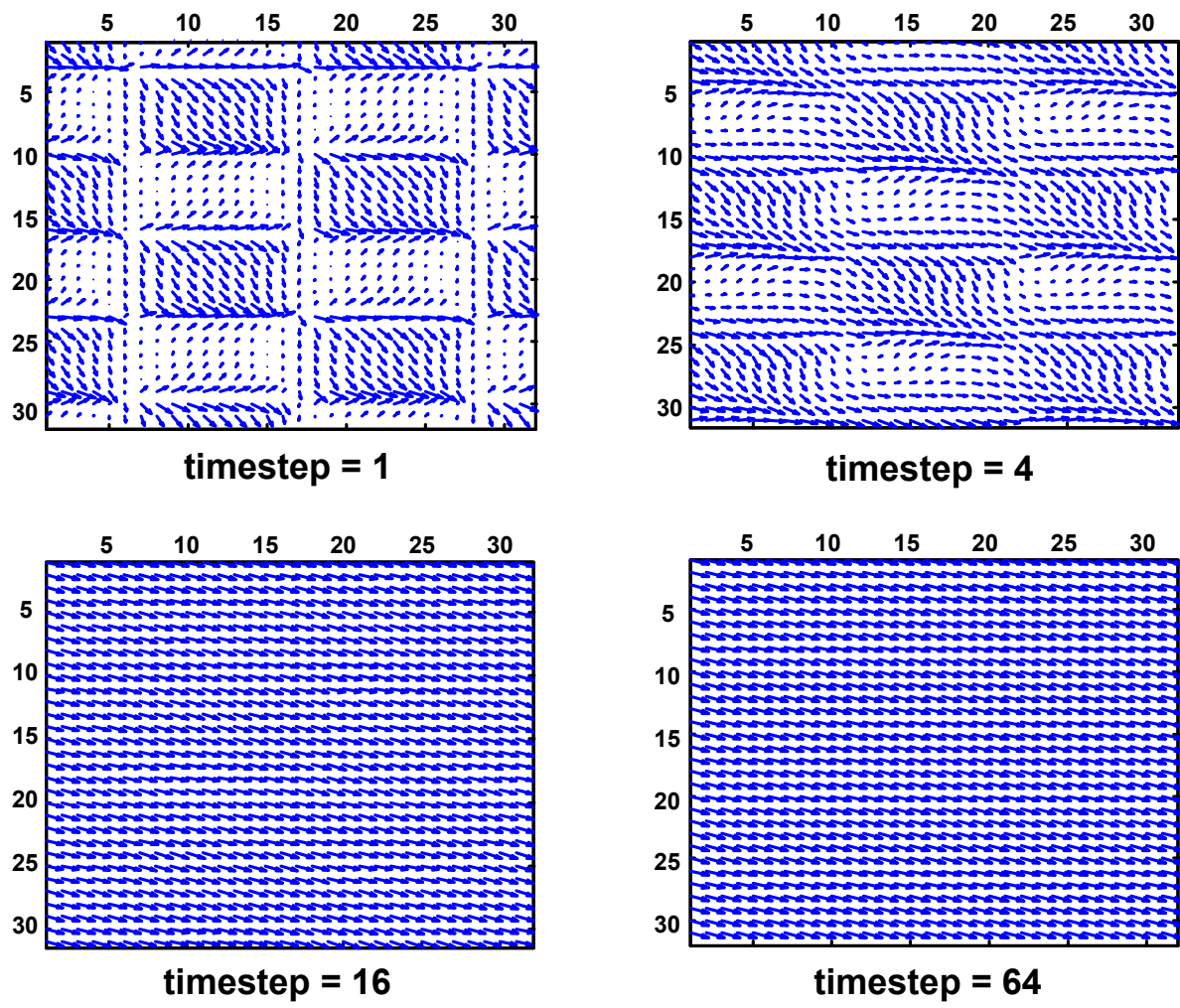
Figure 3-12 Quiver plot demonstrating convergence of HS algorithm for translating pattern.
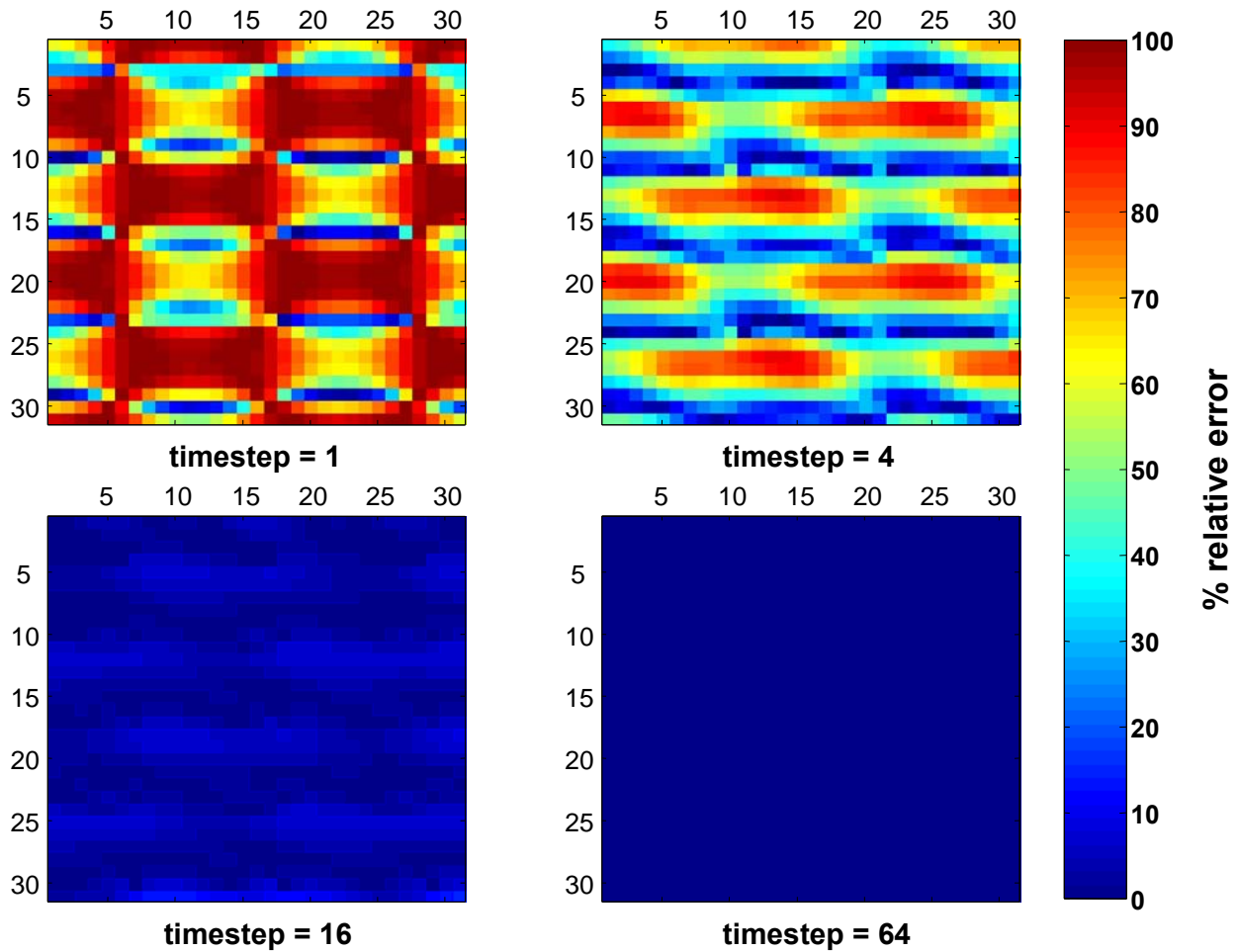
Figure 3-13 Reduction in percent relative error in velocities as a function of timestep.

The Horn-Schunck algorithm performs as expected, although generalization of the positive results to real-world sequences such as the ones from the CFD and fluoro studies should not be assumed. Real-world sequences suffer from corruption and noise that could have a significant impact on the algorithms' convergence and accuracy.

3.3.2 Experimental Results

The purpose of the present work was to demonstrate the use of fluoroscopic imaging as a tool for verification of oxygenator flow fields predicted using computational fluid dynamics. As **Figures 3-14 and 3-15** demonstrate, there is semi-quantitative agreement between the predicted and

experimental flow fields, with both revealing strong similarities in the general flow pattern and absolute flow speed.
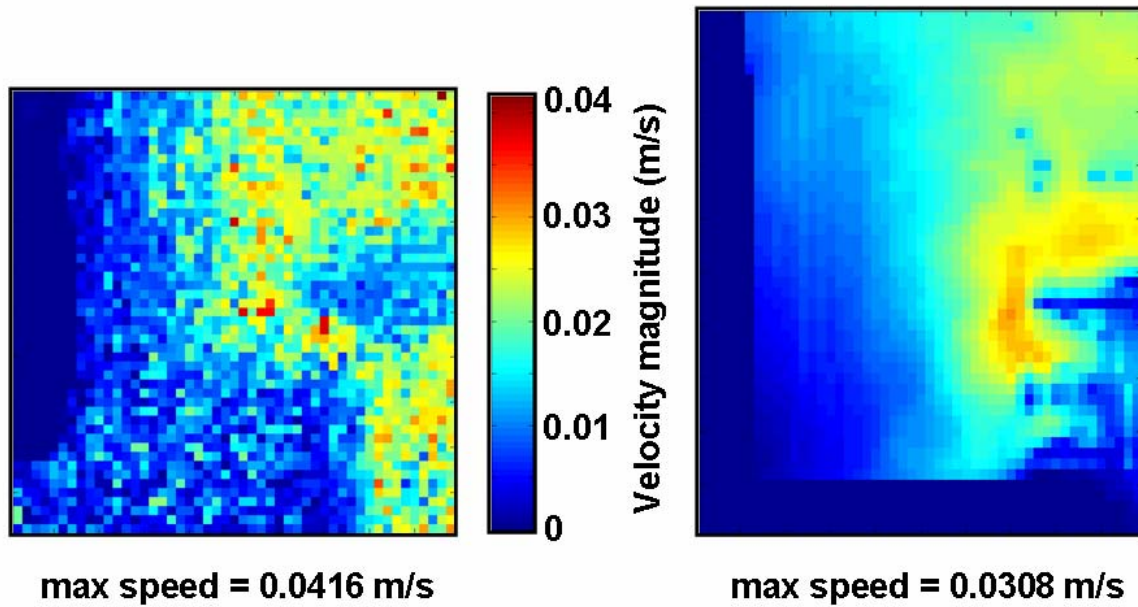
Figure 3-14 The (L) experimental and (R) predicted velocity magnitudes are shown.

The largest velocity in the experimental result was greater than that predicted from the simulation. However, the scattered distribution suggests that the high values could be the result of noise. The vector plots in **Figure 3-15** show less agreement, although some of the aberrant features of the experimental data could be due to the lack of background subtraction prior to velocity calculation. The contrast bolus is primarily moving toward the top and top-left. The divergence in the experimental vector field could be due to the effect of the dark oxygenator housing upon the Horn-Schunck velocity calculation.
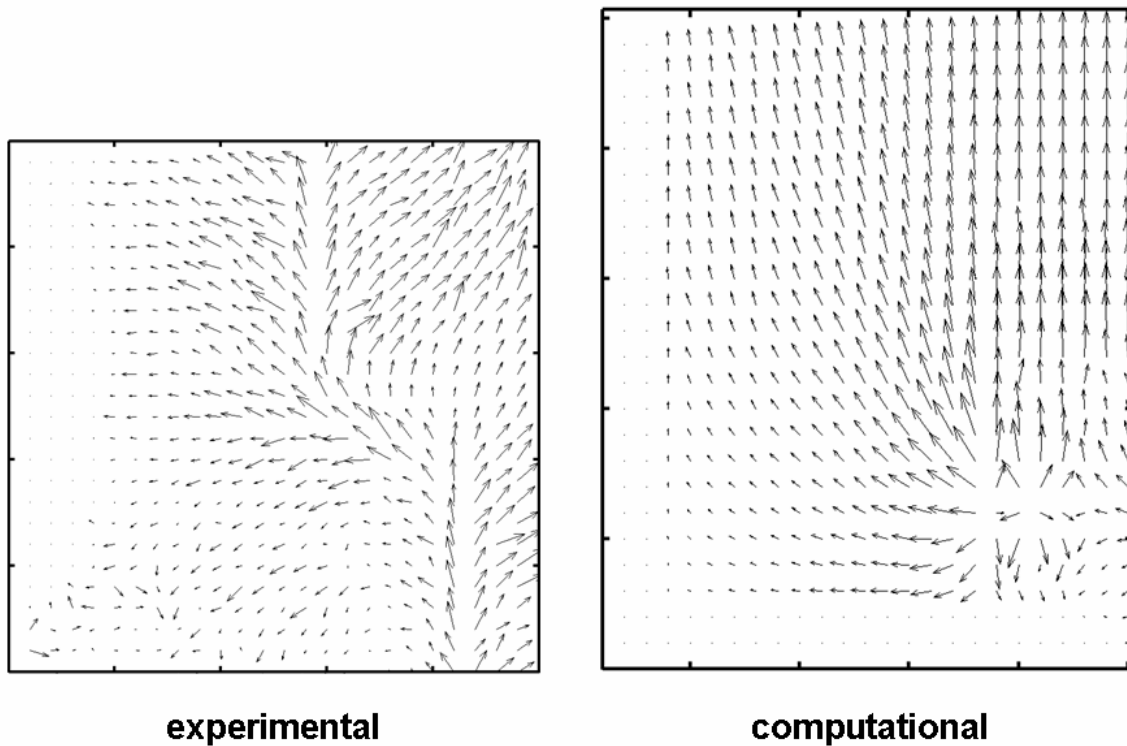
Figure 3-15 The velocity vector fields calculated using the HS method are shown.

3.4   DISCUSSION

A number of changes can be incorporated into the current approach that could improve the accuracy of the velocity field calculation. The fluoroscopic images used in the current manuscript were obtained with the entire oxygenator in the field of view; the result is that few pixels are present in a given frontal location in the oxygenator, reducing the spatial accuracy of the velocity field prediction. However, it is possible to zoom into an area of the oxygenator by moving the device closer to emitter. This approach would be useful for areas such as the corner bundle zone, where areas of concern have been recognized in the literature. Spatial accuracy could be improved with a higher resolution fluoroscopic unit, and all-digital equipment would eliminate a number of analog-to-digital conversion steps that degrade the image quality. In

addition, temporal accuracy would be improved through the use of a cardiac fluoroscopic unit, which has a higher frame rate of capture than a general fluoro unit (approx 150 vs. 30 frames/sec).

Fluoroscopic images are often considered to possess a low signal to noise ratio and suffer from a number of degradation effects due to the method of image acquisition [66]. Some of these effects are represented in **Figure 3-1** and include image degradation due to scattering, divergence, and analog to digital signal conversion. In contrast to other imaging modalities, such as MRI, where the acquisition unit is built around a single point of reference, many fluoroscopic units are portable, making a defined reference point difficult to achieve. This limitation has a significant impact on determination of an absolute spatial resolution for the data reported in this work. This limitation could be partially overcome by employing fixed and bi-plane fluoro units or by calibration of the unit with fixed spatial markers. Portable fluoro units were employed due to their relative availability and the difficulties/costs associated with obtaining access to fixed units. In retrospect, an approach that might have addressed the spatial resolution question would have been to place a geometrically defined, radio-opaque marker within the oxygenator body. This marker could have been used for spatial determination.

Beam divergence and the resulting image distortion would result in a difference between the projected CFD results and the experimental data even if perfect flow prediction would have been achieved. The best approach to accommodating the beam divergence would have been to use a perspective image transformation of the CFD data rather than a simple orthogonal projection. At the time the research was performed, the impact of the divergence was not appreciated. Using modern volume imaging software and toolkits such as ParaView and VTK (Kitware, Clifton Park, NY, U.S.A) a perspective volume transformation can be performed without extensive code writing or excessive effort.

Fluoroscopic imaging suffers from a fair amount of image noise due to scattering, whereby an x-ray is deflected off the nucleus of an atom within the target, thereby providing its energy to a portion of the image detector not aligned with the original beam. This results in brightness changes that are not related to image movement and can thereby degrade the velocity calculations, which depend solely on the brightness field for their calculation. Noise is introduced into the final images from other phenomena as well, and calculation of the cumulative effect upon the resulting velocity field is a substantial undertaking that requires a stochastic

modeling approach of the fluoroscopic imaging chain for accurate predictions. A more reasonable undertaking would be to "corrupt" the ideal test images with an ideal noise source and evaluate the effect on velocity prediction. This approach would be a worthwhile goal for future research to determine the absolute limitations of the fluoroscopic imaging approach described here.

Changes in the method of analysis could also improve the calculated field accuracy. The Horn and Schunck approach is classified as a gradient based method for the calculation of optical flow [70]. Other gradient-based and hybrid methods are better equipped to handle certain anomalies (i.e., occlusions in the field of view) which challenge the underlying assumptions of the Horn-Schunck approach. Fourier phase-based methods have also been shown to produce a more accurate calculated flow field when tested with both real and simulated image sequences [70] and offer an alternative to gradient-based methods.

Despite these limitations, the fluoroscopic technique described herein provides valuable velocity field information suitable for comparison with computationally predicted flow fields. The imaging and analysis method shows promise as a tool for the evaluation of various hollow fiber membrane oxygenator models, including the basic porous media assumptions used in many oxygenator CFD simulations.

3.5   FUTURE WORK

Assuming that the limitations outlined in the above discussion section could be addressed, fluoroscopic imaging would remain a projection based imaging method requiring considerable post-processing and data analysis to provide high-quality velocity information. At the present stage, quantitative comparisons between the simulated and experimental velocity fields are unlikely to result in further insight because the impact of image corruption and noise has yet to be accurately determined and would require a substantial effort. However, once the resulting images were corrected for the effects described above, one could perform a point-by-point (or pixel-by-pixel) comparison of the velocity fields with calculation of agreement statistics (average deviation, min and max deviation, etc).

As indicated in previous sections, orthogonal projection of the CFD dataset does not provide a faithful recreation of the fluoroscopic imaging process, which results in a perspective view of the oxygenator and its contents. The limitation of the orthogonal projection is significant and the development of a perspective projection method would be a logical first step toward improving the qualities of the simulated image data. However, volume visualization of unstructured datasets such as those generated during CFD simulations remains a significant challenge compared to datasets with regular connections (e.g., CT and MRI) [71].

There are a number of methods for visualizing the unstructured CFD dataset as a perspective image analogous to a fluoroscopic view of the oxygenator, including *remapping, projection* (or *splatting*), and *raycasting* [71]. *Remapping* involves mapping the current unstructured data onto a regular grid, which then permits the use of advanced algorithms developed for regular datasets. Remapping was used in the current work, where its limitations (excessive compute time and memory usage) led to a field-of-view restriction to reduce the computational requirements to a reasonable level. *Splatting* can take advantage of the polygon rendering hardware in most workstations and involves projecting the cells onto the viewing plane in succession, building a final image from the contribution of each cell [71]. However, *raycasting* offers the advantage of higher accuracy in the final image [71] and closely mirrors the physical process of an x-ray beam as it passes through an oxygenator **(Figure 3-16)** . Image accuracy is a primary concern as the projected image data would be used for optical flow calculations, suggesting that raycasting is the best approach to extend the current work. A brief discussion of raycasting technique follows.
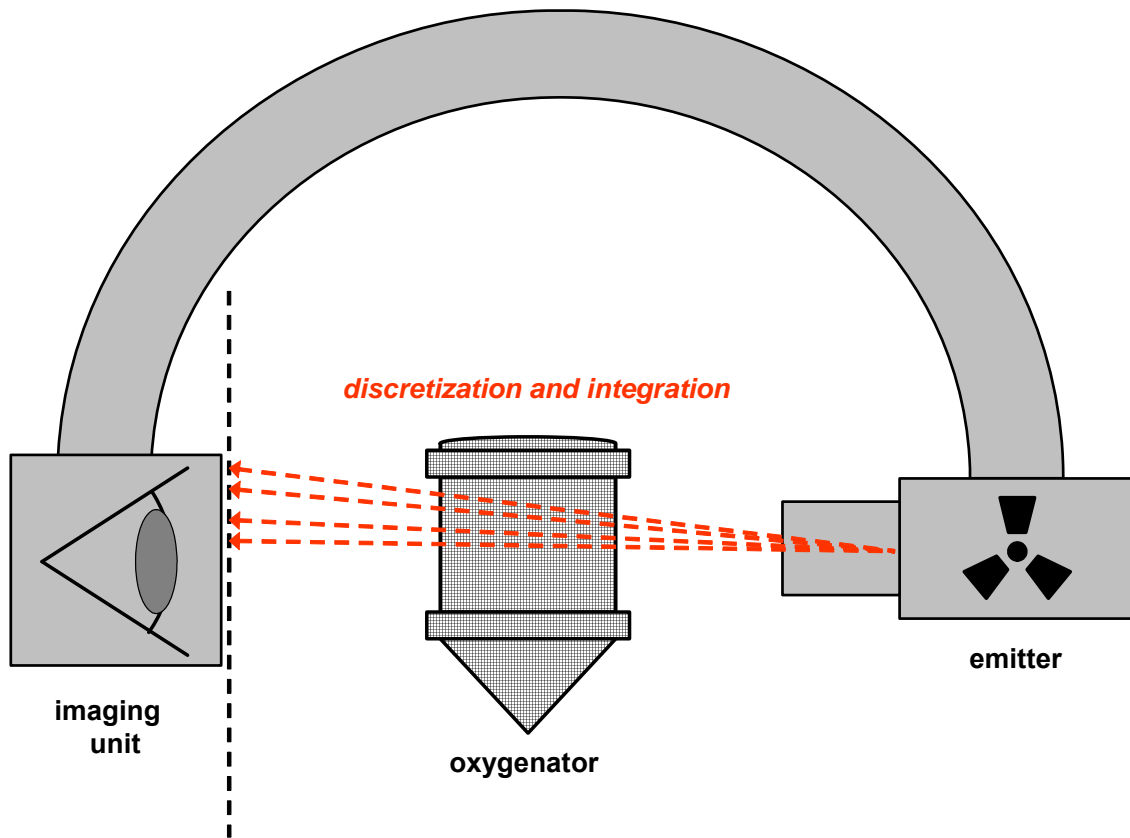
Figure 3-16 Raycasting mirrors the fluoroscopic imaging process.

As mentioned earlier, volume visualization of unstructured data is not a trivial undertaking. One of the earliest and conceptually straightforward raycasting methods for unstructured datasets was proposed by Garrity in 1990 [72]. His basic approach divides the process into two steps: *preprocessing* and *raycasting*. The dataset would initially be converted from point-based to cell-based data (most CFD data are point-based) for the variable of interest (density in the present case) and the cell faces would be sorted into *shared* versus *unshared*. Optionally, the faces can be sorted into a grid for the purpose of accelerating the ray-face intersection search. Once preprocessing is complete, a ray is cast from each pixel in the viewing plane to focal spot of the x-ray emitter; in essence the x-ray beam is being followed from end to beginning. As rays can only enter the object along an unshared face, only these faces must be tested for intersection. Once a particular face has been entered, the ray can only exit through one

of the other faces of the given cell. In this manner, the ray can be tracked through each adjacent cell in succession until the object is exited. The process would be continued until the beam source is reached as it is possible to re-enter the object domain. Attenuation is calculated for each cell visited based on the density of the cell and the ray path length through that cell. The attenuations are summed along the ray to create a final value representing the total beam attenuation through the object of interest. **Figure 3-17** describes the volumetric raycasting procedure in an algorithmic form.

On a final note, a data acquisition technique that provides "clean" velocity field information in 3D would be ideal. Recent publications in the chemical engineering literature have demonstrated the successful use of MRI in mapping the velocity field of fluids passing through fibrous media, which is in contrast to earlier efforts in our own institution. Further development of such techniques is of paramount importance for the development and validation of membrane oxygenator pressure-flow relationships and the performance measures that depend upon them.

Data Preprocessing

•Convert point-based data into cell-based
•Sort faces in *unshared* and *shared*
•Sort faces into coarse 3D regular grid

Raycasting Process

for each *pixel* in image plane

  tot-attenuation = 0

  cast *ray* towards focal spot

      find intersection with 3D grid

      if termination conditions are met (all grids visited, etc.)

        then exit

      else if intersection with unshared *face* in grid location

        •**find** *cell*
        •**calculate** exit *face*
        •**calculate** distance in *cell*
        •**calculate** *cell-attenuation*
        •**sum** *cell-attenuation* & *tot-attenuation*

      if exit face is shared

      else

     else

     pixel = *tot-attenuation*

  end

end

Figure 3-17 Algorithm of volumetric raycasting procedure.

4.0   MODELS OF GAS EXCHANGE IN MEMBRANE DEVICES

4.1   BACKGROUND

Investigators have been attempting to describe, characterize and model the dynamics of gas exchange within artificial lungs since their introduction over 50 years ago. The increasing complexity and sophistication of gas exchange models closely parallels the increased complexity of the devices themselves.

Oxygenator models can be classified in a number of ways. For example, the Advancing Front Theory proposed by Lightfoot [73] is best classified based on the dynamics of the exchange process rather than the device geometry. One straightforward method of classification is to divide the models based on the dominant length scale. **Figure 4-1** provides a graphical overview of the concept of dividing the models based on the length scale and the resulting impact on computational resources.

4.1.1   Micro-scale Models

Micro-scale models are based on a length scale comparable to that of the fiber or other oxygenating surface. As previously indicated, early membrane oxygenator designs were comprised mainly of systems best described as internal flow, such as flow between parallel / flat plates and within round tubes and channels. The simple geometries represented in these devices can be assessed in a straightforward, often analytical manner using the solution principles outlined in classic texts such as *Transport Phenomena* [58] and *Conduction of Heat in Solids* [74]. In the case where flow is perpendicular to the fiber or multiple velocity terms fail to vanish, a numerical or computational solution must be sought. The advent of oxygenators utilizing hollow fibers in a crossflow arrangement necessitated the development of new modeling and analysis

methods as the analytical approach proved intractable due to the resulting geometry and flow path, thus eliminating the validity of many assumptions that were applicable in earlier approaches.
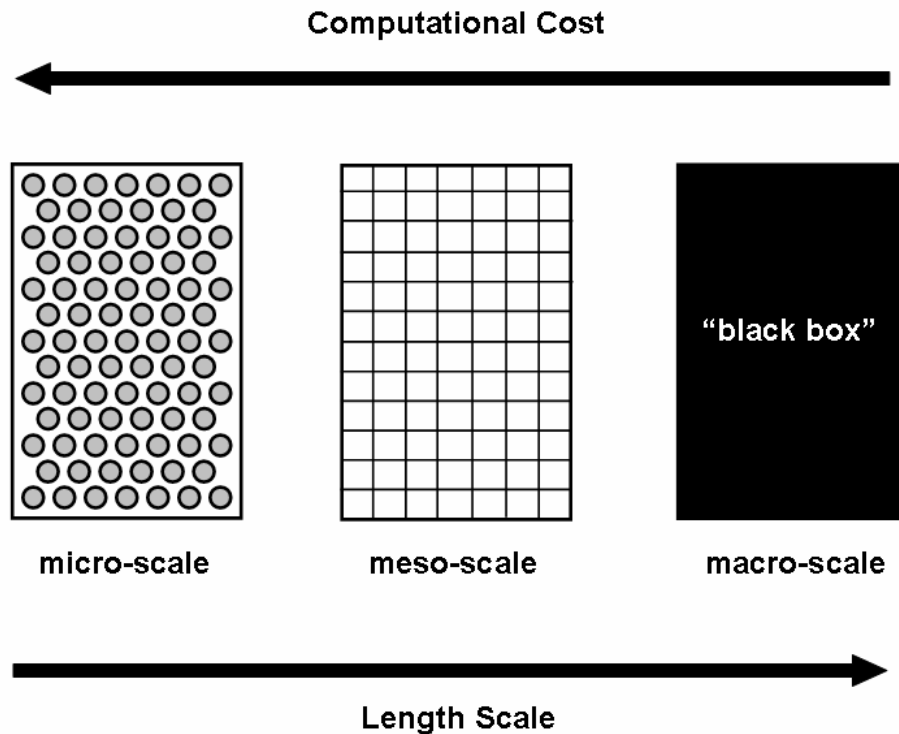
Figure 4-1 Effect of dominant length scale upon computational effort.

The first computational efforts toward understanding gas exchange in oxygenators were presented in 1967 by Weissman and Mockros [75]. This investigation provided critical insight into the phenomena of gas exchange into blood and laid the foundation for the engineering description of the process through the concept of effective diffusivity.

Other computational studies have been performed to model gas exchange from fibers in cross-flow [76, 77] and parallel flow [78]. Cross-flow models have their basis in unit cell models [79] developed to provide a tractable (analytical or computational) subunit of a large-scale

porous media from which an overall "performance" can be calculated. For these models, scale-up of the results remains a significant hurdle, as modeling each individual fiber of an artificial lung lies at the extreme end of the computational spectrum and remains an intractable problem for all but the smallest, simplest geometries. With the computational power available at present, an appropriate compromise would appear to be an approach that allows axisymmetric, two, and three-dimensional geometric modeling but uses approximations to account for the effects of the fibers. This approach has been used for a number of investigations [35, 45, 51].

4.1.2   Macro-scale Models

Macro-scale models are some of the best developed and understood models in use today for approximating device performance. However, these models often resort to a dimensional reduction to simplify the computations – a three dimensional system is modeled with a one-dimensional equation. Although useful, these "black-box" approaches are unable to predict the effect of three-dimensional characteristics on device performance and do not permit full shape based optimization.

The macro-scale models used for analysis of oxygenators have their birth through analogies with correlations from the heat transfer literature [80, 81]. The first widely known use of these models for predicting gas exchange in blood was presented by Mockros and Leonard in 1985 [81], where they attribute the form of their model to Kays and London [82].

Dimensional analysis of the governing equations [58] for mass transfer also leads to the correlations used in macro-scale oxygenator analysis. The final dimensionless groups obtained are dependent upon the form of the governing equations, chosen boundary conditions and investigator opinion, and can therefore differ. Despite the potential for variation, in general these analyses lead to the definition of the Sherwood, Reynolds, and Schmidt numbers in the dimensionless groups [80, 81, 83], with a dimensionless length or "shape factor" as a potential remaining contributor [36]. The Sherwood number is a dimensionless ratio that relates the rate of mass exchange to the diffusivity of the species. The Schmidt number relates the strength of momentum to species diffusivity, and the Reynolds number relates the strength of inertial to viscous forces in the system. Given these results, the most common form of dimensionless mass

transfer correlation is one that relates the Sherwood number to some power of the Reynolds and Schmidt numbers as defined for the system under investigation.

$$Sh = a\,Re^{\alpha}\,Sc^{\beta}$$ **Equation 4-1**

The premultiplication factor *a* and the exponents α and β are determined from experiment through multivariable regression. These experimental coefficients are considered to be dependent upon the structural characteristics of the device [80, 81], although β is often preset to 1/3 due to theoretical [58] and recent experimental support [84]. Some authors will "lump" the Schmidt number (with the preset exponent) in with the Sherwood number to create a combined "dimensionless mass transfer coefficient" that is then correlated with the remaining terms [80, 81]. One advantage of the approach is the use of simple log-log plots of <K> and Re to reveal the functional dependence and the values of *a* and α.

Although it is theoretically possible to create a nomogram or model that will predict the outflow condition given all the inputs, the operating space that must be evaluated experimentally is overwhelming. Some parameters governing the system behavior are clearly dependent upon the device structure, meaning that a simple change in a device feature will limit the utility of the existing data for predicting the performance of the altered device. Investigators have attempted to circumvent the limitations of the basic mass transfer correlation presented in **Equation 4-1** and its device specific coefficients with the additional shape or geometrical parameters that arise from the dimensional studies presented earlier [36, 37]. For example, Dierickx et al [36] introduced two dimensionless parameters ζ (dimensionless manifold length) and ε (dimensionless blood path length) to generate a correlation that is generally applicable to HFM units. There results allowed the collapse of data for multiple oxygenators onto one figure but it is unclear if such an approach results in data accurate enough to be used in computational predictions. His method does demonstrate that the definition of "blood path length" is variable but can have a significant impact on resulting values.

authors	model equation

Dierickx, et al.[†]

$$N_{Sh} N_{Sc}^{-\frac{1}{3}} \cdot \xi^{\frac{1}{2}} = \phi \cdot \left(\varepsilon^{\frac{1}{m}} \cdot N_{Re} \right)^{m}$$

$$N_{Pe} > 3200 \quad \phi = 0.47, m = 0.64$$
$$N_{Pe} < 3200 \quad \phi = 0.26, m = 1.00$$

experimental details

- **Gas-to-liquid flow at 3:1 ratio**
- **Water flow rates between 0.5 to 6.0 Lpm**
- **20.9% O_2 for water and 100% O_2 for blood**
- **Improved geometric characterization using ξ and ε**
- **Used Cobe Optima™ commercial units**

†Dierickx PW, et al. Mass transfer characteristics of artificial lungs. *ASAIO Journal* 2001 47:628-33.

Figure 4-2 Overview of experiments by Dierickx, et al.

Macro-scale models are the best characterized at present and have the largest publication base in the oxygenator literature. Although similar, there are important differences in the experimental approaches, valid range of data, and variable definitions that must be considered when drawing conclusions or comparing results from different groups.

Mockros, Vaslef and Wickramasinghe use mass transfer relationships equivalent to that outlined in **Equation 4-1**. The experimental approach differs between the authors. Mockros and Vaslef investigate oxygen exchange into water or blood while Wickramasinghe uses a deoxygenation technique in his experiments. The advantage of the deoxygenation procedure is that one avoids the high oxygen tensions that fall beyond the linear range of most oxygen analyzers. However, he utilized a low liquid flow rate in his experiments which can result in problems of equilibration that will be discussed later. In addition, there was no mention of the

geometric characterization used in his analysis (i.e., the blood flow path length or frontal area) although it did remain constant. **Figures 4-3** and **4-4** provide an overview of the methods and experiments used by the two groups.

authors	model equation

Wickramasinghe, et al. (1992)[†*]

$$N_{Sh} = \phi \cdot N_{Re}^{m} N_{Sc}^{1/3}$$

$$N_{Re} > 2.5 \quad \phi = 0.15, m = 0.8$$
$$N_{Re} < 2.5 \quad \phi = 0.12, m = 1.0$$

experimental details

- **Pure, water-saturated N$_2$ gas flow of 6 Lpm**
- **O$_2$ saturated water flow of 0.1 to 1.7 Lpm**
- **Deoxygenation experimental procedure**
- **Unspecified (but constant) geometric characterization**
- **Used Medtronic Maxima™ commercial units**

†Wickramasinghe SR, Semmens MJ, Cussler EL. *J Mem Sci* 1992 69:235-250.
*Wickramasinghe SR. *The best hollow fibre module.* PhD Thesis, Univ of Minnesota 1992.

Figure 4-3 Overview of experiments by Wickramasinghe, et al.

authors	model equation

Vaslef, et al.[†*]
Mockros & Leonard[‡]

$$N_{Sh}N_{Sc}^{-1/3} = \phi \cdot N_{Re}{}^{m}$$

$$\frac{dP}{dx} = \frac{4\varphi}{\varepsilon}\left(\frac{1-\varepsilon}{d}\right)^{2-m}\left(\frac{A_f v}{Q_b}\right)^{1-m}\left(\frac{D}{v}\right)^{2/3}\frac{(P_b - P)}{[1 + \lambda(P)]^{2/3}}$$

water[‡]	$\phi = 0.17, m = 0.85$
water[†]	$\phi = 0.124, m = 0.807$
blood[†]	$\phi = 0.243, m = 0.484$
water[*]	$\phi = 0.136, m = 0.832$

experimental details

- **Specific geometric characterization using A_f and L_{path}**
- **Used Sarns SMO1™ and related commercial units**
- **Peclet numbers matched for some experiments[†]**

[‡]**Mockros L.F., Leonard R. *Trans Am Soc Artif Intern Organs* 31:628-633. 1985.**
[†]**Vaslef SN, et al. *ASAIO Journal* 40:990-996. 1994.**
[*]**Vaslef SN. PhD Dissertation. Northwestern Univ, Chicago, IL 1990.**

Figure 4-4 Overview of experiments performed by Mockros, Leonard, and Vaslef et al.

4.1.3   Meso-scale Model

As suggested in the previous sections, the advantages of the macro and micro-scale approaches can be combined, effecting the elimination of most of their disadvantages through the use of what can be termed the meso-scale approach. The current approach to meso-scale modeling utilizes a geometrically representative domain for simulation purposes but does not model the oxygenating surface (usually fibers) directly; the fiber effects (but not the fiber structure) are accounted for with simplified models that assume a regional form of the macro-scale or "black-box" models introduced earlier. In essence, the oxygenator is subdivided into separate areas with

a scale much larger than an individual fiber but much less than the scale of the overall device. Investigators have begun to evaluate the application of the meso-scale approach to modeling HFM devices with considerable success [39, 45, 52]. The meso-scale approach was utilized to predict the mass transfer performance of a commercial HFM oxygenator, the Medtronic Maxima™.

4.2   MATERIALS AND METHODS

4.2.1   Computational Model

The geometric model of the Maxima™ and the subsequent computational grid has been described in previous chapters. The governing equations and boundary conditions for the conservation of momentum remain the same as in previous computational investigations.

As indicated in the overview, a meso-scale approach is used to simulate gas exchange in the device; the fiber structure is not part of the computational model although the effects of the fibers (gas exchange, momentum loss) are included. In a similar fashion to the use of a porous media model to calculate the pressure drop associated with porous media flow, the increase in species concentration associated with mass transfer can be accommodated on a per-cell basis through the use of a source term in the species transport equation, which considers convection, diffusion and generation. Full details regarding the assumptions and formal derivation of **Equation 4-2** can be found in **Appendix B.**

$$\vec{u} \cdot \nabla P_{O2} = D_{eff} \, \nabla^2 P_{O2} + R_{eff} \qquad \qquad \textbf{Equation 4-2}$$

Two terms in the **Equation 4-2** deserve special mention. The effective diffusivity term is closely allied to the variable diffusivity proposed by Weissman and Mockros [75] but has been derived for the case of transport within a porous media and therefore includes the porosity ε.

$$D_{eff} = \frac{\varepsilon \alpha}{(\alpha + C_T \lambda)} D \qquad \qquad \textbf{Equation 4-3}$$

The effective species reaction or generation term, R_{eff}, accounts for the effects of device porosity and oxyhemoglobin dissociation curve upon the local species generation rate R.

$$R_{eff} = \frac{\varepsilon}{(\alpha + C_T \lambda)} R$$

<div align="right">**Equation 4-4**</div>

Determination of the local species generation rate R utilizes the local species concentration, surface area, and porosity, along with a mass transfer coefficient, which is a lumped parameter that accounts for intrinsic fluid and device properties that affect the rate of mass exchange. The approach has been used with some success for modeling gas exchange to blood in membrane oxygenators [80]. **Appendix C** contains the relevant details regarding the definition of the local species generation rate within a porous media.

$$R = \frac{4(1-\varepsilon)}{\varepsilon d} K \alpha \Delta P_{O2}$$

<div align="right">**Equation 4-5**</div>

Equation 4-5 includes an important unknown in the form of the mass transfer coefficient K, which is not constant for blood and requires experimental determination. Correlations for determining the mass transfer coefficient of membrane devices exist and can be found in both the chemical engineering and artificial organs literature. These correlations are often of the form

$$Sh = aRe^{\alpha} Sc^{\beta}$$

<div align="right">**Equation 4-6**</div>

Using definitions found in the literature [81], **Equation 4-6** can be used to determine the form of the mass transfer coefficient K as detailed in **Appendix C.**

$$K = av^{\alpha} d_h^{\alpha-1} D^{\frac{2}{3}} v^{\frac{1}{3}-\alpha} \left(1 + \frac{C_T}{\alpha} \lambda\right)^{\frac{1}{3}}$$

<div align="right">**Equation 4-7**</div>

Species transport (i.e., oxygen transport in blood) can be simulated using a variety of approaches. One can consider blood as a mixture where both the fluid and dissolved gas contribute to the physical properties on a per volume basis. In this approach, a dissolved gas could affect the overall viscosity and density of the fluid, although in actual simulations the change was negligible. An alternative approach was to assume the blood and gas are separate species. The gas would be modeled using a species transport equation with the velocity information coming from the solved blood conservation of momentum equations. The former approach was used for initial simulations as it was the only modeling technique supported by our software (FLUENT5) at that time. As the software was updated to support scalar transport

models, the latter approach was utilized as it more accurately represented the physical conditions with the oxygenator.

Appropriate parameters for **Equation 4-6** that were experimentally derived for the Medtronic Maxima™ have been reported in the literature [85] and were employed here. These values were derived by Wickramasinghe for water (a non-reactive fluid) using methods similar to those proposed by Mockros and Vaslef [80, 81, 83]. In his experiments, Wickramasinghe deoxygenated water passing through the oxygenator using nitrogen stripping. A review of his data shows that nearly all oxygen was removed from the fluid stream at all flow rates, which were well below those used in clinical practice. Because blood has a viscosity approximately three times that of water, but only a slightly higher density, dimensional analysis would suggest that one should flow water at a higher rate than that used in clinical practice to provide data useful for calculation with blood. By flowing at a lower rate, the water equilibrates with the surrounding gas carrying fibers before exiting the device. This equilibration causes an under-prediction of the gas exchange performance. **Figure 4-5** demonstrates this in a graphical format.

Evidence for flow-limited O₂ transfer

$$k = v^0 \frac{a}{Z} \ln\left[\frac{c_1(sat) - c_1(inlet)}{c_1(sat) - c_1(outlet)}\right]$$ **Assume at L*,** $c_1^* \approx c_1(outlet)$

$L \approx 2L^*$
$\therefore k_{true} \approx 2\,k_{apparent}$

$L \approx 1.3\overline{3}L^*$
$\therefore k_{true} \approx 1.3\overline{3}\,k_{apparent}$

$L \approx L^*$
$\therefore k_{true} \approx k_{apparent}$

L ↕

L*

L*

L*
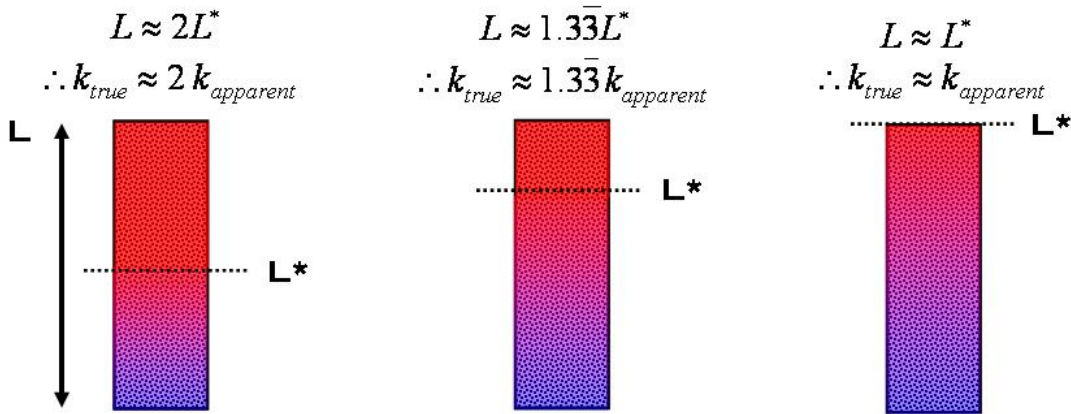
Figure 4-5 Effect of equilibrium on calculated mass transfer coefficients.

Path length is a critical parameter for calculating overall gas exchange efficiency. By approaching equilibrium, the actual length over which gas exchange occurs is less than that used for calculation of the overall efficiency. The effect of this change on the calculation of the critical parameters alpha and beta is shown in **Figure 4-6.** The overall effect is one of increasing the pre-multiplication factor while decreasing the slope of the relationship between Re and <K>, the dimensionless mass transfer rate. These results explain why previous attempts to use water data to predict blood transfer rates in HFM have not resulted in accurate prediction of the gas concentration at device outflow. Close review of the discrepancies between blood and water parameters obtained in the experiments of Vaslef, presented in his dissertation [83], show just such behavior. This does not mean the approach outlined by Mockros and Vaslef is without utility; from a theoretical standpoint there is little argument against the approach. However, the

data collected using water must be collected in a flow range that matches the dimensionless conditions shared with blood. Because of their large size and surface area, the flow range required for commercial devices falls in the range of 10-20 L/min, which is beyond that reported in the literature to date.

Figure 4-6 Effect of equilibrium upon mass transfer relationship parameters.

An experimental approach that could address the concern of appropriate flow rates for the determination of mass transfer parameters would use specially designed oxygenators with uniform flow paths and limited gas exchange area. A reduction in overall device size would reduce the volumetric flow requirements to a level easily reached with current experimental equipment even when water is used as the exchange fluid. By using flow path geometries that provide uniform flow characteristics, one could assume that differences in transport properties

(Newtonian versus non-Newtonian flow behavior) would have a minimal effect on the fluid distribution and the resulting gas exchange.

Further evidence supporting these conclusions is present in the literature. For example, Dierickx et al [36] presents evidence that there are two particular exchange regimes present in an oxygenator which are dependent on the Peclet number. In one regime, defined by low flow, the gas exchange is linearly related to the flow rate; in the other, high flow regime, the gas exchange rate falls short of being linearly related to flow. Theoretical [86] and experimental [87] analysis of the effects of boundary layers on heat exchange rates suggests that mass exchange cannot be a linear relationship with flow; Such perfect exchange can only appear to occur if equilibrium (or near equilibrium) has been achieved within the device. The appearance of a change in slope (and an apparent flow regime change) also occurs in **Figure 4-6**. And can be explained by the fact that the equilibrium point is now beyond the exit of the oxygenator; the true relationship between gas exchange and flow rate becomes evident as a change in slope between the dimensionless mass transfer and Reynolds number. Both Dierickx [36] and Vaslef [80] attempted to improve the relationship of their data through matching of the Peclet Number and reduction of the oxygen concentration in the gas. Although reduction in gas concentration reduces the driving force for gas exchange, it also reduces the point at which equilibrium would occur; which effect dominates is unknown.

4.2.2   Experimental Data

Experimental data for oxygen exchange to blood in the Medtronic Maxima™ was obtained from the device manufacturer. The data consisted of averaged values of blood saturation and dissolved oxygen concentration in the form of partial pressures at the device inlet and outlet. The data was obtained under AAMI standard conditions [42] at 2, 4, 6, and 7 liter / min flow rates. The experimental outflow conditions were compared to the CFD predicted values, as were the overall rates of gas exchange.

4.3   RESULTS

The experimental and CFD predicted rates of volumetric oxygen exchange in mL per min as a function of flow rate are shown in **Figure 4-7**. This form of data presentation is preferred in the clinical literature as it indicates the amount of oxygen that can be transferred per minute to meet the patient's basic metabolic demand.
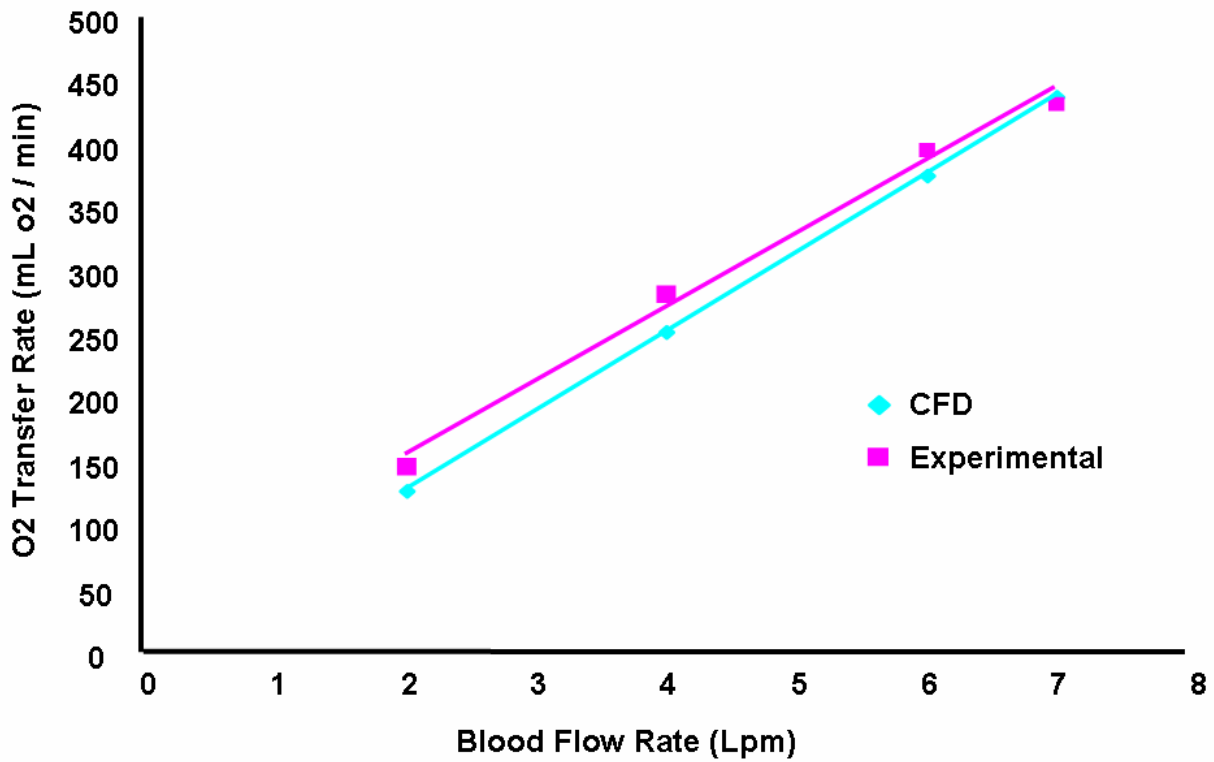
Figure 4-7 Experimental and CFD predicted overall mass transfer rate for the Maxima™.
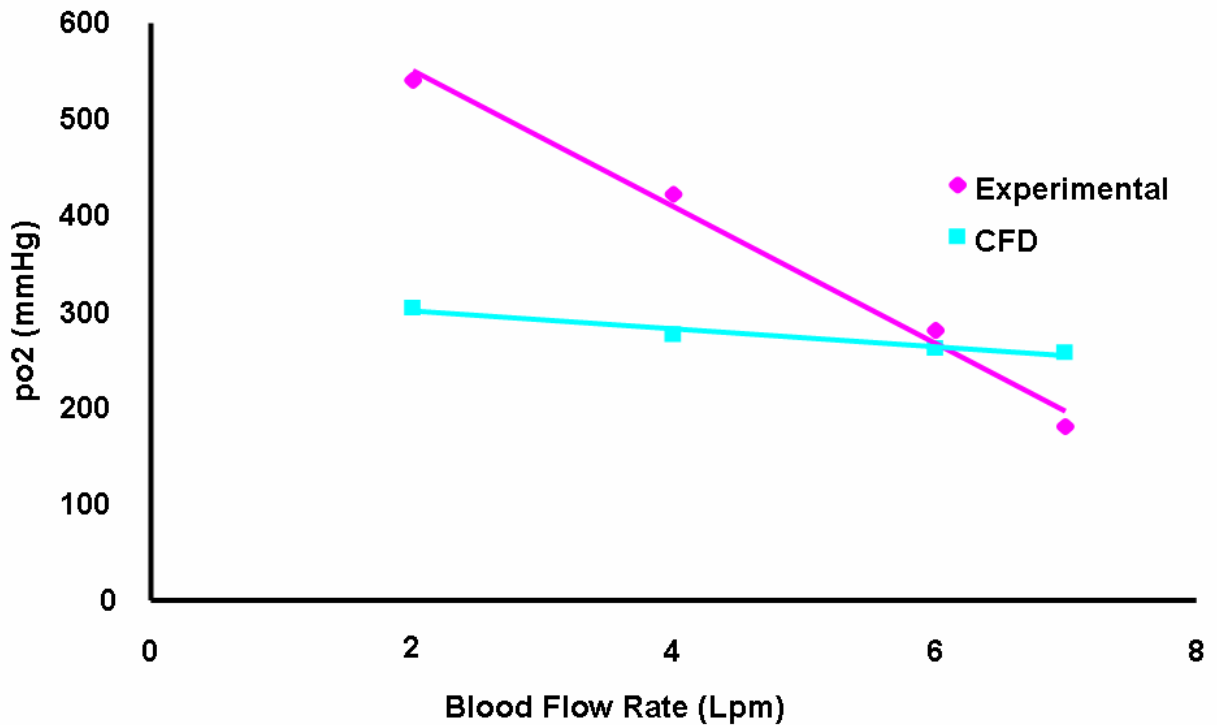
Figure 4-8 Experimental and CFD predicted outflow dissolved oxygen content.

Figure 4-8 is showing the outlet oxygen concentrations from the experimental and computational studies. It is obvious that a substantial difference exists at most flow rates, with the close agreement at 6 LPM due to the overall trend of the data series rather than an improved predictive result.

4.4   DISCUSSION AND ANALYSIS OF LITERATURE DATA

One must investigate the assumptions, data and findings of the numerical and computational models that form the engineering backbone of the meso-scale approach in an effort to resolve the

apparent discrepancy between the experimental and CFD predicted oxygen concentrations at the device outflow.

One possible cause of the discrepancy could be an error in the correlative model used to determine the length averaged mass transfer coefficient. To investigate if this could be the source of the error, the data presented in the original paper of Mockros and Leonard [81] was analyzed using the methodology described in [83]. In his thesis, Dr. Vaslef demonstrates that the normalized, length-averaged dimensionless mass transfer coefficient <K> should remain the same under the same flow conditions for an oxygenator regardless of the inlet blood conditions. Fortunately, Mockros and Leonard present such data in their 1985 paper [81].

An open-source data digitizing software package (Engauge Digitizer v2.12, http://digitizer.sourceforge.net/) was used obtain the inlet and outlet blood saturation data from the original figures presented in [81]. The data were then processed to determine the normalized, length-average dimensionless mass transfer coefficient <K> at each experimental condition. The results are shown below and indicate that the dimensionless value of <K> is indeed constant to some approximation. It is believed the deviations that appear at the higher inlet blood saturations arise due to the impact of even slight experimental errors in saturation upon the calculate of the corresponding oxygen partial pressure. There are two sources of error that can arise in the calculated values. One source of error arises from the acquisition of data from the figure, where pixel selection could affect the final value to some extent. Of larger concern is the effect of the oxyhemoglobin-dissociation curve at large saturations. At the high saturations present at the device outflow, a very small change in saturation can result in a large change in raw pO2 value. At these very shallow slopes, experimental error inherent in the equipment itself can have a large effect upon the final pO2 value. Based on these results, the concept of the normalized, length-averaged mass transfer coefficient and its role in the Sherwood-Reynolds-Schmidt correlation is sound.
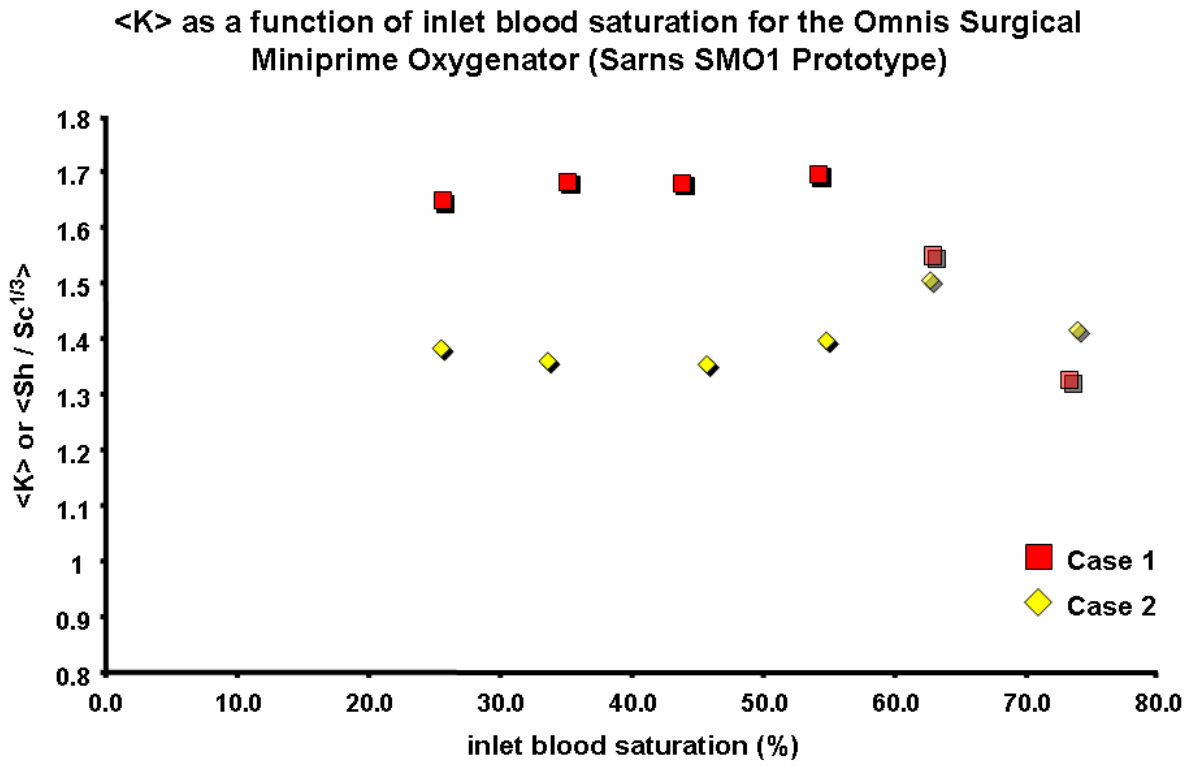
Figure 4-9 Normalized, length-averaged mass transfer coefficients using data from [81].

Another possible source of error in the use of correlative models is the reliance upon fluids other than blood to calculate the magnitude of the premultiplication and exponential factors. The use of nondimensional correlative mass transfer equations should permit one to use any fluid, under the proper operating conditions, to collect the appropriate data for regression of the parameters describing the mass transfer behavior. Because of this, researchers [36, 80, 85] have utilized non-reactive fluids such as water in the evaluation of the mass transfer parameters. However, **Figure 4-10** reveals a significant discrepancy in the prediction of outlet oxygen concentrations using parameters derived from different motive fluids. Dr. Vaslef reported on the difference in the mass transfer parameters when water and blood are used [83], and the results shown in **Figure 4-10** using his data and iterative methods demonstrate a clear deviation. These

findings indicate that improper experimental conditions or assumptions could lead to incorrect mass transfer parameters and ultimately poor prediction of gas exchange.
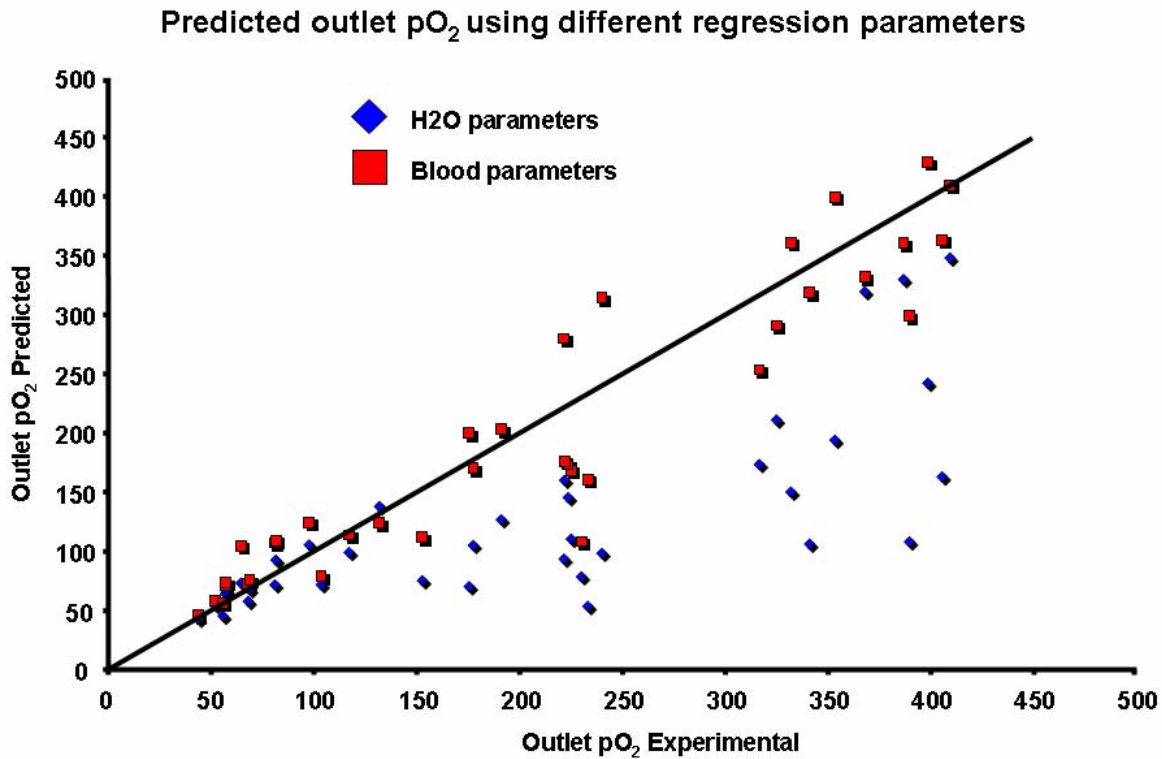
Figure 4-10 Outflow oxygen concentrations using parameters and data from [83].

4.5   FUTURE WORK

The accurate prediction of spatial oxygen species concentration in blood is particularly challenging. Computational studies often report the overall rate of oxygen transfer, but neglect to show concordance between the partial pressure of oxygen predicted computationally with that measured through experiment. For clinicians, the overall rate of oxygen transfer to blood is the variable of interest, but for design optimization, the spatial oxygen concentration provides a

concrete measure of the contribution of a particular device region to overall gas transfer. Efficiency measures such as mass transfer coefficients can also provide insight for device optimization [45] but are not as rigorous as dissolved gas concentration. Recent authors have reported impressive results in oxygenator design optimization with an approach that utilized automatic meshing, computational fluid dynamics and genetic algorithms [39]. More than 900 designs were analyzed during the investigation, which only took eight days to complete. Of note, the authors did not utilize a gas exchange rate as an objective parameter in their investigation, presumably because of the lack of a suitable gas exchange model.

The development of an accurate spatial model of gas exchange could require the stepwise solution of a number of extant problems in meso-scale simulation. These include determining the proper form of the porous media model used to approximate the momentum losses in the fiber bundle, validation of the meso-scale flow pattern predicted by the model through an imaging process, and eventual incorporation of the validated models into a research program for the determination of the proper mass transfer relationship. However, it might be possible to avoid a stepwise solution process in favor of a new experimental approach that provides a spatially variant yet known velocity field, allowing the investigator to focus on the form of the mass transfer model and its validation. On possible experimental apparatus with these features is shown below.

A radial flow chamber with a circularly wrapped, vertically oriented fiber bundle would permit one to experimentally separate the problems of pressure-flow prediction and mass transfer. Assuming a well-wrapped bundle with radially uniform permeabilities, all fluid passing through the bundle will be moving at the same speed at a particular radial location, possess the same oxygenation history, and should be experiencing the same amount of mass transfer. One can vary the total surface area available for mass transfer, utilize different fluids and experiment with different models without the requirement of determining the flow field in a complex oxygenator geometry. Although these characteristics have been assumed in the development of useful mathematical models [88], an experimental device that possess these features would eliminate the need for these assumptions in model development.
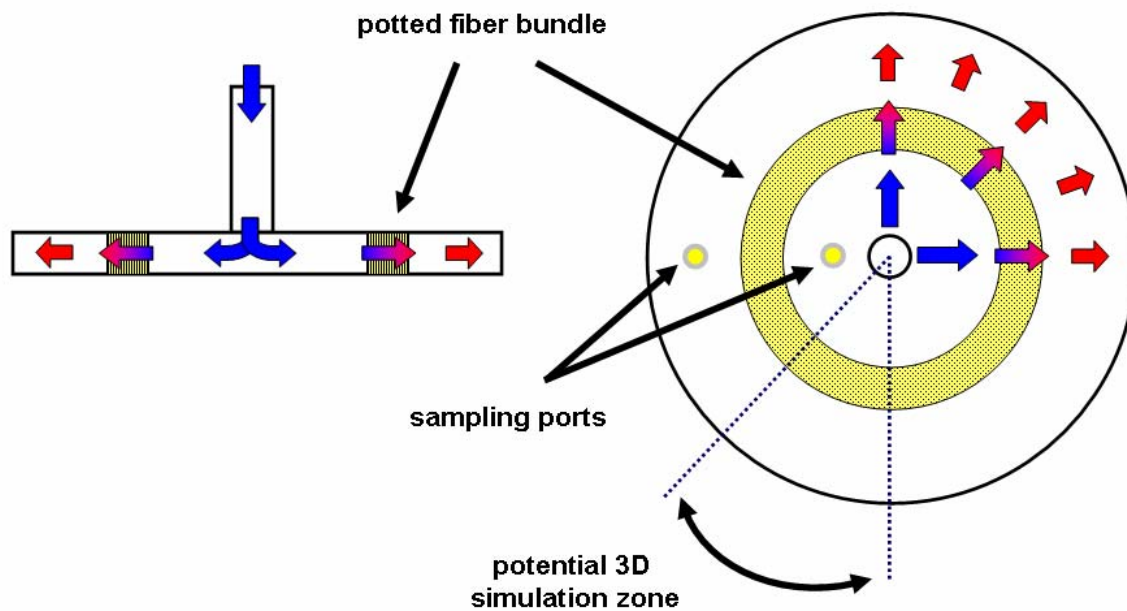
Figure 4-11 The proposed radial flow fiber bundle is shown.

Although ideal, a radial flow fiber bundle is not an absolute requirement to predict gas exchange for an individual oxygenator. One could take the coefficients calculated from the high flow regime and extrapolate to the low flow region, which assumes there is no difference in the actual flow phenomena present between the two regimes, i.e., one is laminar and the other turbulent. For the low range of Reynolds numbers under which oxygenators are operated in the clinical setting, this assumption seems reasonable and would be an appropriate starting point for future work.

5.0   CONCLUSIONS

"If I have a thousand ideas, and only one turns out to be good, I am satisfied."
   - Alfred Bernhard Nobel

The conclusions resulting from the proposed work and final dissertation are as follows:

Fluids flowing at clinical speeds within hollow fiber membrane oxygenators experience pressure losses exceeding those predicted by purely viscous losses alone. In addition, the pressure loss trend possesses a non-linear character often attributed to the inertial losses encountered in high-speed turbulent flow. These results suggest that additional phenomena are affecting the pressure losses and that a purely viscous model is unsatisfactory.

Visualization of flow patterns in membrane oxygenators and validation of CFD predicted patterns are both important tasks in artificial lung research. Despite its limitations, fluoroscopic imaging is a useful tool for investigating pressure-flow phenomena in hollow fiber membrane devices.

Despite the considerable potential of spatial modeling of gas exchange in hollow fiber devices, current models and approaches appear limited in their ability to provide accurate results. The construction of idealized flow geometries would allow faster and more flexible evaluation of operating conditions and potential model improvements.

APPENDIX A

FLOW VISUALIZATION MATLAB M-FILES

A.1 OPTICAL FLOW M-FILES

The following m-files are used to calculate the optical flow present in an image sequence. The methods implemented for dissertation work include the method of Horn & Schunk [67] and Cornelius & Kanade [89].

A.1.1 optical_flow_Horn_1981.m

```
function vel_field = optical_flow_Horn_1981(E_series, vel_guess, bc, iter)
%
%
%


% Use weighting factor estimate
alpha_sq = 0.00024;
%alpha_sq = 1;


% Determine the size of the image sequence
[rows,cols,ts] = size(E_series);


% Create brightness partial derivative matrices
```

```
E_x = zeros(rows-1,cols-1);

E_y = zeros(rows-1,cols-1);

E_t = zeros(rows-1,cols-1);


% Note: The procedure for estimating the partial derivatives uses the formula

% from reference 1. The terms are collected in stages using the commutative

% and distributive properties of addition and subtraction to perform the

% operations in vector form.  The signs variable indicates whether the

% terms are added or subtracted for the partial derivative being calculated.

signs = ones(3) + diag([-2,-2,-2],0);


% Estimate the brightness partial derivatives using formula from ref 1

E_deriv = zeros(rows,cols,2);


% Iterate through the image sequence

for timestep = 1:ts-1


    for dim = 1:3


        % Collapse rows through addition or subtraction with row above

        for i = 1:rows-1

            E_deriv(i,:,:) = E_series(i+1,:,timestep:timestep+1) + ...

                signs(dim,1)*E_series(i,:,timestep:timestep+1);

        end


        % Using the new values collapse the columns

        for j = 1:cols-1

            E_deriv(:,j,:) = E_deriv(:,j+1,:) + signs(dim,2)*E_deriv(:,j,:);

        end


        % Flatten the result through addition or subtraction

        for k = 1

            E_deriv(:,:,k) = E_deriv(:,:,k+1) + signs(dim,3)*E_deriv(:,:,k);
```

76

```matlab
    end


    % Assign results to brightness partial derivative matrices

    if dim == 1

        E_y = 0.25*E_deriv(1:rows-1,1:cols-1,1);

    elseif dim == 2

        E_x = 0.25*E_deriv(1:rows-1,1:cols-1,1);

    else

        E_t = 0.25*E_deriv(1:rows-1,1:cols-1,1);

    end


end


E_dim = zeros(rows-1,cols-1,3);

E_dim(:,:,1) = E_x;

E_dim(:,:,2) = E_y;

E_dim(:,:,3) = E_t;


% Determine if initial vel matrix provided and instantiate if absent

if (isempty(vel_guess))

    vel_guess = zeros(rows-1,cols-1,2);


elseif (size(vel_guess) ~= [rows-1, cols-1, 2])

    error('ERROR: Velocity matrix possesses improper dimensions');

end


% Instantiate average vel matrices and weighting matrix

vel_avg = ones(rows-1,cols-1,3);

weights = zeros(rows-1,cols-1);


% Create averaging filter for Laplacian calculation

avg_filter = [1/12,1/6,1/12; 1/6,0,1/6; 1/12,1/6,1/12];
```

```matlab
% Calculate optical flow using Gauss-Jacobi iterations
for k = 1:iter


    % Prepare matrices based on boundary conditions desired
    if strcmpi(bc,'normal') % zero normal b.c.


        % Assign convolution operator flag
        conv_flag = 'valid';


        % Add row and column to all sides of flow field matrix
        vel_proc = zeros(rows+1,cols+1,2);


        % Place input field in center of new matrix
        vel_proc(2:rows,2:cols,:) = vel_guess;


        % Duplicate outer rows and columns
        vel_proc(1,2:cols,:) = vel_guess(1,:,:);
        vel_proc(rows+1,2:cols,:) = vel_guess(rows-1,:,:);
        vel_proc(2:rows,1,:) = vel_guess(:,1,:);
        vel_proc(2:rows,cols+1,:) = vel_guess(:,cols-1,:);


        % Populate corners of new matrix
        vel_proc(1,1,:) = vel_guess(1,1,:);
        vel_proc(1,cols+1,:) = vel_guess(1,cols-1,:);
        vel_proc(rows+1,1,:) = vel_guess(rows-1,1,:);
        vel_proc(rows+1,cols+1,:) = vel_guess(rows-1,cols-1,:);

    elseif strcmpi(bc,'zeros')  % zero padded b.c.


        % Direct transfer into processing matrix
        vel_proc = vel_guess;


        % Assign convolution operator flag
```

```matlab
            conv_flag = 'same';


        else

            error('ERROR: Unknown boundary condition: see usage');

        end


        % Perform FFT based convolution to generate average vel estimate

        vel_avg(:,:,1) = conv2(vel_proc(:,:,1),avg_filter,conv_flag);

        vel_avg(:,:,2) = conv2(vel_proc(:,:,2),avg_filter,conv_flag);


        % Calculate weighting terms

        for i = 1:rows-1

            for j = 1:cols-1


                % Calculate weighting term with noise based smoothing param

                weights(i,j) = dot(E_dim(i,j,:),vel_avg(i,j,:)) / ...

                    (sum(E_dim(i,j,1:2).^2) + alpha_sq);


            end

        end


        % Update vel estimate

        vel_guess(:,:,1) = vel_avg(:,:,1) - (squeeze(E_dim(:,:,1)) .* weights);

        vel_guess(:,:,2) = vel_avg(:,:,2) - (squeeze(E_dim(:,:,2)) .* weights);


    end % End iterations per timestep

end % End timestep iterations


vel_field = vel_guess;
```

A.1.2 optical_flow_Cornelius_1983.m

```
function [vel_field,dEdt_total] = optical_flow_Cornelius_1983(E_series, vel_guess, dEdt_guess,
bc, iter)
%
%
%


% Determine if smoothness parameter for image vel provided

alpha_sq = 0.1;


% Determine if smoothness parameter for brightness variation provided

beta_sq = 0.1;


% Determine the size of the image sequence

[rows,cols,ts] = size(E_series);


% Create brightness partial derivative matrices

E_x = zeros(rows-1,cols-1);

E_y = zeros(rows-1,cols-1);

E_t = zeros(rows-1,cols-1);



% Note: The procedure for estimating the partial derivatives uses the formula

% from reference 1. The terms are collected in stages using the commutative

% and distributive properties of addition and subtraction to perform the

% operations in vector form.  The signs variable indicates whether the

% terms are added or subtracted for the partial derivative being calculated.

signs = ones(3) + diag([-2,-2,-2],0);


% Estimate the brightness partial derivatives using formula from ref 1

E_deriv = zeros(rows,cols,2);
```

```matlab
% Iterate through the image sequence

for timestep = 1:ts-1


    for dim = 1:3


        % Collapse rows through addition or subtraction

        for i = 1:rows-1

            E_deriv(i,:,:) = E_series(i+1,:,timestep:timestep+1) + ...

                signs(dim,1)*E_series(i,:,timestep:timestep+1);

        end


        % Using the new values collapse the columns

        for j = 1:cols-1

            E_deriv(:,j,:) = E_deriv(:,j+1,:) + signs(dim,2)*E_deriv(:,j,:);

        end


        % Flatten the result through addition or subtraction

        for k = 1

            E_deriv(:,:,k) = E_deriv(:,:,k+1) + signs(dim,3)*E_deriv(:,:,k);

        end


        % Assign results to brightness partial derivative matrices

        if dim == 1

            E_y = 0.25*E_deriv(1:rows-1,1:cols-1,1);

        elseif dim == 2

            E_x = 0.25*E_deriv(1:rows-1,1:cols-1,1);

        else

            E_t = 0.25*E_deriv(1:rows-1,1:cols-1,1);

        end


    end


    E_dim = zeros(rows-1,cols-1,3);
```

```
E_dim(:,:,1) = E_x;

E_dim(:,:,2) = E_y;

E_dim(:,:,3) = E_t;



% Determine if initial vel matrix provided and instantiate if absent

if (isempty(vel_guess))

    vel_guess = zeros(rows-1,cols-1,2);



elseif (size(vel_guess) ~= [rows-1, cols-1, 2])

    error('ERROR: Velocity matrix possesses improper dimensions');

end



% Instantiate average vel & dEdt matrices and weighting matrix

vel_avg = ones(rows-1,cols-1,3);

dEdt_avg = zeros(rows-1,cols-1);

weights = zeros(rows-1,cols-1);



% Create averaging filter for Laplacian calculation

avg_filter = [1/12,1/6,1/12; 1/6,0,1/6; 1/12,1/6,1/12];



% Calculate optical flow using Gauss-Jacobi iterations

for k = 1:iter



    % Prepare matrices based on boundary conditions desired

    if strcmpi(bc,'normal') % zero normal b.c.



        % Assign convolution operator flag

        conv_flag = 'valid';



        % Add row and column to all sides of flow field & dEdt matrix

        vel_proc = zeros(rows+1,cols+1,2);

        dEdt_proc = zeros(rows+1,cols+1);
```

```
% Place input field in center of new matrix

vel_proc(2:rows,2:cols,:) = vel_guess;

dEdt_proc(2:rows,2:cols) = dEdt_guess;


% Duplicate outer rows and columns

vel_proc(1,2:cols,:) = vel_guess(1,:,:);

vel_proc(rows+1,2:cols,:) = vel_guess(rows-1,:,:);

vel_proc(2:rows,1,:) = vel_guess(:,1,:);

vel_proc(2:rows,cols+1,:) = vel_guess(:,cols-1,:);


dEdt_proc(1,2:cols) = dEdt_guess(1,:);

dEdt_proc(rows+1,2:cols) = dEdt_guess(rows-1,:);

dEdt_proc(2:rows,1) = dEdt_guess(:,1);

dEdt_proc(2:rows,cols+1) = dEdt_guess(:,cols-1);


% Populate corners of new matrix

vel_proc(1,1,:) = vel_guess(1,1,:);

vel_proc(1,cols+1,:) = vel_guess(1,cols-1,:);

vel_proc(rows+1,1,:) = vel_guess(rows-1,1,:);

vel_proc(rows+1,cols+1,:) = vel_guess(rows-1,cols-1,:);


dEdt_proc(1,1) = dEdt_guess(1,1);

dEdt_proc(1,cols+1) = dEdt_guess(1,cols-1);

dEdt_proc(rows+1,1) = dEdt_guess(rows-1,1);

dEdt_proc(rows+1,cols+1) = dEdt_guess(rows-1,cols-1);


elseif strcmpi(bc,'zeros')  % zero padded b.c.


% Direct transfer into processing matrix

vel_proc = vel_guess;


% Assign convolution operator flag

conv_flag = 'same';
```

```
        else

            error('ERROR: Unknown boundary condition: see usage');

        end


        % Perform FFT based convolution to generate average vel & dEdt estimates

        vel_avg(:,:,1) = conv2(vel_proc(:,:,1),avg_filter,conv_flag);

        vel_avg(:,:,2) = conv2(vel_proc(:,:,2),avg_filter,conv_flag);

        dEdt_avg = conv2(dEdt_proc,avg_filter,conv_flag);


        % Calculate weighting terms

        for i = 1:rows-1

            for j = 1:cols-1


                % Calculate weighting term with noise based smoothing param

                weights(i,j) = (dot(E_dim(i,j,:),vel_avg(i,j,:)) - dEdt_avg(i,j,:)) / ...

                    (sum(E_dim(i,j,1:2).^2)*alpha_sq*beta_sq + alpha_sq +
2*beta_sq*(alpha_sq^2));


            end

        end


        % Update vel & dEdt estimates

        vel_guess(:,:,1) = vel_avg(:,:,1) - beta_sq*(squeeze(E_dim(:,:,1)) .* weights);

        vel_guess(:,:,2) = vel_avg(:,:,2) - beta_sq*(squeeze(E_dim(:,:,2)) .* weights);

        dEdt_guess = dEdt_avg + weights;


    end % End iterations per timestep

end % End timestep iterations


vel_field = vel_guess;

dEdt_total = dEdt_guess;
```

A.2   TEST PATTERN MATLAB M-FILES

The current appendix section includes the m-files used to generate test patterns in accordance with those used in the literature for testing optical flow algorithms.

A.2.1 test_pattern_simple.m

The following m-file generates simple patterns (brightness gradients and orthogonal sinusoids) that can be translated, rotated or magnified for testing of optical flow algorithms.

```
function test_image_stack = test_pattern_simple(pattern, transformation, num_images, N, varargin)

% usage:    test_image_stack = test_pattern_simple(pattern, transformation, num_images, size,
% varargin)

% params:   pattern is a string (sinusoid or gradient)

%           transformation is a string (trans, mag, or rot)

%           num_images is the number of images in the final sequence

%           N is the size of the resulting images in pixels (N x N) - assumed square

%           varargin is one or two floating point parameters that determine the magnitude of

%           the resulting transform:

%           2 for translation (row and col offsets - row first)

%           1 for dilation (scale factor) and rotation (angular speed in degrees per timestep)

%

% author:   KLG 03-29-04

% version:  1.1

% M-file for generating test patterns undergoing simple transformations such as

% translation, rotation and dilation. The pattern is generated from orthogonal

% sinusoids in a manner represented in the classic paper of Horn and Schunck[1].

%

% References:

% 1. Horn BKP, Schunck B. Determining Optical Flow. Artif Intelligence

%       17():185-203. 1981.

%
```

```
% Potential Improvements:

% Algorithm implemented using matrix mathematics. Speed increase possible with FFT.

%

% ChangeLog

% KLG 04-03-04

% Added 'gradient' as a function choice for generating test patterns

% Added default settings from reference 1


% Initialize flags for default settings

dirflag = 0; roffflag = 0; coffflag = 0; magflag = 0; rotflag = 0;


% Default settings from reference 1 test sequences

row_offset = 1.5;

col_offset = 0.5;

scale = 0.95;

angle = 2.8;    % degrees per timestep


% Determine function to be used and access parameters

if (strcmpi(pattern,'gradient') | strcmpi(pattern,'sinusoid'))


    % Access orientation of pattern gradient

    if strcmpi(pattern,'gradient')


        for i = 1:length(varargin)

            if strcmpi(varargin{i},'direction')

                direction = varargin{i+1};

                dirflag = 1;

            end

        end


        % Assign default direction of 0 degrees if dirflag unset

        if dirflag == 0

            direction = 0;
```

```matlab
        end


    end

else

    error('ERROR: Unidentified function: see usage');

end




% Determine transformation to be performed and access parameters

if strcmpi(transformation,'trans')


    % Access offset parameters

    for i = 1:length(varargin)

        if strcmpi(varargin{i},'row_offset')

            row_offset = varargin{i+1};

            roffflag = 1;


        elseif strcmpi(varargin{i},'col_offset')

            col_offset = varargin{i+1};

            coffflag = 1;

        end

    end


    % Report if offsets not provided

    if (roffflag == 0 & coffflag == 0)

        disp('NOTE: Row and column offsets undefined. Defaults being used.');

    end


    % Report simple transformation to be performed

    disp(['Pattern undergoing translation with a row offset of ',num2str(row_offset),...

        ' and a column offset of ',num2str(col_offset),' ...']);


elseif strcmpi(transformation,'mag')
```

87

```matlab
    % Access scaling parameter

    for i = 1:length(varargin)

        if strcmpi(varargin{i},'scale')

            scale = varargin{i+1};

            magflag = 1;

        end

    end


    % Report if offsets not provided

    if (magflag == 0)

        disp('NOTE: Scaling parameter undefined. Default being used.');

    end


    % Report simple transformation to be performed

    disp(['Pattern undergoing dilation with a scaling factor of ',num2str(scale),' ...']);



elseif strcmpi(transformation,'rot')


    % Access rotational speed in degrees per timestep

    for i = 1:length(varargin)

        if strcmpi(varargin{i},'angle')

            angle = varargin{i+1};

            rotflag = 1;

        end

    end


    % Report if offsets not provided

    if (rotflag == 0)

        disp('NOTE: Rotational speed undefined. Default being used.');

    end
```

```matlab
    % Report simple transformation to be performed
    disp(['Pattern undergoing rotation with a speed of ',num2str(angle), ...
        ' degrees per timestep']);


else

    error(['Unidentified transformation: ',transformation]);
end


% Generate position matrix for multiplication
% - assumes square matrix
rows = N; cols = N;
initial_pos = ones(rows,cols,3);


for i = 1:rows

    initial_pos(i,:,1) = linspace(1,rows,rows);
end


initial_pos(:,:,2) = initial_pos(:,:,1)';


% Generate image stack for population - increases execution speed
test_image_stack = zeros(rows,cols,num_images);


% Place initial image in stack position one
if strcmpi(pattern,'sinusoid')

    test_image_stack(:,:,1) = (sin(initial_pos(:,:,2)*(5/(cols+1))*pi) + ...
        sin(initial_pos(:,:,1)*(3/(rows+1))*pi));
else

    test_image_stack(:,:,1) = (sin(direction * (pi / 180)) * (initial_pos(:,:,2) / N) + ...
        cos(direction * (pi / 180)) * (initial_pos(:,:,1) / N));
end


% Generate base transformation matrix
transform = eye(3);
```

89

```matlab
% Complete transform matrix using selected procedure

if strcmpi(transformation,'trans')

    transform(1,3) = -row_offset;

    transform(2,3) = -col_offset;


elseif strcmpi(transformation,'mag')

    transform(1,1) = 1.0 / scale;

    transform(2,2) = transform(1,1);


elseif strcmpi(transformation,'rot')

    omega = angle * (pi / 180);

    transform(1,1) = cos(omega);

    transform(1,2) = -sin(omega);

    transform(2,1) = -transform(1,2);

    transform(2,2) = transform(1,1);


end


% Perform transformations and populate image stack

interim_pos = initial_pos;

for n = 2:num_images


    % Perform spatial transform

    for i = 1:rows

        for j = 1:cols

            interim_pos(i,j,:) = transform * squeeze(interim_pos(i,j,:));

        end

    end


    % Calculate pattern and populate stack

    if strcmpi(pattern,'sinusoid')

        test_image_stack(:,:,n) = (sin(interim_pos(:,:,2)*(5/(cols+1))*pi) + ...
```

```
            sin(interim_pos(:,:,1)*(3/(rows+1))*pi));

    else

        test_image_stack(:,:,n) = (sin(direction * (pi / 180)) * (interim_pos(:,:,2) / N) + ...

            cos(direction * (pi / 180)) * (interim_pos(:,:,1) / N));

    end

end
```

THE OXYGEN TRANSPORT EQUATION: A CONTINUUM MODEL OF GAS EXCHANGE IN HOLLOW FIBER MEMBRANE OXYGENATORS

B.1   BASIC ASSUMPTIONS

The arbitrary volume dV represents a volume of space within the hollow fiber membrane oxygenator that is differential with respect to the overall oxygenator size but large with respect to the size of RBCs and the hollow fibers; in essence $l_{RBCs,\,fibers} << dl << l_{device}$. The fluid and fibers are assumed to be incompressible. **Figure B1** shows graphically the basic assumptions utilized herein for deriving the oxygen transport equation.

---

[3] The formal derivation herein comes from an unpublished derivation authored by Dr. William J. Federspiel during initial discussions regarding the work outlined in this dissertation [90] W. J. Federspiel, "Continuum Models of Transport in HFM Modules," University of Pittsburgh, 1997, pp. 7. It refined an earlier ad hoc approach proposed in a grant application to the Whitaker Foundation.
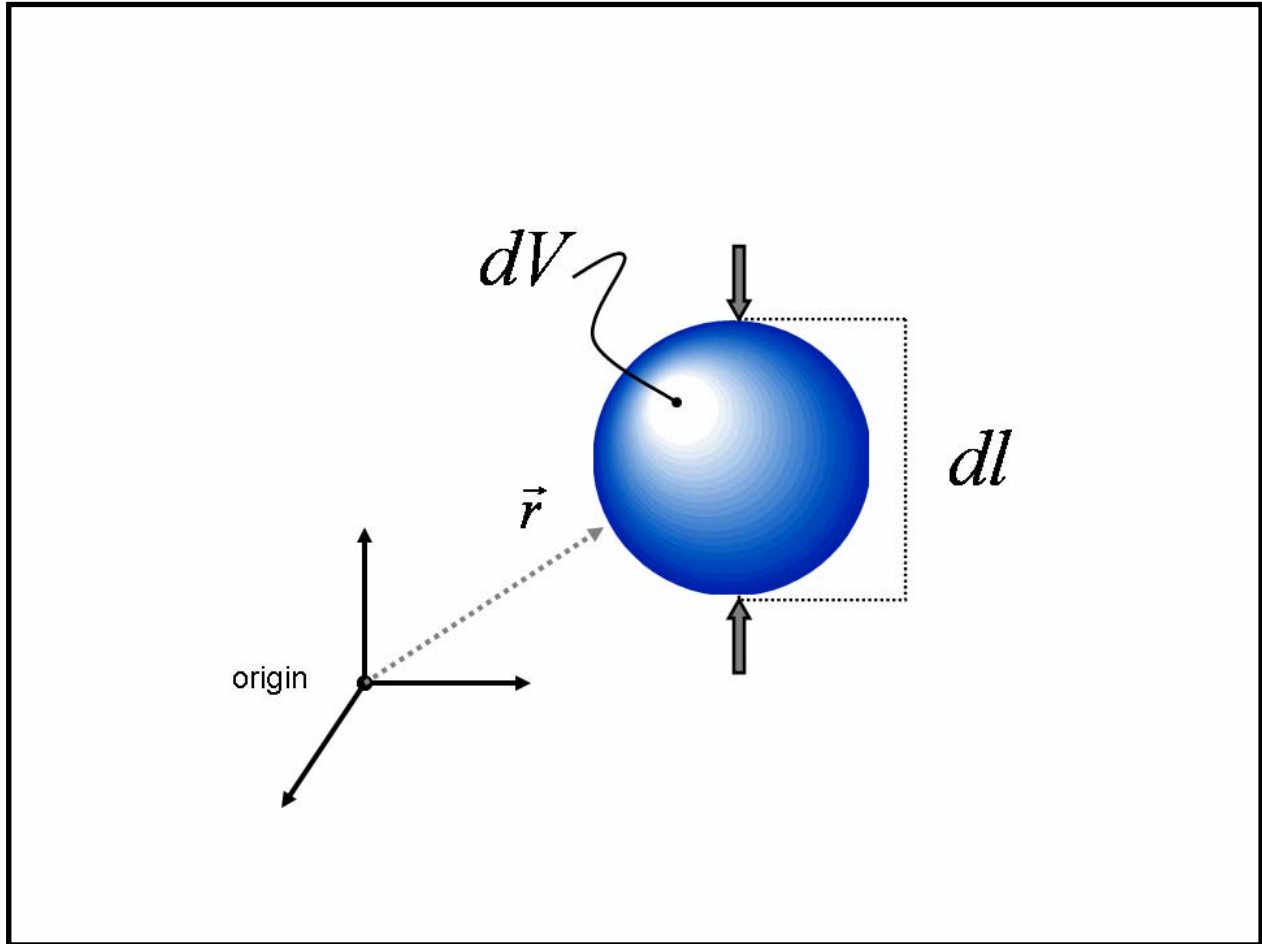
Figure B1 Graphic demonstrating basic assumptions of transport equation derivation.

B.2 VOLUME DEFINITIONS

A number of definitions regarding various volumes within the device are outlined below.

$$dV \equiv \text{differential volume of HFM on a continuum scale}$$

$$dV_f \equiv \text{fluid volume within } dV$$

$$dV_{fiber} \equiv \text{fiber volume within } dV$$

$$\frac{dV_f}{dV} \equiv \varepsilon$$

The porosity or void volume ε represents the ratio of fluid or open volume to the total volume. The porosity will be used later to define interstitial versus superficial velocities.

B.3   CONCENTRATION DEFINITIONS

First the amount of both free and hemoglobin-bound oxygen present in the differential volume dV is defined as equivalents to volumes of oxygen gas under STP conditions.

$$dV_{O2}^{f} \equiv \text{amount of free O2 in } dV \text{ in STP volumes of gas}$$

$$dV_{O2}^{b} \equiv \text{amount of bound O2 in } dV \text{ in STP volumes of gas}$$

With these definitions, the following oxygen concentrations on a fluid volume basis can be defined.

$$\text{Free } O_2 : \; C_{O2}^{f} \equiv dV_{O2}^{f}\Big/ dV_f$$

$$\text{Bound } O_2 : \; C_{O2}^{b} \equiv dV_{O2}^{b}\Big/ dV_f$$

The partial pressure of dissolved oxygen can be defined as follows, where α represents the oxygen solubility in blood.

$$P_{O2} \equiv C_{O2}^{f}\Big/ \alpha$$

The saturation of blood, S_{O2}, ranges from zero to one and can be defined as below in terms of C_T, which represents the total hemoglobin oxygen binding capacity in terms of STP volumes of oxygen per volume of fluid.

$$S_{O2} \equiv C_{O2}^{b}\Big/ C_T$$

94

B.4   FLOW AND FLUX DEFINITIONS

B.4.1   Interstitial versus Superficial Velocities

Fluid flow within hollow fiber membrane modules can be defined on either a superficial or interstitial basis. The interstitial velocity is the actual velocity of the fluid traveling within the interstices of the porous media; the area (and volume) for fluid transport within a differential volume element is reduced due to the presence of the hollow fibers in an amount proportional to the porosity, ε. In terms of the differential fluid flow rate dQ_f,

$$dQ_f = \frac{dV_f}{dt}$$
$$dQ_f = \vec{v} \cdot \vec{n}\, \varepsilon\, dA$$

In contrast, the superficial fluid velocity is more commonly used in the porous media literature, and can be defined using the differential fluid flow rate as:

$$dQ_f = \vec{u} \cdot \vec{n}\, dA$$

B.4.2   Definition of Total Oxygen Flux Vector

Defining the total oxygen flux vector requires one to consider an arbitrary differential area element dA as shown in **Figure B2**.
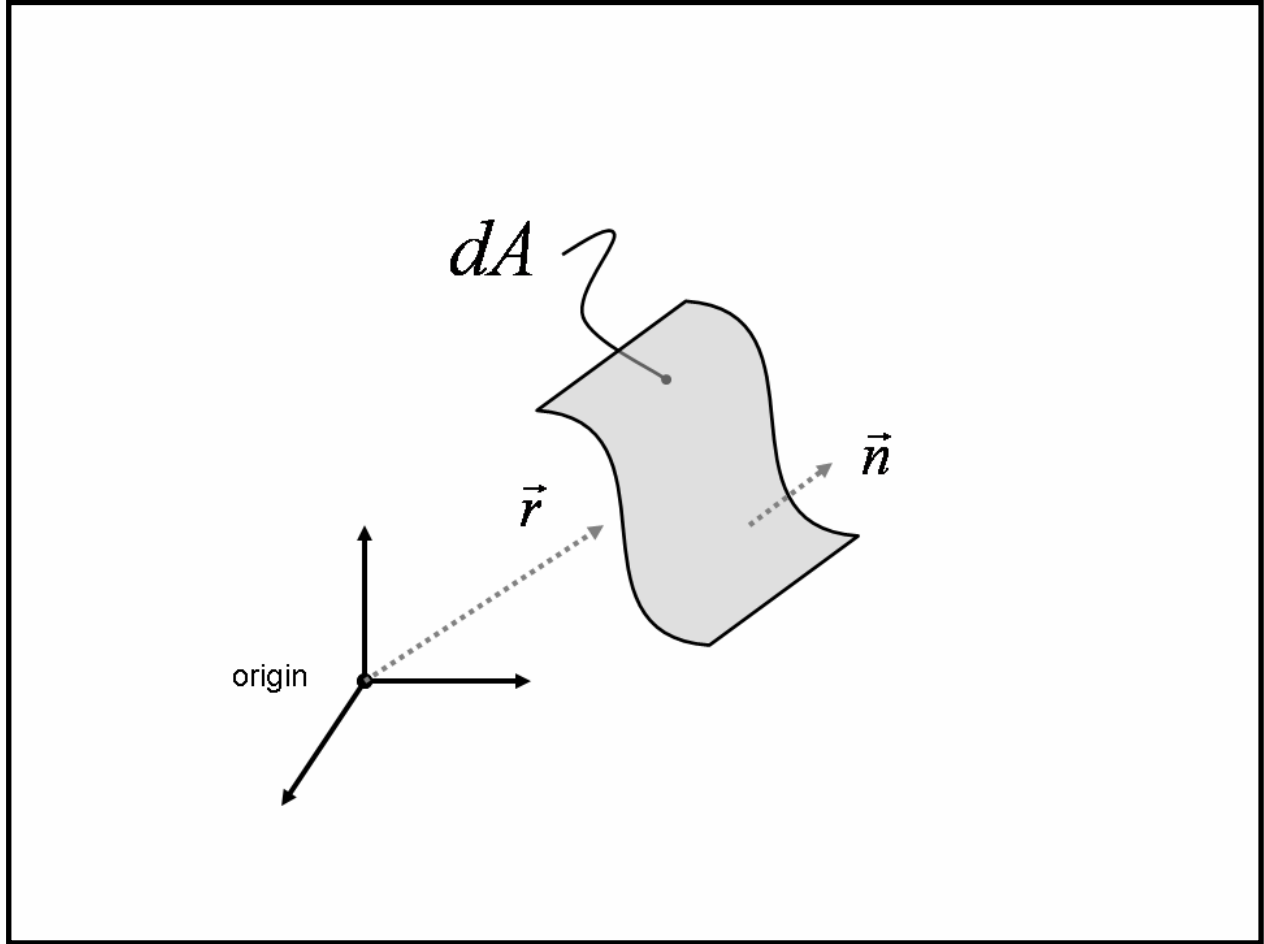
Figure B2 An arbitrary differential area element with surface normal vector.

The total flow rate of oxygen through the area dA is the aggregate of bound and dissolved amounts that are both convected and diffused.

$$d\dot{V}_{O2} = d\dot{V}_{O2}^{f,conv} + d\dot{V}_{O2}^{b,conv} + d\dot{V}_{O2}^{f,diff} + d\dot{V}_{O2}^{b,diff}$$

The bound oxygen is chemically complexed with hemoglobin, a protein residing within the RBCs. The large size of the RBCs results in a negligible diffusive contribution to the transport of bound oxygen. Therefore,

$$d\dot{V}_{O2}^{b,diff} \cong 0$$

The dissolved oxygen will diffuse down the concentration gradient in the standard manner, but will diffuse through that portion of the area that contains fluid and not fibers. With this consideration,

$$dV_{O2}^{f,diff} = -D\nabla C_{O2}^{f} \cdot \vec{n}\ \varepsilon dA$$

$$dV_{O2}^{f,diff} = -\varepsilon D\nabla C_{O2}^{f} \cdot \vec{n}\ dA$$

The convection of dissolved oxygen through the area element dA can be defined as follows:

$$d\dot{V}_{O2}^{f,conv} = \frac{dV_{O2}^{f}}{dt}$$

$$\frac{dV_{O2}^{f}}{dt} = \frac{dV_{O2}^{f}}{dV_{f}} \frac{dV_{f}}{dt}$$

Recall that:

$$dQ_{f} = \frac{dV_{f}}{dt} = \vec{u} \cdot \vec{n}\ dA$$

$$C_{O2}^{f} = \frac{dV_{O2}^{f}}{dV_{f}}$$

Incorporating these definitions into the above equations leads to the following form for the convection of free, dissolved oxygen through the area element dA :

$$d\dot{V}_{O2}^{f,conv} = C_{O2}^{f}\ \vec{u} \cdot \vec{n}\ dA$$

In a similar fashion, the convection of bound oxygen through the area element dA can be defined as:

$$d\dot{V}_{O2}^{b,conv} = C_{O2}^{b}\ \vec{u} \cdot \vec{n}\ dA$$

Returning to the initial equation defining the total flow rate of oxygen through the area element dA and substituting the derivations for the different terms:

$$d\dot{V}_{O2} = d\dot{V}_{O2}^{f,conv} + d\dot{V}_{O2}^{b,conv} + d\dot{V}_{O2}^{f,diff} + d\dot{V}_{O2}^{b,diff}$$

$$d\dot{V}_{O2} = C_{O2}^{f}\ \vec{u} \cdot \vec{n}\ dA + C_{O2}^{b}\ \vec{u} \cdot \vec{n}\ dA - \varepsilon D\nabla C_{O2}^{f} \cdot \vec{n}\ dA + 0$$

$$d\dot{V}_{O2} = \underbrace{\left(C_{O2}^{f}\ \vec{u} + C_{O2}^{b}\ \vec{u} - \varepsilon D\nabla C_{O2}^{f} \right)}_{\vec{N}_{O2}} \cdot \vec{n}\ dA$$

The term $\vec{N}_{O2}$ is known as the total oxygen flux vector. The flux vector can be rewritten in terms of the dissolved oxygen partial pressure, P_{O2}, to become:

$$\vec{N}_{O2} = \vec{u}\ \left(\alpha P_{O2} + C_{T} S_{O2} \right) - \varepsilon \alpha D\nabla P_{O2}$$

B.5 THE INTEGRAL OXYGEN MASS BALANCE

B.5.1 Definition of the Volumetric Oxygen Generation Rate

One can define a volumetric oxygen reaction or generation rate R on a fluid volume basis:

$$R \equiv \frac{\text{volume O}_2 \text{ generated}}{\text{time} \cdot V_f}$$

Recall that the term V_f represents the volume of fluid present in the overall volume element; oxygen can only be transferred into the fluid volume.

B.5.2 The Steady-state Equilibrium Mass Balance

Derivation of the integral oxygen mass balance requires one to consider an arbitrary volume V with surface area A as shown in **Figure B3.**
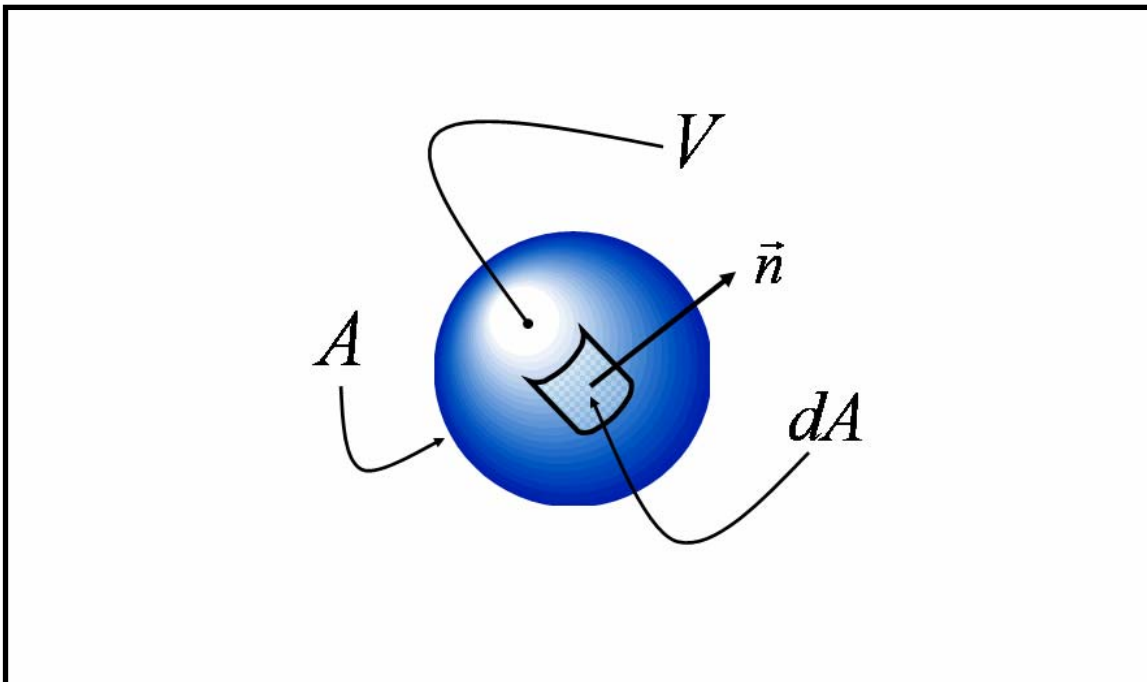
Figure B3 An arbitrary volume V used for derivation of the transport equation.

Assuming S.S. (steady-state), equilibrium exists between the flux through the surface A and the amount of oxygen generated within the volume V_f.

$$\int_A \vec{N}_{O2} \cdot \vec{n}\, dA = \int_V R\, dV_f$$

However, recall that the differential fluid volume dV_f is related to the differential total volume dV by the porosity ε the following equation:

$$dV_f = \varepsilon\, dV$$

Furthermore, one can utilize the Gauss-Ostrogradskii Divergence Theorem [91], which states that if V if a closed region in space surrounded by a surface S, then

$$\iiint_V (\nabla \cdot \mathbf{v})dV = \iint_S (\vec{n} \cdot \mathbf{v})dS$$

In the above theorem, the symbol $\mathbf{v}$ represents an arbitrary vector.

Applying the theorem to the left hand side of the equilibrium mass balance, one obtains the following:

$$\int_A \vec{N}_{O2} \cdot \vec{n}\, dA = \int_V \nabla \cdot \vec{N}_{O2}\, dV$$

Incorporating both changes into the equilibrium mass balance equation, the following relationship is obtained:

$$\int_V \nabla \cdot \vec{N}_{O2}\, dV = \int_V R\, \varepsilon\, dV$$

Taking the limit as $V \to 0$, the above leads to the differential oxygen balance shown below.

$$\nabla \cdot \vec{N}_{O2} = \varepsilon\, R$$

B.5.3 The Convection-Diffusion-Reaction Equation for Oxygen

Inserting the derivation for the oxygen flux vector, $\vec{N}_{O2}$, leads to the following relationship:

$$\nabla \cdot \vec{u} \left(\alpha P_{O2} + C_T S_{O2} \right) - \nabla \cdot \varepsilon \alpha D \nabla P_{O2} = \varepsilon\, R$$

The above equation can be further simplified using the following rule for the differentiation of products [91]:

$$\left(\nabla \cdot s\, \mathbf{v}\right)=\left(\nabla s \cdot \mathbf{v}\right)+ s\left(\nabla \cdot \mathbf{v}\right)$$

Recalling that the volume under consideration is incompressible and the commutative property of vector dot products, the following result is obtained.

$$\vec{u}\cdot\nabla\left(\alpha P_{O2} + C_T S_{O2}\right)=\nabla\cdot\varepsilon\alpha D\nabla P_{O2} + \varepsilon\, R$$

The above can be further simplified if it is assumed that the oxygen solubility is blood, α, and the total oxygen binding capacity for hemoglobin, C_T, are both constant. Recall that the saturation of blood with oxygen, S_{O2}, is a function of the partial pressure of oxygen, P_{O2}, allowing the definition of a new symbol, λ, that represents the slope of the saturation curve with respect to the partial pressure of oxygen.

$$\lambda = \left.dS_{O2}\middle/dP_{O2}\right.$$

Taken together, these assumptions and definitions result in the following equation:

$$\vec{u}\cdot\left(\alpha + C_T\lambda\right)\nabla P_{O2} = \nabla\cdot\varepsilon\alpha D\nabla P_{O2} + \varepsilon\, R$$

The above equation can be altered by dividing both sides of the equation by term preceding the partial pressure gradient, $\left(\alpha + C_T\lambda\right)$,

$$\vec{u}\cdot\nabla P_{O2} = \left(\alpha + C_T\lambda\right)^{-1}\nabla\cdot\varepsilon\alpha D\nabla P_{O2} + \frac{\varepsilon}{\left(\alpha + C_T\lambda\right)}R$$

It is now possible to define an effective volumetric oxygen generation or reaction term as follows:

$$R_{eff} = \frac{\varepsilon}{\left(\alpha + C_T\lambda\right)}R$$

The resulting equation then becomes

$$\vec{u}\cdot\nabla P_{O2} = \left(\alpha + C_T\lambda\right)^{-1}\nabla\cdot\varepsilon\alpha D\nabla P_{O2} + R_{eff}$$

B.5.4 Simplification for Uniform and Isotropic Porosity

If one assumes a constant and uniform porosity ε within the fiber module, along with a constant diffusivity of oxygen D within blood, the right-hand side of the above equation can be further simplified as follows:

$$\vec{u} \cdot \nabla P_{O2} = (\alpha + C_T \lambda)^{-1} \nabla \cdot \varepsilon \alpha D \nabla P_{O2} + R_{eff}$$

$$\vec{u} \cdot \nabla P_{O2} = \frac{\varepsilon \alpha D}{(\alpha + C_T \lambda)} \nabla \cdot \nabla P_{O2} + R_{eff}$$

$$\vec{u} \cdot \nabla P_{O2} = \frac{\varepsilon \alpha D}{(\alpha + C_T \lambda)} \nabla^2 P_{O2} + R_{eff}$$

It is now possible to define an effective variable diffusivity term, D_{eff}, as follows

$$D_{eff} = \frac{\varepsilon \alpha}{(\alpha + C_T \lambda)} D$$

The final form of the oxygen convection-diffusion-reaction equation in blood becomes

$$\vec{u} \cdot \nabla P_{O2} = D_{eff} \nabla^2 P_{O2} + R_{eff}$$

APPENDIX C

THE VOLUMETRIC OXYGEN GENERATION TERM

The convection-diffusion-reaction equation for oxygen transport in blood was derived in **Appendix B** and was found to be

$$\vec{u} \cdot \nabla P_{O2} = D_{eff} \nabla^2 P_{O2} + R_{eff}$$

The effective oxygen generation term, R_{eff}, is defined as follows.

$$R_{eff} = \frac{\varepsilon}{(\alpha + C_T \lambda)} R$$

Recall that the volumetric oxygen generation or exchange rate R has previously been defined as

$$R \equiv \frac{\text{volume O}_2 \text{ generated}}{\text{time} \cdot V_f}$$

In the above equations, the volumetric generation rate R has been defined but a method of calculation was not provided. Herein the details for calculating R are provided.

C.1 DEFINITION OF OXYGEN GENERATION USING THE LOCAL MASS TRANSFER COEFFICIENT AND EXCHANGE GRADIENT

The rate of local oxygen transfer can be determined using a local mass transfer coefficient K in the following manner:

$$\dot{V}_{O2} = K A_{HF} \Delta C_{O2}$$

In the above equation, $\dot{V}_{O2}$ represents the rate of oxygen generation in mL O2 per second. Recall

$$R \equiv \frac{\text{volume O}_2 \text{ generated}}{\text{time} \cdot V_f}$$

Therefore,

$$R = \frac{\dot{V}_{O2}}{V_f} = \frac{KA_{HF}\Delta C_{O2}}{V_f}$$

The driving force is in terms of volumes of dissolved oxygen per volume of fluid. It can be put in terms of the oxygen partial pressure using the solubility of oxygen in blood as follows.

$$\Delta C_{O2} = \alpha \Delta P_{O2}$$

Recall that the hydraulic radius for a porous media is defined as the ratio of the void or fluid volume to the wetted perimeter.

$$r_h = \frac{V_f}{A_{HF}}$$

The hydraulic radius for a hollow fiber oxygenator has been found [83] to be

$$r_h = \frac{\varepsilon d}{4(1-\varepsilon)}$$

Substituting into the equation for R provides the local volumetric generation rate in terms of the local mass transfer coefficient K and oxygen gradient ΔP_{O2}.

$$R = \frac{4(1-\varepsilon)}{\varepsilon d}K\alpha \Delta P_{O2}$$

C.2   CALCULATION OF THE LOCAL MASS TRANSFER COEFFICIENT K

In the above equation, the local mass transfer coefficient K remains unknown and requires determination from experimental data. Correlations for heat and mass transfer are abundant in the engineering and artificial organs literature and often take the form

$$Sh = aRe^{\alpha}Sc^{\beta}$$

It is common to assume the exponent of the Schmidt number is 0.33 in keeping with theoretical arguments [58]. The remaining coefficients a and α are determined from experiment following the methods outlined by various authors [80, 81, 83]. Please refer to these references for details.

In the paper of Vaslef [80], the dimensionless numbers Sh, Re, and Sc were defined as follows.

$$Sc = \frac{\nu}{D}$$

$$Sh = \frac{Kd_h}{D}$$

$$Re = \frac{vd_h}{\nu}$$

However, Mockros and Leonard [81] point out that an effective diffusivity should be used for the calculation of the Schmidt number. Note that this effective diffusivity, being based on the original derivation, differs from that presented in **Appendix B**; the porosity is not included.

$$D_{eff} = \frac{\alpha}{\left(\alpha + C_T \lambda\right)} D$$

The hydraulic diameter d_h is simply 4 times the hydraulic radius.

$$d_h \equiv 4r_h = \frac{\varepsilon d}{\left(1 - \varepsilon\right)}$$

Incorporating the above definitions into the mass transfer correlations reveals

$$\frac{Kd_h}{D} = a\left(\frac{vd_h}{\nu}\right)^\alpha \left(\frac{\nu}{D_{eff}}\right)^{\frac{1}{3}}$$

Rearranging terms reveals the final form

$$K = av^\alpha d_h^{\alpha-1} D^{\frac{2}{3}} \nu^{\frac{1}{3}-\alpha}\left(1 + \frac{C_T}{\alpha}\lambda\right)^{\frac{1}{3}}$$

APPENDIX D

MASS TRANSFER MATLAB M-FILES

The following appendix includes the MATLAB m-files used to analyze the mass transfer data acquired from the literature and to implement the various mathematical models therein.

D.1 OVERALL MASS TRANSFER COEFFICIENT SUBROUTINES

The following subroutines calculate the overall length averaged mass transfer coefficient following the methods of Vaslef, et al [80, 83].

D.1.1 K_length_ave.m

```
function K_overall = K_length_ave(Pin, Pout, species, device_name, Qfluid, Pfiber, varargin)

% usage:    K_overall = K_length_ave(Pin, Pout, species, device_name, Qfluid, Pfiber, ...

%                'Hb', Hb, 'Hct', Hct, 'T', T, 'pH', pH, 'tol', tol, 'trace', trace)

% units:    Pin Pout & Pfiber are in mmHg

%           species is a string ('bovine';'human')

%           device_name is a string ('Maxima';'Miniprime';'SMO1')

%           Qfluid is mL per sec

%           Hb is hemoglobin conc in g per mL

%           Hct is dimensionless between 0 and 1

%           pH is dimensionless
```

```
%           T is in degrees celsius

%           tol is the integral error tolerance (10e-6 default)

%           trace is a flag for tracing the integral progess (0 = off; default)

% author:   KLG 01-11-2004

% version:  0.1

% The function K_length_ave calculate the overall length averaged dimensionless

% mass transfer rate <K> as shown in equation seven of reference 1.  The local

% dimensionless mass transfer rates are averaged over the blood path length Lpath.

%

% References:

% 1. Vaslef SN, et.al. ASAIO Journal 40:990-996. 1994.

% 2. Vaslef SN. Analysis and design of an intravascular lung assist device.

%        PhD Thesis. Northwestern Univ, Chicago, IL. 1990.


% Obtain device parameters
if (ischar(device_name))

    [poros,dfiber,Afront,Lpath] = device_prop(device_name);

else

    error('Device_name not a string: see usage')

end


% Use flags to indicate if parameters are defaults or assigned; assign defaults

flagHb = 0; flagHct = 0; flagT = 0;  flagpH = 0;

Hb = 0.12; Hct = 0.36; T = 37; pH = 7.4;


% Use flags for assigning integral defaults

tol = 10^-6; trace = 0;


% Determine number and class of input parameters

if mod(length(varargin),2) == 0

    for i = 1:2:length(varargin)

        if ischar(varargin{i})

            switch varargin{i} % assign parameters where provided
```

106

```
                case 'Hb'

                    Hb = varargin{i+1}; flagHb = 1;

                case 'Hct'

                    Hct = varargin{i+1}; flagHct = 1;

                case 'T'

                    T = varargin{i+1}; flagT = 1;

                case 'pH'

                    pH = varargin{i+1}; flagpH = 1;

                case 'tol'

                    tol = varargin{i+1};

                case 'trace'

                    trace = varargin{i+1};

                otherwise

                    error(['Unknown parameter ', varargin{i}, ' : see usage']);

            end

        else

            error('Tags must precede data: see usage');

        end

    end


else

    error('Number of input arguments must be even: see usage');

end


% Report integral parameters

[stol, tolerr] = sprintf('The integral error tolerance is: %0.5g',tol);

disp(stol);

if trace == 0

    disp('Integral step trace is off');

else

    disp('Integral step trace is on');

end
```

```matlab
% Determine fluid properties and integrate appropriate terms
if (ischar(species))

    if (strcmpi(species,'bovine') | strcmpi(species,'human'))

        [exponent,P50] = Hill_equation_parameters(species,'pH',pH,'T',T);

        [Do2,ko2,Hufner_num,nu] = blood_prop(species,'Hb',Hb,'Hct',Hct,'T',T);


        % Report use of default variables where applicable
        if flagpH == 0

            disp('Default pH (7.4) assumed');

        end
        if flagT == 0

            disp('Default T (37 C) assumed');

        end
        if flagHb == 0

            disp('Default Hb (0.12 g/mL) assumed')

        end
        if flagHct == 0

            disp('Default Hct (0.36) assumed')

        end


        % Calculate value of integrand
        integrand = quadl(@pO2_integrand,Pin,Pout,tol,trace,ko2,Hufner_num,Hb, ...

            exponent,P50,Pfiber)


    elseif (strcmpi(species,'water'))

        error('Water properties not implemented');


        % Calculate value of integrand
        integrand = log((Pfiber - Pin)/(Pfiber - Pout));


    else

        error('Unknown fluid species: see usage');
```

```
        end


else

    error('species not a string: see usage');

end


% Calculate overall length averaged mass transfer coefficient

K_overall = (Qfluid * poros * dfiber^2)/(4 * Afront * Lpath * (1 - poros)^2 * nu) ...

    * (nu/Do2)^(2/3) * integrand;


% Subfunction for calculating value of integrand at a particular pressure

function integrand = pO2_integrand (P, ko2, Hufner_num, Hb, ...

    exponent, P50, Pfiber)


% Calculate slope of Hill equation

dSdP = slope_Hill_equation(exponent, P50, P);


% Calculate lambda - modified slope of oxyhemoglobin dissociation curve

lambda = Hufner_num .* Hb ./ ko2 .* dSdP;


% Calculate terms

integrand = ((1 + lambda).^(2/3))./(Pfiber - P);
```

D.1.2 Hill_equation_parameters.m

The following subroutine calculates the parameters of the Hill equation depending on the blood conditions during the experiment.

```
function [exponent, P50] = Hill_equation_parameters(species, varargin)

% usage:    [exponent, P50] = Hill_equation_parameters(species,'pH',pH,'T',T)

% units:    species is a string (bovine or human)

%           P50 is in mmHg

%           T is in degrees Celsius
```

109

```
%          pH is dimensionless

% author:   KLG 11-04-2003

% version:  0.1

% The function Hill_equation_parameters determines the

% various parameters for use in the Hill equation.

% references:

% 1. Vaslef SN, et.al. ASAIO Journal 40:990-996. 1994.

% 2. Mockros LF, et.al. Trans Am Soc Artif Intern Organs 31: 628-633. 1985.

% 3. Vaslef SN. Analysis and design of an intravascular lung assist device.

%    PhD Thesis. Northwestern Univ, Chicago, IL. 1990.

%

% NOTE: There is a discrepancy in the sign of the exponent in the equations used

% to calculate the bovine P50 with variable pH between the references. Email from

% Dr. Mockros at NWU verifies the correct signs of exponents: +0.41 for bovine P50ph

% and -0.24 for human P50. The values used were also compared and verified against

% those found in Dr. Vaslef's thesis.


% Use flags to indicate if parameters are defaults or assigned; assign defaults
flagpH = 1; flagT = 1;
pH = 7.4; T = 37;


% Determine number and class of input parameters
if length(varargin) == 0 % use defaults
    disp('Default pH (7.4) and temperature (37 C) assumed');
    flagpH = 0; flagT = 0;


elseif mod(length(varargin),2) == 0

    for i = 1:2:length(varargin)

        if ischar(varargin{i})

            switch varargin{i} % assign parameters where provided

                case 'pH'

                    pH = varargin{i+1}; flagpH = 0;

                case 'T'
```

```
                        T = varargin{i+1}; flagT = 0;

                    otherwise

                        error(['Unknown parameter ', varargin{i}, ' : see usage']);

                end

            else

                error('Tags must precede data: see usage');

            end

        end


else

    error('Number of input arguments must be even: see usage');

end


% Report use of default parameters

if flagpH == 1

    disp('Default pH (7.4) assumed');

elseif flagT == 1

    disp('Default T (37 C) assumed');

end


% Determine species and assign or calculate appropriate values

switch lower(species)

    case 'bovine'

        exponent = 2.85;                        % value from ref 1

        P50pH = 29.0 * (10^((0.41)*(7.4 - pH)));    % eqns from ref 2

        P50 = P50pH * (10^((-0.024)*(37 - T)));

    case 'human'

        exponent = 2.7;                         % value from ref 2

        P50pH = 26.6 * (10^((0.48)*(7.4 - pH)));    % eqns from ref 2

        P50 = P50pH * (10^((-0.024)*(37 - T)));

    otherwise

        error('Unknown species - no Hill parameters available');

end
```

111

D.1.3 blood_prop.m

The following subroutine calculates the transport properties of blood given the experimental conditions.

```
function [Do2, ko2, Hufner_num, nu] = blood_prop(species, varargin)


% References:
% 1.Colton CK, et al. Chem Eng Prog Symp Series No.99. Mass Transfer in Biological
%   Systems. 66:85-100.
% 2.Goldstick TK. Oxygen Transport. In: Engineering Principles in Physiology.
%   Brown JHU and Gann DS, eds. New York: Academic Press, 1973. p 257-282
% 3.Shaum's Vet Hematology


% Use flags to indicate if parameters are defaults or assigned and assign defaults
flagHb = 1; flagHct = 1; flagT = 1;     % Assuming 3 * Hb = Hct relationship
Hb = 12; Hct = 0.36; T = 37;


% Determine number and class of input parameters
if mod(length(varargin),2) == 0
    for i = 1:2:length(varargin)
        if ischar(varargin{i})
            switch varargin{i} % assign parameters where provided
                case 'Hb'
                    Hb = varargin{i+1}; flagHb = 0;
                case 'Hct'
                    Hct = varargin{i+1}; flagHct = 0;
                case 'T'
                    T = varargin{i+1}; flagT = 0;
                otherwise
                    error(['Unknown parameter ', varargin{i}, ' : see usage']);
            end
        else
```

```matlab
            error('Tags must precede data: see usage');

        end

    end


else

    error('Number of input arguments must be even: see usage');

end


% Report use of default parameters

if (strcmpi(species, 'water') & flagT == 1)

    disp('Default T (37 C) assumed');


else

    if flagHb == 1

        disp('Default Hb (12 g/dL) assumed');

    end

    if flagHct == 1

        disp('Default Hct (0.36) assumed');

    end

    if flagT == 1

        disp('Default T (37 C) assumed');

    end

end


% Calculate fluid properties

if strcmpi(species,'water')


    % Hufner Number describes hemoglobin O2 binding - 0 in H2O

    Hufner_num = 0;


    % Call H20 subroutine

    [Do2, ko2, nu] = water_prop(T);
```

```matlab
elseif (strcmpi(species,'bovine') | strcmpi(species,'human'))


    % Determine absolute (dynamic) blood viscosity
    eta_plasma = exp(-5.64 + 1800 / (T + 273)) / 100;
    eta = eta_plasma * exp(2.31 * Hct)    % g per (cm * s)


    % Determine blood density
    rho = 1.09*Hct + 1.035*(1 - Hct)    % g per mL


    % Determine kinematic blood viscosity
    nu = eta / rho;                      % cm2 per s


    % Assign Hufner Number - O2 carrying capacity of hemoglobin
    Hufner_num = 1.34;       % mL O2 per gm Hb


    % Determine O2 solubility in blood using method of Zander 1981
    % Temperature correction as suggested Vaslef 1990
    ko2_plasma = (2.855E-5) * (1.01)^(37 - T);
    ko2_rbc = (4.658E-5) * (1.01)^(37 - T);
    ko2 = Hct * ko2_rbc + ko2_plasma * (1 - Hct);    % mL O2 STP per mL blood * mmHg


    % Determine O2 diffusion in blood using values of Ciuryla 1975
    Do2_plasma = 1.62 * 10^-5 * (1.025)^(T - 25)     % cm2 per s
    Do2_rbc = 0.76 * 10^-5 * (1.025)^(T - 25)


    % Use modified Fricke approach for whole blood calculation
    M = 0.283;
    N = ko2_rbc / ko2_plasma;
    beta = (1/3) * ((2/(1 + (N * (Do2_rbc/Do2_plasma) - 1)*(M/2))) + ...
        (1/(1 + (N * (Do2_rbc/Do2_plasma) - 1)*(1-M)))) * ...
        (N * (Do2_rbc/Do2_plasma) - 1);
    chi = (-(N * (Do2_rbc/Do2_plasma) - 1) - (N * (Do2_rbc/Do2_plasma)) * beta) / ...
        ((N * (Do2_rbc / Do2_plasma) - 1) - beta);
```

```matlab
    R = Hct * ((N * (Do2_rbc / Do2_plasma) - 1)/ ...

        (N * (Do2_rbc/Do2_plasma) + chi));

    Do2 = Do2_plasma * (ko2_plasma / ko2) * ((1 + chi * R) / (1 - R));  % cm2 per sec


    % Report use of reference or method for solubility and diffusivity

    %disp('O2 diffusivity and solubility in whole blood from:');

    %disp('Goldstick TK. Oxygen Transport. In: Engineering Principles in Physiology.');

    %disp('Brown JHU and Gann DS, eds. New York: Academic Press, 1973. p 257-282');


    % Calculate whole blood diffusion constant

    %Do2 = 1.31 * 10^-5;      % cm2 per s at 37 C - reference Goldstick 1973


    % Assign whole blood O2 solubility - reference Goldstick 1973

    %ko2 = 2.4 * 10^-5;       % mL O2 STP per (mL blood * mmHg) at 37 C


else

    error('Unknown species: see usage');

end
```

D.1.4   device_prop.m

The following subroutine returns the device properties for the different devices for which data were available in the literature.

```matlab
function [poros, dfiber, Afront, Lpath] = device_prop(device_name)

% usage:    [poros, dfiber, Afront, Lpath] = device_prop(device_name)

% units:    poros is dimensionless

%           dfiber and Lpath are in cm

%           Afront is cm2

%           device_name is a string ('Maxima';'Miniprime';'SMO1')

% author:   KLG 11-04-2003

% version:  0.4

% The function device_prop assigns critical variables for use in
```

```matlab
% Vaslef model of oxygenator gas exchange.

% references:

% 1. Mockros LF, Leonard R. Trans Am Soc Artif Intern Organs

%       31:628-633. 1985.

% 2. Vaslef SN, et.al. ASAIO Journal 40:990-996. 1994.

% 3. Wickramasinghe


% 01-23-2004 KLG version 0.4

% Added Maxima Lpath and Afront area


% 01-11-2004 KLG version 0.3

% Updated file to include blood path length Lpath


% 12-01-2003 KLG version 0.2

% Based on an email response from Dr. Mockros the frontal area of

% of the Omnis Miniprime is assumed to be the same as that of the

% Sarns SMO1 - the two devices share a common history with the Omnis

% Miniprime being a prototype.  The fiber packing (porosity and total

% surface area) differ between the two oxygenators but the housing

% appears to be the same.


% Determine oxygenator name and assign variables
switch lower(device_name)


case 'miniprime'     % source references 1 & 2

    poros = 0.61;    % ref 1

    dfiber = 0.029; % ref 1 - 290 micron OD polypropylene HF

    Afront = 36.88; % ref 2 - see note above

    Lpath = 9.5;     % ref 2


case 'smo1'          % source reference 2

    poros = 0.576;

    dfiber = 0.029; % 290 micron polypropylene HF
```

116

```matlab
        Afront = 36.88;

        Lpath = 9.5;


    case 'maxima'

        poros = 0.625;  % calculated in notebook from reference 3 data

        dfiber = 0.046; % reference 3

        Afront = 52.09; % calculated in notebook from Medtronic diagrams

        Lpath = 10.05;


        % NOTE: Variables assumed constant although Afront changes with path

        % length due to angled core.


    otherwise

        error('Unknown device - no properties available');


end
```

BIBLIOGRAPHY

[1]   K. L. Gage and W. R. Wagner, "Cardiovascular Devices," in *Standard Handbook of Biomedical Engineering and Design*, *McGraw-Hill Standard Handbooks*, M. Kutz, Ed. New York: McGraw-Hill Professional, 2002, pp. 20.1-20.48.

[2]   A. H. Stammers, "Historical aspects of cardiopulmonary bypass: from antiquity to acceptance," *J Cardiothorac Vasc Anesth*, vol. 11, pp. 266-74, 1997.

[3]   W. Boettcher, F. Merkle, and H. H. Weitkemper, "History of extracorporeal circulation: the conceptional and developmental period," *J Extra Corpor Technol*, vol. 35, pp. 172-83, 2003.

[4]   H. G. Zimmer, "The heart-lung machine was invented twice--the first time by Max von Frey," *Clin Cardiol*, vol. 26, pp. 443-5, 2003.

[5]   M. Kurusz, "Cardiopulmonary bypass: past, present, and future," *ASAIO J*, vol. 50, pp. xxxiii-xxxvi, 2004.

[6]   H. Iwahashi, K. Yuri, and Y. Nose, "Development of the oxygenator: past, present, and future," *J Artif Organs*, vol. 7, pp. 111-20, 2004.

[7]   L. H. Edmunds, "Cardiopulmonary bypass after 50 years," *N Engl J Med*, vol. 351, pp. 1603-6, 2004.

[8]   J. H. Gibbon, Jr., "Application of a mechanical heart and lung apparatus to cardiac surgery," *Minn Med*, vol. 37, pp. 171-85, 1954.

[9]   J. J. C. Le Gallois, *Experiments on the principle of life*. Philadelphia, PA, U.S.A.: M. Thomas, 1813.

[10]   M. von Frey and M. Gruber, "Untersuchungen uber den Stoffwechsel isolirter Organe I. Ein Respirationsapparat fur isolirte Organe.," *Archiv für Physiologie*, vol. 9, pp. 519-532, 1885.

[11]   C. Dennis, D. S. Spreng, Jr., G. E. Nelson, K. E. Karlson, R. M. Nelson, J. V. Thomas, W. P. Eder, and R. L. Varco, "Development of a pump-oxygenator to replace the heart

and lungs; an apparatus applicable to human patients, and application to one case," *Ann Surg*, vol. 134, pp. 709-21, 1951.

[12] J. A. Wegner, "Oxygenator anatomy and function," *J Cardiothorac Vasc Anesth*, vol. 11, pp. 275-81, 1997.

[13] W. von Schroeder, "Ueber die Bildungsstätte des Harnstoffs," *Arch Exp Pathol Pharmakol*, vol. 15, pp. 364-402, 1882.

[14] C. Jacobj, "Apparat zur Durchblutung isolirter uberlebender Organe.," *Arch Exp Pathol Pharmakol*, vol. 26, pp. 388-400, 1890.

[15] V. L. Gott, R. A. Dewall, M. Paneth, M. N. Zuhdi, W. Weirich, R. L. Varco, and C. W. Lillehei, "A self-contained, disposable oxygenator of plastic sheet for intracardiac surgery; experimental development and clinical application," *Thorax*, vol. 12, pp. 1-9, 1957.

[16] L. H. Edmunds, Jr., "The evolution of cardiopulmonary bypass: lessons to be learned," *Perfusion*, vol. 17, pp. 243-51, 2002.

[17] G. H. A. Clowes, Jr. and W. E. Neville, "Further development of a blood oxygenator dependent upon the diffusion of gases through plastic membranes," *Trans Am Soc Artif Intern Organs*, vol. 3, pp. 52-58, 1957.

[18] G. H. Clowes, Jr., A. L. Hopkins, and W. E. Neville, "An artificial lung dependent upon diffusion of oxygen and carbon dioxide through plastic membranes," *J Thorac Surg*, vol. 32, pp. 630-7, 1956.

[19] P. M. Galletti and C. T. Mora, "Chapter 1. Cardiopulmonary bypass: The historical foundation, the future promise.," in *Cardiopulmonary bypass: Principles and techniques of extracorporeal circulation*, C. T. Mora, Ed. New York, NY. U.S.A.: Springer-Verlag, 1995, pp. 3-18.

[20] P. M. Galletti, "Cardiopulmonary bypass: a historical perspective," *Artif Organs*, vol. 17, pp. 675-86, 1993.

[21] P. A. Drinker and J. L. Lehr, "Engineering aspects of ECMO technology," *Artif Organs*, vol. 2, pp. 6-11, 1978.

[22] C. Jacobj, "Ein Beitrag zur Technik der künstlichen Durchblutung überlebender Organe.," *Arch Exp Pathol Pharmakol*, vol. 36, pp. 330-48, 1895.

[23] I. E. Konstantinov and V. V. Alexi-Meskishvili, "Sergei S. Brukhonenko: the development of the first heart-lung machine for total body perfusion," *Ann Thorac Surg*, vol. 69, pp. 962-6, 2000.

[24] W. T. Mustard, "Clinical and experimental experience with homologous and heterologous lung perfusion," *Trans Am Soc Artif Intern Organs*, vol. 1, pp. 94-95, 1955.

[25]   G. S. Campbell, N. W. Crisp, and E. B. Brown, Jr., "Total cardiac by-pass in humans utilizing a pump and heterologous lung oxygenator (dog lungs)," *Surgery*, vol. 40, pp. 364-71, 1956.

[26]   W. T. Mustard and J. A. Thomson, "Clinical experience with the artificial heart lung preparation," *Can Med Assoc J*, vol. 76, pp. 265-9, 1957.

[27]   D. C. McGiffin and J. K. Kirklin, "Chapter 32: Cardiopulmonary bypass for cardiac surgery," in *Surgery of the chest*, vol. 2, D. C. Sabiston Jr. and F. C. Spencer, Eds., 6th ed. Philadelphia, PA. U.S.A.: W.B. Saunders, 1995, pp. 1256-1271.

[28]   J. L. Svennevig, "Off-pump vs on-pump surgery. A review," *Scand Cardiovasc J*, vol. 34, pp. 7-11, 2000.

[29]   H. L. Anderson III and R. H. Bartlett, "Chapter 123: Extracorporeal life support for respiratory failure and multiple organ failure," in *Textbook of Critical Care*, A. Grenvik, S. M. Ayres, P. R. Holbrook, and W. C. Shoemaker, Eds., 4 ed. Philadelphia, PA. U.S.A.: W.B. Saunders, 2000.

[30]   R. H. Bartlett, D. W. Roloff, J. R. Custer, J. G. Younger, and R. B. Hirschl, "Extracorporeal life support: the University of Michigan experience," *JAMA*, vol. 283, pp. 904-8, 2000.

[31]   E. I. Cantekin and M. H. Weissman, "Experimental and theoretical considerations in augmenting oxygen transfer in membrane artificial lungs," *Med Biol Eng*, vol. 13, pp. 617-30, 1975.

[32]   K. Y. Chan, H. Fujioka, R. H. Bartlett, R. B. Hirschl, and J. B. Grotberg, "Pulsatile flow and mass transport over an array of cylinders: Gas transfer in a cardiac-driven artificial lung," *J Biomech Eng*, vol. 128, pp. 85-96, 2006.

[33]   K. K. Yeleswarapu, J. F. Antaki, M. V. Kameneva, and K. R. Rajagopal, "A mathematical model for shear-induced hemolysis," *Artif Organs*, vol. 19, pp. 576-82, 1995.

[34]   S. Goto, Y. Ikeda, E. Saldivar, and Z. M. Ruggeri, "Distinct mechanisms of platelet aggregation as a consequence of different shearing flow conditions," *J Clin Invest*, vol. 101, pp. 479-86, 1998.

[35]   M. J. Gartner, C. R. Wilhelm, K. L. Gage, M. C. Fabrizio, and W. R. Wagner, "Modeling flow effects on thrombotic deposition in a membrane oxygenator," *Artif Organs*, vol. 24, pp. 29-36, 2000.

[36]   P. W. Dierickx, D. S. De Wachter, F. De Somer, G. Van Nooten, and P. R. Verdonck, "Mass transfer characteristics of artificial lungs," *ASAIO Journal*, vol. 47, pp. 628, 2001.

[37] P. W. Dierickx, F. De Somer, D. S. De Wachter, G. Van Nooten, and P. R. Verdonck, "Hydrodynamic characteristics of artificial lungs," *ASAIO Journal*, vol. 46, pp. 532, 2000.

[38] E. N. Sorensen, G. W. Burgreen, W. R. Wagner, and J. F. Antaki, "Computational simulation of platelet deposition and activation: I. Model development and properties," *Ann Biomed Eng*, vol. 27, pp. 436-48, 1999.

[39] I. Taga, A. Funakubo, and Y. Fukui, "Design and development of an artificial implantable lung using multiobjective genetic algorithm: evaluation of gas exchange performance," *ASAIO J*, vol. 51, pp. 92-102, 2005.

[40] P. D. Richardson, "The artificial lung facility at Brown: more than a dozen years with Pierre Galletti," *ASAIO J*, vol. 51, pp. 165-72, 2005.

[41] US Department of Health and Human Services, "Guidance for Cardiopulmonary Bypass Oxygenators 510(k) Submissions; Final Guidance for Industry and FDA Staff," Center for Devices and Radiological Health, Food and Drug Administration, U.S. Department of Health and Human Services, 2000.

[42] AAMI Inc., "Cardiovascular implant and artificial organs - blood-gas exchangers," in *AAMI Standards and Recommended Practices*, vol. 1996. Arlington, VA: Association for the Advancement of Medical Instrumentation, 1996, pp. 633.

[43] T. Masuzawa, T. Tsukiya, S. Endo, E. Tatsumi, Y. Taenaka, H. Takano, T. Yamane, M. Nishida, B. Asztalos, Y. Miyazoe, K. Ito, T. Sawairi, and Y. Konishi, "Development of design methods for a centrifugal blood pump with a fluid dynamic approach: results in hemolysis tests," *Artif Organs*, vol. 23, pp. 757-61, 1999.

[44] G. W. Burgreen, J. F. Antaki, Z. J. Wu, and A. J. Holmes, "Computational fluid dynamics as a development tool for rotary blood pumps," *Artif Organs*, vol. 25, pp. 336-40, 2001.

[45] N. Matsuda, M. Nakamura, K. Sakai, K. Kuwana, and K. Tahara, "Theoretical and experimental evaluation for blood pressure drop and oxygen transfer rate in outside blood flow membrane oxygenator," *J Chem Eng Jpn*, vol. 32, pp. 752 -759, 1999.

[46] M. R. van Driel, "Cardioplegia heat exchanger design modelling using computational fluid dynamics," *Perfusion*, vol. 15, pp. 541-8, 2000.

[47] C. Bludszuweit, "Three-dimensional numerical prediction of stress loading of blood particles in a centrifugal pump," *Artif Organs*, vol. 19, pp. 590-6, 1995.

[48] J. Apel, R. Paul, S. Klaus, T. Siess, and H. Reul, "Assessment of hemolysis related quantities in a microaxial blood pump by computational fluid dynamics," *Artif Organs*, vol. 25, pp. 341-7, 2001.

[49] E. N. Sorensen, G. W. Burgreen, W. R. Wagner, and J. F. Antaki, "Computational simulation of platelet deposition and activation: II. Results for Poiseuille flow over collagen," *Ann Biomed Eng*, vol. 27, pp. 449-58, 1999.

[50] K. L. Gage, M. J. Gartner, G. W. Burgreen, and W. R. Wagner, "Predicting membrane oxygenator pressure drop using computational fluid dynamics," *Artif Organs*, vol. 26, pp. 600-7, 2002.

[51] M. S. Goodin, E. J. Thor, and W. S. Haworth, "Use of computational fluid dynamics in the design of the Avecor Affinity oxygenator," *Perfusion*, vol. 9, pp. 217-22, 1994.

[52] N. Matsuda and K. Sakai, "Blood flow and oxygen transfer rate of an outside blood flow membrane oxygenator," *Journal of Membrane Science*, vol. 170, pp. 153 - 158, 2000.

[53] A. K. Al-Hadhrami, L. Elliott, and D. B. Ingham, "A new model for viscous dissipation in porous media across a range of permeability values," *Transp Porous Media*, vol. 53, pp. 117-22, 2003.

[54] D. A. Nield, "Resolution of a paradox involving viscous dissipation and nonlinear drag in a porous medium," *Transp Porous Media*, vol. 41, pp. 349-57, 2000.

[55] Fluent Inc., "Chapter 7: Boundary Conditions," in *FLUENT 6.2 User's Guide*, vol. 1. Lebanon, NH, U.S.A.: Fluent, Inc., 2005, pp. 1-230.

[56] Fluent Inc., "Chapter 9: Modeling Basic Fluid Flow," in *FLUENT 6.2 User's Guide*, vol. 2. Lebanon, NH, U.S.A.: Fluent, Inc., 2005, pp. 1-32.

[57] S. V. Patankar, *Numerical Heat Transfer and Fluid Flow*. New York, NY, USA: Hemisphere Publishing Corporation, 1980.

[58] R. B. Bird, W. E. Stewart, and E. N. Lightfoot, *Transport Phenomena*, 1st ed. New York, NY, U.S.A.: John Wiley & Sons, Inc., 1960.

[59] M. Pohl, M. O. Wendt, S. Werner, B. Koch, and D. Lerche, "In vitro testing of artificial heart valves: comparison between Newtonian and non-Newtonian fluids," *Artif Organs*, vol. 20, pp. 37-46, 1996.

[60] P. W. Dierickx, D. De Wachter, and P. R. Verdonck, "Blood flow around hollow fibers," *International Journal of Artificial Organs*, vol. 23, pp. 610, 2000.

[61] A. Feinauer, S. A. Altobelli, and E. Fukushima, "NMR measurements of flow profiles in a coarse bed of packed spheres," *Magn Reson Imaging*, vol. 15, pp. 479, 1997.

[62] E. Fukushima, "Nuclear magnetic resonance as a tool to study flow," *Ann Rev Fluid Mech*, vol. 31, pp. 95-123, 1999.

[63] C. J. Elkins, M. Markl, N. Pelc, and J. K. Eaton, "4D magnetic resonance velocimetry for mean velocity measurements in complex turbulent flows," *Exp Fluids*, vol. 34, pp. 494-503, 2003.

[64] R. Deinsberger, R. Regatschnig, and K. Ungersbock, "Intraoperative evaluation of bone decompression in anterior cervical spine surgery by three-dimensional fluoroscopy," *Eur Spine J*, vol. 14, pp. 671-6, 2005.

[65] A. Feldman, "A sketch of the technical history of radiology from 1896 to1920," *Radiographics*, vol. 9, pp. 1113-28, 1989.

[66] B. A. Schueler, "The AAPM/RSNA physics tutorial for residents: general overview of fluoroscopic imaging," *Radiographics*, vol. 20, pp. 1115-26, 2000.

[67] B. K. P. Horn and B. G. Schunck, "Determining optical flow," *Artif Intell*, vol. 17, pp. 185-203, 1981.

[68] A. Singh, "Chapter 3: State of the Art," in *Optic flow computation: A unified perspective*, A. Singh, Ed. Los Alamitos, CA, USA: IEEE Computer Society Press, 1991, pp. 19-43.

[69] F. A. L. Dullien, *Porous Media: Fluid Transport and Pore Structure*, 2nd ed: Elsevier Science & Technology, 1991.

[70] J. L. Barron, D. J. Fleet, and S. S. Beauchemin, "Performance of optical flow techniques," *Int J Comput Vision*, vol. 12, pp. 43, 1994.

[71] A. Kaufman and K. Mueller, "Overview of volume rendering," in *The Visualization Handbook*, C. D. Hansen and C. R. Johnson, Eds., 1st ed. Burlington, MA, USA: Elsevier Butterworth-Heinemann, 2005, pp. 127-174.

[72] M. P. Garrity, "Raytracing irregular volume data," in *Proceedings of the 1990 workshop on Volume Visualization*. San Diego, CA, USA: ACM Press, New York NY USA, 1990.

[73] E. N. Lightfoot, "Low-order approximations for membrane blood oxygenators," *AIChE J*, vol. 14, pp. 669-670, 1968.

[74] H. S. Carslaw and J. C. Jaeger, *Conduction of Heat in Solids*, 2nd ed: Oxford University Press, 1986.

[75] M. H. Weissman and L. F. Mockros, "Oxygen transfer to blood flowing in round tubes," *American Society of Civil Engineers Proceedings, Journal of the Engineering Mechanics Division*, vol. 93, pp. 225 - 244, 1967.

[76] A. J. Makarewicz and L. F. Mockros, "Modeling oxygen transfer to blood from crossflow membrane oxygenators," presented at Proceedings of the 1995 Bioengineering Conference, Beever Creek, CO, USA, 1995.

[77] P. W. Dierickx, D. S. De Wachter, and P. R. Verdonck, "Two-dimensional finite element model for oxygen transfer in cross-flow hollow fiber membrane artificial lungs," *International Journal of Artificial Organs*, vol. 24, pp. 628, 2001.

[78] D. A. Baker, J. E. Holte, and S. V. Patankar, "Computationally two-dimensional finite-difference model for hollow-fibre blood-gas exchange devices," *Med Biol Eng Comput*, vol. 29, pp. 482-8, 1991.

[79] J. Happel, "Viscous flow relative to arrays of cylinders," *AIChE Journal*, vol. 5, pp. 174-177, 1959.

[80] S. N. Vaslef, L. F. Mockros, R. W. Anderson, and R. J. Leonard, "Use of a mathematical model to predict oxygen transfer rates in hollow fiber membrane oxygenators," *ASAIO Journal*, vol. 40, pp. 990, 1994.

[81] L. F. Mockros and R. Leonard, "Compact cross-flow tubular oxygenators," in *Transactions of the American Society of Artificial Internal Organs*, vol. 31, 1985, pp. 628-33.

[82] W. M. Kays and A. L. London, *Compact Heat Exchangers*, 2nd ed. New York, NY, U.S.A.: McGraw-Hill Book Co., 1964.

[83] S. N. Vaslef, "Analysis and design of an intravascular lung assist device," in *Biomedical Engineering*, vol. Ph.D. Evanston, IL: Northwestern University, 1990, pp. 186.

[84] S. R. Wickramasinghe, C. M. Kahr, and B. Han, "Mass transfer in blood oxygenators using blood analogue fluids," *Biotechnology Progress*, vol. 18, pp. 867, 2002.

[85] S. R. Wickramasinghe, M. J. Semmens, and E. L. Cusller, "Mass transport in various hollow fiber geometries," *J Memb Sci*, vol. 69, pp. 235, 1992.

[86] L. Graetz, "Ueber die Wärmeleitungsfähigkeit von Flüssigkeiten," *Annalen der Physik und Chemie*, vol. 261, pp. 337-357, 1885.

[87] E. N. Sieder and G. E. Tate, "Heat Transfer and Pressure Drop of Liquids in Tubes," *Ind Eng Chem*, vol. 28, pp. 1429-1435, 1936.

[88] T. J. Hewitt, B. G. Hattler, and W. J. Federspiel, "A mathematical model of gas exchange in an intravenous membrane oxygenator," *Ann Biomed Eng*, vol. 26, pp. 166-78, 1998.

[89] N. Cornelius and T. Kanade, "Adapting optical flow to measure object motion in reflectance and x-ray image sequences," presented at Proceedings of the ACM SIGGRAPH/SIGART Interdisciplinary Workshop on Motion:Representation and Perception, Toronto, Ontario, Canada, 1983.

[90] W. J. Federspiel, "Continuum Models of Transport in HFM Modules," University of Pittsburgh, 1997, pp. 7.

[91] R. B. Bird, W. E. Stewart, and E. N. Lightfoot, "Appendix A: Summary of Vector and Tensor Notation," in *Transport Phenomena*, 1st ed. New York, New York, U.S.A.: John Wiley & Sons, Inc., 1960, pp. 715-742.